

UNIVERSITY of OULU  
OULUN YLIOPISTO



COSTEL MUNTEANU

2015

# STUDIES ON THE MICROSTRUCTURE OF THE SOLAR WIND

COSTEL MUNTEANU

ISBN 978-952-62-1041-4  
ISBN 978-952-62-1042-1 (PDF)  
ISSN 1239-4327

REPORT SERIES IN PHYSICAL SCIENCES  
Report No. 98 (2015)

# **STUDIES ON THE MICROSTRUCTURE OF THE SOLAR WIND**

COSTEL MUNTEANU

*Astronomy and Space Physics Research Unit  
University of Oulu Graduate School  
University of Oulu  
Finland*

Academic Dissertation to be presented with the assent of the Doctoral Training Committee of Technology and Natural Sciences of the University of Oulu for public discussion in the Auditorium GO101, Linnanmaa, on December 4, 2015, at 12 o'clock noon.

REPORT SERIES IN PHYSICAL SCIENCES Report No. 98

OULU 2015 • UNIVERSITY OF OULU

**Supervisors**

Prof. Kalevi Mursula,  
University of Oulu, Finland

Dr. Marius Echim,  
Belgian Institute for Space Aeronomy (BISA), Brussels, Belgium

**Opponent**

Prof. Giuseppe Consolini,  
Institute for Space Astrophysics and Planetology (INAF), 00133 Rome, Italy

**Reviewers**

Dr. Zoltan Vörös,  
Space Research Institute, Austrian Academy of Sciences, Schmiedlstrabe 6, 8042  
Graz, Austria

Dr. Yasuhito Narita,  
Theoretical Space Plasma Physics, Space Research Institute, Austrian Academy of  
Sciences, Schmiedlstrabe 6, Graz, Austria

**Custos**

Prof. Kalevi Mursula,  
University of Oulu, Finland

ISBN 978-952-62-1041-4  
ISBN 978-952-62-1042-1 (PDF)  
ISSN 1239-4327

Juvenes Print Oulu  
Oulu 2015

**Munteanu, Costel,**

Studies on the microstructure of the solar wind

Astronomy and Space Physics Research Unit, University of Oulu, Finland

Report No. 98 (2015)

### *Abstract*

The thesis includes five original papers: the first three of them study solar wind discontinuities, the fourth paper studies solar wind turbulence, and the fifth paper studies the effect of data gaps on different spectral analysis methods.

Discontinuities are important structures in understanding the microstructure of the solar wind and its interaction with the Earth's magnetosphere. The key role of these small-scale structures in the statistical investigation of space plasma turbulence was only recently revealed. Also, a large part of these studies are affected by the almost ubiquitous presence of data gaps in satellite measurements, representing a real challenge in most statistical analysis methods. This thesis addresses these questions and offers answers and solutions to them.

We present a statistical study on predicting the propagation delay of solar wind discontinuities observed by both ACE, located at L1, and Cluster 3 (C3) spacecraft, close to the Earth's bow shock. Paper I studies almost 200 events between 2001 and 2007, Paper II introduces a new method of improving the time delay estimation using wavelet denoising to remove small scale fluctuations, and Paper III expands the study to more than 350 discontinuities between 2001 and 2012, performing a systematic analysis of the effect of wavelet denoising on time delay estimation accuracy. The methods used to predict the propagation delay, based on different ways of boundary normal estimation, are: the cross product method (CP), the minimum variance analysis of the magnetic field (MVAB), and the constrained minimum variance analysis (MVAB0). Paper III finds that, by tuning the method parameters for each discontinuity individually, the fraction of discontinuities estimated to arrive at C3 within  $\pm 2$  min from the observed time delay is significantly improved. Using wavelet denoising parameters optimized to each event, we found that 88% of our database of events are estimated to arrive within  $\pm 2$  min from the observed time delay with MVAB, 74% with CP, and 69% with the MVAB0 method.

We investigate Venus Express observations of magnetic field fluctuations during 2007-2009. Paper IV finds that the power spectral densities have higher levels of power for the fast solar wind than for the slow. The three components of the magnetic field exhibit different average spectral slopes for the fast and slow wind. Paper IV also investigates the variation of the spectral index as a function of the solar wind speed, and finds that the average spectral indices of the magnetic field become shallower with increasing plasma velocity.

We investigate the effect of data gaps for four methods of estimating the amplitude spectrum of a time series. Paper V shows that, for single data gaps, Fast Fourier Transform (FFT) and Discrete Fourier Transform (DFT) give an amplitude decreasing with gap size. On the other hand, the Z-Transform (ZTR) and the Lomb-Scargle algorithm (LST) preserve the absolute level of amplitude but lead to greatly increased spectral noise for increasing gap size. For multiple small data gaps, DFT, ZTR and LST can, unlike FFT, find the correct amplitude of sinusoidal modes even for a rather large data gap percentage. However, for in-situ data collected in a turbulent plasma environment, these three methods overestimate the high frequency part of the amplitude spectrum, while FFT only slightly underestimates it. Therefore, for small data gaps, FFT is the most appropriate method to approximate the spectral slope for turbulent spectra, while ZTR and LST are recommended for the study of well defined sinusoidal modes.

*Keywords:* Solar wind, Solar wind discontinuities, Solar wind turbulence, Analysis methods and tools



## Preface

This thesis is the result of a successful international collaboration between me and my two supervisors: Dr. Marius Echim, at the Belgian Institute for Space Aeronomy (BIRA-IASB) in Brussels, Belgium (also at Institute of Space Science (ISS) in Magurele, Romania) and Prof. Kalevi Mursula, at the Astronomy and Space Physics Research Unit of the University of Oulu, Finland.

I wish to express my sincere gratitude to my supervisors for the fruitful collaboration during these years and for their guidance and patience throughout my studies. I also wish to acknowledge the STORM FP7 project, the ReSoLVE Center of Excellence of the Academy of Finland and the University of Oulu for financial support.

I also acknowledge the science teams of the spacecraft mentioned throughout the thesis, most notably the Principal Investigators for the magnetic field instruments on-board ACE, Cluster and Venus Express spacecraft, for freely providing good quality in situ measurements to the scientific community. Without their sustained efforts not only in planning the missions but, most importantly, in maintaining and curating the data, our studies would not be possible.

Finally, I am also grateful to the members of the two research groups in which I carried out my activities: to my colleagues in the Space Plasma and Magnetometry Group of ISS: Gabriel Voitcu, Eliza Teodorescu and Catalin Negrea, with whom I had many fruitful scientific discussions, and to the Space Physics group in Oulu, especially to: Ilpo Virtanen, Lauri Holappa and Pauli Väisänen, with whom I also had many scientific discussions, but, who, more importantly, helped me with many practical details related to my stay in Oulu.

Oulu, November, 2015

Costel Munteanu



## Original publications

This thesis consists of an introduction and 5 original papers.

- I *Mailyan, B., C. Munteanu and S. Haaland (2008), What is the best method to calculate the solar wind propagation delay?, Ann. Geophys., 26, 2383-2394.*
- II *Haaland, S., C. Munteanu and B. Mailyan (2010), Solar wind propagation delay: Comment on "Minimum variance analysis-based propagation of the solar wind observations: Application to real-time global magnetohydrodynamic simulations" by A. Pulkinen and L. Raststatter, Space Weather, 8, S06005, doi:10.1029/2009SW000542.*
- III *Munteanu, C., S. Haaland, B. Mailyan, M. Echim, and K. Mursula (2013), Propagation delay of solar wind discontinuities: Comparing different methods and evaluating the effect of wavelet denoising, J. Geophys. Res. Space Physics, 118, 3985-3994, doi:10.1002/jgra.50429.*
- IV *Teodorescu, E., M. Echim, C. Munteanu, T. Zhang, R. Bruno and P. Kovacs (2015), Inertial range turbulence of fast and slow solar wind at 0.72 AU and solar minimum, The Astrophysical Journal Letters, 804:L41 (5pp), doi:10.1088/2041-8205/804/2/L41*
- V *Munteanu, C., C. Negrea, M. Echim and K. Mursula (2015), Effect of data gaps: Comparison of different spectral analysis methods, Ann. Geophys., submitted on August, 31, 2015*

In the text, original papers are referred to using roman numerals I–V.

In all papers the author had a major role in data analysis and in papers III and V the author was also the responsible writer.



# Contents

Abstract	
Preface	
Original publications	
Contents	
1. Introduction . . . . .	9
2. The structure of the solar wind . . . . .	11
2.1. Global structure . . . . .	11
2.2. Perturbations . . . . .	13
2.3. Average parameters at 1AU . . . . .	14
3. Satellite missions . . . . .	16
3.1. Advanced Composition Explorer . . . . .	16
3.2. Cluster spacecraft . . . . .	17
3.3. Venus Express . . . . .	18
4. Solar wind discontinuities . . . . .	20
4.1. Description . . . . .	20
4.2. Observations . . . . .	22
5. Solar wind turbulence . . . . .	24
5.1. Equations and phenomenology . . . . .	24
5.2. Observations of MHD turbulence . . . . .	27
6. Analysis methods and tools . . . . .	29
6.1. Discontinuity analysis . . . . .	29
6.2. Wavelet denoising . . . . .	35
6.3. Spectral analysis . . . . .	36
7. Summary . . . . .	39
References . . . . .	41



# 1. Introduction

This thesis studies the microstructure of the solar wind, in particular solar wind discontinuities, solar wind turbulence and related methods and analysis tools. We concentrate here on a small number of specific topics, among which we can mention: estimating the propagation time of solar wind discontinuities; using wavelet denoising techniques to increase the accuracy of time delay estimation; the characterization of solar wind turbulence at 0.72 AU at solar minimum; and the effect of data gaps on different spectral analysis methods. We also discuss the various classification schemes of discontinuities within the magnetohydrodynamic theory and present the main theories and observations on solar wind turbulence. One chapter presents the analysis methods and tools used in our studies.

Solar wind discontinuities, i.e., rapid changes in the interplanetary magnetic field and/or plasma parameters, are a major part of the micro-scale fluctuations observed in the solar wind. The nature and origin of these discontinuities has important implications on the microstructure of the solar wind. Low energy cosmic ray particles, for example, follow closely the topology of the interplanetary magnetic field and are guided along the field lines. Thus, rotational discontinuities, which resemble “kinks” in the magnetic field, can be important scattering centers for low energy cosmic rays. If, on the other hand, most solar wind discontinuities are tangential discontinuities, i.e., surfaces that separate plasma regions that are not magnetically connected, such scattering will not occur.

Our studies are also motivated by the connection between solar wind discontinuities and disturbances in the Earth’s magnetosphere, such as aurora, magnetospheric storms and substorms. Southward turnings of the IMF lead to enhanced reconnection with the geomagnetic field, thus allowing the transfer of energy and momentum from the solar wind into the magnetosphere, and setting up a large scale circulation of plasma in the magnetosphere [Dungey, 1961]. It has also been argued that northward turnings of the IMF can act as trigger for magnetospheric substorm onsets (see, e.g., Lyons *et al.*, 2003). The interaction of solar wind discontinuities with the Earth’s bow shock is also known to generate turbulence and structures, e.g. pressure pulses, SLAMS (short, large-amplitude magnetic structures), HFAs (hot flow anomalies), etc., within the magnetosheath (see, e.g., Archer *et al.* [2012]). For these studies is also important to understand discontinuities in

the solar wind and their propagation properties.

Turbulence and discontinuities in the solar wind have a well established connection. *Siscoe et al.* [1968] studied the contribution of discontinuities to the power spectrum of interplanetary magnetic field measurements made by Mariner 4. By using a simplified model, with a zero mean signal that maintains a constant value for varying periods of time and jumps discontinuously from one constant value to another at times having a Poisson distribution, *Siscoe et al.* [1968] showed that discontinuities might make a substantial contribution to the power spectrum at frequencies in the range of  $10^{-5}$  Hz to  $10^{-3}$  Hz and possibly even higher. This range partially overlaps with the range of frequencies usually associated with the inertial range of solar wind turbulence of  $10^{-4}$  Hz to  $10^{-1}$  Hz (see, e.g., Paper IV). Discontinuities may also be the walls of fossil flux tubes [*Burlaga, 1968; Burlaga, 1969; Borovsky, 2008*], in which case they need to be removed from the analysis since they are not part of turbulence. On the other hand, there are also studies showing how turbulence can generate small-scale discontinuities. These structures belong to the turbulent field, and have to be studied within the context of intermittent turbulence theories (e.g., *Matthaeus et al.* [2015]). These results motivated our studies on solar wind turbulence.

Spectral analysis is the most widely used tool in turbulence studies. The most important theories on turbulence make predictions about the slope of the power spectral density as a function of frequency in certain frequency ranges. A major drawback with spectral analysis based on the Fast Fourier Transform (FFT) is that it requires a uniform sampling and accepts no data gaps. The usual case with satellite measurements is that, due to instrument malfunction or measurement error, most datasets contain data gaps. In order to understand the effect of data gaps we tested some well known methods of computing the amplitude spectrum of time series with various gap configurations. Paper V presents the results of our study, which concludes that, in the presence of relatively small data gaps, FFT is the most appropriate method to compute the spectral slope for a turbulent spectrum, while the Z-Transform and the Lomb Scargle algorithm are recommended for the study of well defined sinusoidal modes.

The thesis is organized as follows: Chapter 2 presents the global structure of the solar wind and the major large-scale perturbations, Chapter 3 discusses the satellite missions used in our studies, Chapters 4 and 5 discuss solar wind discontinuities and turbulence, respectively, Chapter 6 gives details about the main analysis methods and tools used in our studies, and Chapter 7 summarizes the thesis.

## 2. The structure of the solar wind

The solar wind is a stream of fully ionized plasma released from the upper atmosphere (corona) of the Sun. It consists mostly of electrons and protons. Due to the high conductivity of the solar wind plasma, the magnetic field of the solar corona is "frozen" in the plasma and carried out into the entire heliosphere, forming the Interplanetary Magnetic Field (IMF). This "frozen-in" condition implies that the dynamics of the IMF follows closely the plasma dynamics, thus enabling us to describe, at least partly, the plasma dynamics by looking only at magnetic field measurements, which often have higher time resolution, better data coverage and higher overall quality.

In this Chapter we introduce some basic notions and parameters relevant for the description of the solar wind. The Chapter is divided into 3 Sections: 2.1 Global structure, 2.2 Perturbations and 2.3 Average parameters at 1AU. Section 2.1 introduces the concept of solar wind and describes its global structure; Section 2.2 describes the main disturbances and Section 2.3 gives the typical values of solar wind parameters at 1AU .

### 2.1. Global structure

On a global scale, but not very far from the sun, the IMF can roughly be thought of being produced by a giant bar magnet whose polarity reverses every 11 years. This yields opposite average fields near the solar poles at the minimum of the cycle, when the solar magnetic dipole is roughly aligned with the Sun's rotation axis. This dipolar field gradually weakens and reverses its direction near the maximum of the cycle, when the large-scale field is no longer dipole-like and has a complex multipolar structure.

Figure 2.1 shows the solar wind speed for the three polar orbits of the Ulysses spacecraft. The left panel shows the first orbit, which took place around the solar minimum of cycle 22 (1996), the middle panel shows the second orbit, near the solar maximum of cycle 23 (2000) and the third panel shows the third orbit, around

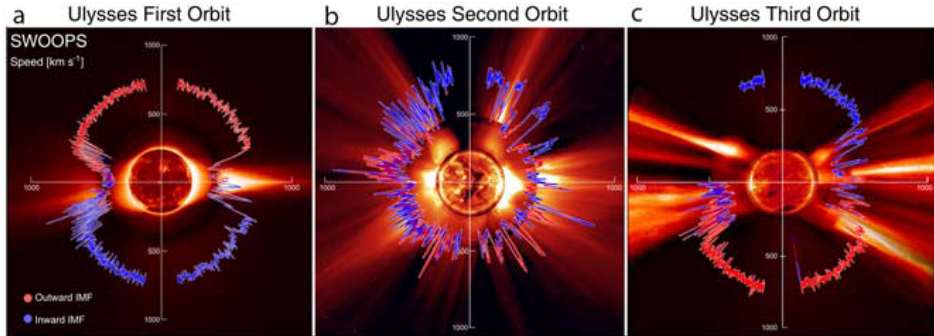


Fig. 2.1. Polar plots of the solar wind speed for the three polar orbits of the Ulysses spacecraft. In each panel, the earliest times are on the left and progress around counterclockwise. The colors indicate the magnetic polarity: red for positive (outward) IMF and blue for negative (inward) IMF. In panels a-c, the solar wind speed is plotted over characteristic solar images for solar minimum for cycle 22 (17-08-1996), solar maximum for cycle 23 (07-12-2000), and solar minimum for cycle 23 (28-03-2006). From the center out, blended images from the Solar and Heliospheric Observatory (SOHO) Extreme Ultraviolet Imaging Telescope (Fe XII at 1950 nm), the Mauna Loa K coronameter (700-950 nm), and the SOHO C2 white light coronagraph [McComas *et al.*, 2008].

the solar minimum of cycle 23 (2006). The polar plots of the solar wind speed are superposed on characteristic solar images typical for these periods of solar activity.

Near solar minimum of cycle 22 (panel a) in Fig. 2.1) we observe bright complex structures at low and mid latitudes, with bright streamers extending radially above them forming the so called streamer belt, whereas the polar regions appear uniformly darker. The solar wind speed also reflects this simple pattern: the speed is nearly constant at all latitudes except in a narrow band of  $\pm 20$  degrees around the equator. The pattern is also shared by the other properties, like the sign of the radial component of the magnetic field, also shown in Fig. 2.1, which remains rather constant within each hemisphere, being positive (outward) in the north and negative (inward) in the south.

Near solar maximum, middle panel of Fig. 2.1, we see a complex structure, typical of solar maximum, with bright streamers extending radially all around the Sun. The solar wind structure reflects this complexity, with alternating fast and slow streams observed at all latitudes. A complex structure is also seen in the IMF polarity, which fluctuates between positive and negative at all latitudes.

For the solar minimum of cycle 23 (panel c) in Fig. 2.1) we observe a pattern similar to the one for the previous solar minimum (depicted in panel a), except for the reversed IMF polarity. Also, the streamer belt extends to somewhat higher latitudes in this case.

Because the magnetic polarity is opposite on the two sides of the streamer belt, it must include a current which separates the two magnetic hemispheres. This

is called the Heliospheric Current Sheet (HCS), and it represents the extension of solar magnetic equator into the heliosphere. During the declining phase, there are large coronal holes, which extend down to the equator, warping the streamer belt and the HCS along the solar longitude. As the Sun rotates the HCS makes a nicely alternating structure, which reminds (and is called) the ballerina skirt. Because of the HCS warping, the high-speed streams above or below the HCS can be observed even at the low latitudes of the ecliptic plane.

To summarize, the solar wind observed at 1AU often has a bimodal structure, especially in the late declining to minimum phase of the solar cycle, when it consists of streams of fast solar wind ( $\sim 700\text{--}800$  km/s), and of slow solar wind ( $\sim 300\text{--}400$  km/s) (see, e.g., *Meyer-Vernet*, 2007).

## 2.2. Perturbations

Due to the wide variety of scales on which the fluctuations take place in the solar wind, it is useful to define certain ranges. When studying the characteristics of solar wind discontinuities on different scales, *Burlaga* [1969] introduced four useful time ranges: macro-scale ( $> 4$  days), meso-scale (1 hour - 4 days), micro-scale (36 sec - 1 hour) and kinetic-scale ( $< 36$  sec). Below we introduce the various phenomena and structures belonging to these time ranges.

On an average, particles move radially away from the Sun. Therefore, the stream lines connecting particles emerging from the same source region on the rotating Sun are curved like an Archimedean spiral. The curvature of the spiral is determined both by the flow speed and the distance from the Sun. The average angle between the stream lines and the radial direction to the Sun at 1 AU is about  $45^\circ$  [*Meyer-Vernet*, 2007]. The spiral structure of the IMF is a macro-scale characteristic of the solar wind. Other examples of macro-scale heliospheric structures are the Corotating Interaction Regions (CIRs), which are regions where a fast solar wind stream interacts with a slow stream, and Coronal Mass Ejections (CMEs). The latter are massive plasma clouds explosively released from the solar corona into the solar wind. Another example of macro-scale features of the solar wind are the sector boundaries, i.e., regions where the polarity of the magnetic field changes. These macro-scale phenomena are represented schematically in Fig. 2.2.

An early suggestion for a meso-scale structure of the solar wind is that it consists of a collection of intertwined and twisted filaments, regions with different plasma and field properties, separated by tangential discontinuities [*McCracken and Ness*, 1966]. Further observations revealed that such an ensemble of filamentary tubes with distinct boundaries enclosing well-ordered magnetic field lines is very difficult to identify. Therefore *Burlaga* [1969] suggested thinking of the interplanetary medium as discontinuous rather than filamentary. In this model the solar wind is structured by an ensemble of discontinuities rather than by pairs of discontinuities as in the filamentary model.

A considerable part of the micro - (and kinetic) scale consists of discontinuities.

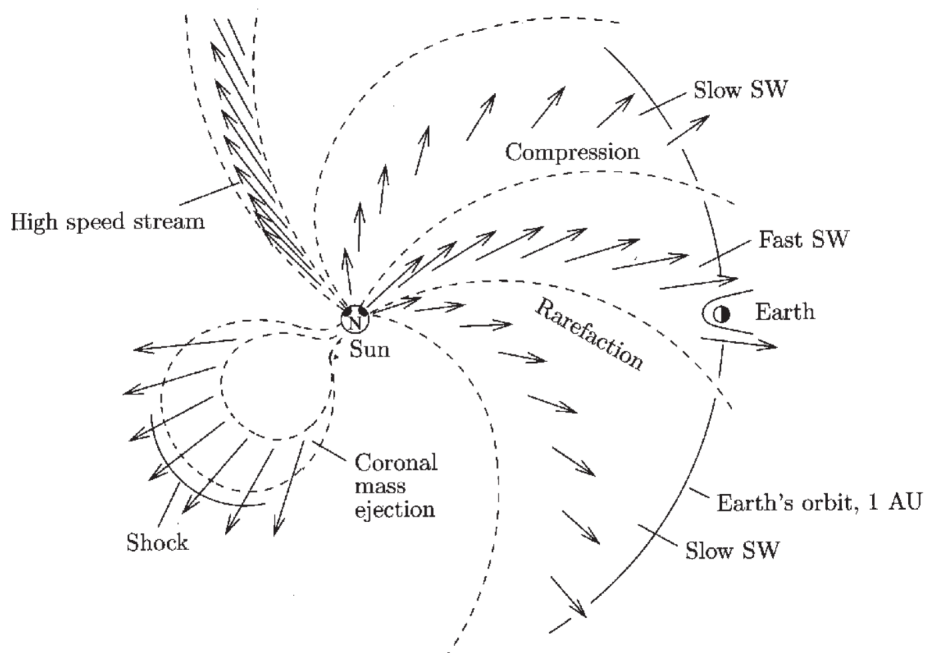


Fig. 2.2. The macro-scale phenomena of the solar wind [Prolss, 2004].

Alfvén waves across the inertial range of scales are also a micro-scale phenomena. These structures, and also their connection with solar wind turbulence are the main subject of this thesis, and will be discussed in detail in the following Chapters.

### 2.3. Average parameters at 1AU

Although the solar wind is a highly variable medium, one can estimate average values for its most important parameters from in-situ measurements. Since the solar wind is an expanding medium, we need to choose one heliocentric distance as a reference, and a natural choice for this is the mean distance of the Earth from the Sun, the astronomical unit (AU). Table 2.1 provides the values of several solar wind parameters, at 1AU.

Table 2.1. Typical values of solar wind parameters at 1 AU (adapted from *Bruno and Carbone* [2013]).

Parameter	Slow solar wind	Fast solar wind	Unit
Basic Properties			
number density	$\sim 15$	$\sim 4$	$\text{cm}^{-3}$
bulk velocity	$\sim 350$	$\sim 600$	km/s
proton temperature	$\sim 0.5 \times 10^5$	$\sim 2 \times 10^5$	K
electron temperature	$\sim 2 \times 10^5$	$\sim 1 \times 10^5$	K
magnetic field	$\sim 6$	$\sim 6$	nT
Speeds			
Alfvén	$\sim 30$	$\sim 60$	km/s
ion sound	$\sim 60$	$\sim 60$	km/s
proton thermal	$\sim 35$	$\sim 70$	km/s
electron thermal	$\sim 3000$	$\sim 2000$	km/s
Frequencies			
proton cyclotron	$\sim 0.1$	$\sim 0.1$	Hz
electron cyclotron	$\sim 2 \times 10^2$	$\sim 2 \times 10^2$	Hz
plasma	$\sim 2 \times 10^5$	$\sim 1 \times 10^5$	Hz
Lengths			
Debye	$\sim 4$	$\sim 15$	m
proton gyroradius	$\sim 130$	$\sim 260$	km
electron gyroradius	$\sim 2$	$\sim 1.3$	km

### 3. Satellite missions

The solar wind has been studied extensively since the beginning of the space age in the late nineteen-fifties, when the first interplanetary missions observed the solar wind in-situ. Several very successful missions were devoted to solar wind investigation only. The Helios 1 and Helios 2 missions, launched in 1974 and 1976, respectively, revealed the radial structure of the solar wind between 0.3 and 1 AU. The Ulysses deep-space mission, a joint European Space Agency (ESA) and National Aeronautics and Space Administration (NASA) mission, launched in October 1990, was the first to reveal the structure of the solar wind outside the ecliptic. NASA's Wind spacecraft launched in November 1994 made unique observations of the solar wind at 1 AU. NASA's Advanced Composition Explorer (ACE) spacecraft, originally thought of as a solar wind monitor for space weather, provides valuable continuous particle and field data for more than two decades. Magnetospheric and planetary missions with highly elongated orbits also sweep the solar wind at various radial distances (e.g. Cluster, Venus Express, Cassini).

In this Chapter we introduce the satellite missions used in our studies. The Chapter is divided into 3 Sections: 3.1 Advanced Composition Explorer, 3.2 Cluster spacecraft and 3.3 Venus Express. Each Section contains a "fact sheet" that gives details on the launch date, mission end, mission phase and orbit. We also discuss the scientific objectives and instrument payloads of these missions.

#### 3.1. Advanced Composition Explorer

The ACE mission [*Stone et al.*, 1998] was launched by NASA in August 1997. The spacecraft carries six high-resolution sensors and three monitoring instruments to sample low-energy particles of solar origin and high-energy galactic particles. ACE is a spinning spacecraft, rotating at 5 rpm, with the spin axis generally pointed along the Earth-Sun line and most of the scientific instruments on the top (sunward) deck. Details on the ACE mission are presented in Table 3.1.

ACE orbits the L1 libration point, which is a point of Sun-Earth gravitational equilibrium about 1.5 million km from Earth toward the Sun. From this loca-

Table 3.1. ACE fact sheet [ACE, 2015].

Launch date	25 August 1997
Mission end	the spacecraft has enough propellant on board to maintain an orbit at L1 until $\sim 2024$
Mission phase	operational
Orbit	orbit maneuvers keep the spacecraft bound to L1 ( $\sim 1.5$ million km from Earth)
Time spent in the solar wind	full-time

tion, ACE has a prime view of the solar wind, interplanetary magnetic field and higher energy particles accelerated by the Sun, as well as particles accelerated in the heliosphere and the galactic regions beyond. ACE also provides near-real-time continuous coverage of solar wind parameters and solar energetic particle intensities for space weather studies [SWPC, 2015]. ACE provides advanced warnings (at the lead time of about one hour) of geomagnetic storms that can overload power grids, disrupt communications on Earth, and present a hazard to satellites.

Papers I, II and III use IMF data obtained from the ACE Magnetic Field Experiment (MAG) [Smith *et al.*, 1998] at 16s time resolution and plasma data from the ACE Solar Wind Electron Proton Alpha Monitor (SWEPAM) [McComas *et al.*, 1998] experiment at 64s resolution. The datasets were downloaded via the Coordinate Data Analysis Web [CDAWeb, 2015]. Papers I and III use IMF data to calculate the boundary normal to the planar solar wind discontinuities (see Chapter 6, Section 6.1). The solar wind speed measured by SWEPAM, as well as the exact position of the spacecraft, are also used in time delay calculations. Paper II uses a sample of ACE IMF measurements to demonstrate the applicability of wavelet denoising techniques in calculating the solar wind time delay (see Chapter 6, Section 6.2).

### 3.2. Cluster spacecraft

The Cluster mission [Escoubet *et al.*, 2001] consists of four identical satellites flying occasionally in a tetrahedral configuration, with separation distances between the spacecraft varying between 600 km and 20 000 km, depending on the main scientific objective of a particular magnetospheric region. The main scope of the Cluster mission is to study the magnetospheric dynamics and the interaction with the solar wind using multi-point measurements that allow, for the first time, to disentangle the spatial and temporal variations. Details on the Cluster mission are presented in Table 3.2.

Cluster was planned together with SOHO, which monitors the Sun, and with ACE, which monitors the solar wind.

Table 3.2. Cluster fact sheet [*Cluster*, 2015].

Launch date	16-Jul-2000 12:39 UT and 09-Aug-2000 11:13 UT
Mission end	31 December 2018 (subject to a mid-term review in 2016)
Mission phase	operational
Orbit	elliptical polar orbit with a period of 57 hours, perigee at 19 000 km and apogee at 119 000 km
Time spent in the solar wind	a few hours per orbit, around the apogee, only during January to April every year

Each of the four spacecraft carries a nearly identical set of 11 instruments to investigate charged particles as well as electrical and magnetic fields and waves. For our purposes, we mainly used data from the Fluxgate Magnetometer (FGM) experiment [*Balogh et al.*, 2001], and from the Cluster Ion Spectrometry (CIS) experiment [*Rème et al.*, 2001].

Papers I and III use the official FGM prime parameter data with 4s time resolution provided by the Cluster Science Data System (CSDS). Most of the Cluster magnetic field measurements were taken from Cluster 3 (C3) spacecraft, and were used to compute, e.g., the time delay between the upstream solar wind monitor ACE and C3. Also, the exact position of C3 was used in the time delay calculations (see Chapter 6, Section 6.1). Cluster is primarily a magnetospheric mission, so the spacecraft enters the upstream solar wind only around the apogee, when the apogee is close to the solar direction, which takes place in the months January to April every year. Data from the CIS experiment were inspected to verify that C3 was indeed located in the solar wind.

### 3.3. Venus Express

Venus Express (VEX) [*Titov et al.*, 2001] is the first mission of ESA to the Earth's nearest planetary neighbor, the planet Venus. The science objectives of VEX are to study the atmosphere, the plasma environment, and the surface of the planet in great detail. Details on the VEX mission are presented in Table 3.3.

VEX arrived at Venus on 11 April 2006. Until the end of its main scientific mission, in May 2014, the spacecraft had a 24-hour elliptical, quasi-polar orbit, with a perigee of 250 kilometers, and an apogee of 66 000 kilometers. In May-July 2014, the spacecraft perigee was lowered to 129.2 km. At this altitude the atmospheric drag on the spacecraft reduced the orbital period to 22 hours 20 minutes.

Paper IV uses magnetic field data provided by the VEX-MAG magnetic field experiment [*Zhang et al.*, 2006] with a time resolution of 1s to compute and compare the power spectral densities of  $\mathbf{B}_x$ ,  $\mathbf{B}_y$  and  $\mathbf{B}_z$  for various solar wind conditions. The state of plasma (electron and ion spectra and their moments, e.g., density,

Table 3.3. VEX fact sheet [VEX, 2015].

Launch date	9 November 2005 03:33 UT
Mission end	31 December 2015
Mission phase	operational
Orbit	until May 2014, a 24-hour elliptical, quasi-polar orbit, with perigee at 250 km and apogee at 66 000 km. In May-July 2014 the perigee was lowered to 129.2 km, reducing the orbital period to 22 hours 20 minutes.
Time spent in the solar wind	20 to 22 hours per day; the plasma instrument, however, is switched on for maximum 1.5 hours close to the apogee

temperature, velocity) is investigated using the Analyzer of Space Plasmas and Energetic Atoms (ASPERA) [Barabash *et al.*, 2006]. The ion and electron spectra and their moments are provided with a time resolution of 196s, which is insufficient for a micro-scale analysis of the solar wind plasma parameters, but it does provide the data needed to discriminate between fast and slow solar wind.

## 4. Solar wind discontinuities

With an average occurrence rate of one or two per hour, discontinuities, i.e. abrupt changes in the IMF direction or magnitude and/or plasma parameters like velocity, density or temperature, are abundant micro-scale structures in the solar wind [Burlaga, 1969; Tsurutani and Smith, 1979].

In this Chapter we introduce discontinuities in the framework of magnetohydrodynamics (MHD) and present a brief overview of the main observational results on solar wind discontinuities. The Chapter is divided into 2 Sections: 4.1 Description and 4.2 Observations.

### 4.1. Description

An observer crossing through a discontinuity in the solar wind can experience rapid changes in the field and plasma parameters. MHD allows only certain well-defined changes from one side to the other that are controlled by the so called jump conditions. The first theoretical derivation of the jump conditions in a thermal isotropic plasma was given by *Landau and Lifshitz* [1960]. The theory for anisotropic plasma [Hudson, 1970; Neubauer, 1970] was developed later, mainly in response to the first solar wind measurements.

Two general classes of MHD discontinuities can be distinguished: stationary discontinuities, that do not propagate with respect to the ambient plasma, and propagating discontinuities. Stationary discontinuities include the contact discontinuity (CD) and the tangential discontinuity (TD). Propagating discontinuities are the fast and slow shocks and the rotational discontinuity (RD).

CDs have a non-zero normal component of the magnetic field, but no mass flux through the surface. They are boundaries between two media at rest, which may have different densities and temperatures [Landau and Lifshitz, 1960]. Due to the rapid diffusion along the field lines it is expected that CDs would rapidly broaden into smooth transitions [Knetter, 2005].

The most frequent discontinuities at the micro-scale level in the solar wind, are abrupt changes of the direction of the magnetic field [Burlaga, 1969]. Changes

in the field direction, called directional discontinuities (DDs), are predominantly expected for TDs and RDs. Therefore, the relatively rare fast and slow MHD shocks, will not be considered here.

TDs and RDs are pressure balanced structures (PBSs) [*Burlaga, 1971; Burlaga et al., 1990; Burlaga, 1995*]. PBSs are structures across which the total pressure (kinetic plus magnetic) is constant. Since the initial observations by *Burlaga* [1968], PBSs have been observed throughout the heliosphere [*Burlaga et al., 1990*].

Tangential discontinuities are stationary with respect to the ambient plasma. One way to distinguish a TD from any other PBS or DD, is to show that they are stationary, i.e., there is no component of the velocity, normal to the surface. Another important characteristic of TDs, distinguishing them from RDs, is that the normal component of the magnetic field along the boundary normal is zero. Since  $B_n = 0$ , the two sides of the discontinuity are not magnetically connected: a TD separates two completely distinct plasmas, which, for instance, may have different chemical composition. All other changes from one side to the other are arbitrary, for example, we can have TDs with or without velocity shears, with or without temperature or density jumps, etc. Any combination of values for density and temperature is allowed across a TD, provided that total pressure remains constant.

Rotational discontinuities are PBSs and/or DDs that propagate with respect to the ambient plasma, and have a non-zero magnetic field normal component. In the absence of a temperature anisotropy, the magnetic field magnitude, and plasma density and temperature are all constant across an RD. For RDs, also referred to as Alfvén shocks, the flow is Alfvénic on both sides of the discontinuity, so RDs propagate along the normal to the surface of the discontinuity at the Alfvén speed corresponding to the normal component of the magnetic field ( $V_{An} = \pm B_n / \sqrt{\mu_0 \rho}$ ), essentially like a kink in the magnetic field [*Burlaga, 1971; Burlaga, 1995*].

The most important characteristics of TDs and RDs are summarized in Table 4.1.

Table 4.1. Summary of the main properties of TDs and RDs (adapted from *Tsurutani and Ho* [1999]).

Property	Tangential Discontinuities	Rotational Discontinuities
propagation velocity	$= 0$	$\approx V_{An}$
mass flux ( $\rho V_n$ )	$= 0$	$\neq 0$
$B_n$	$= 0$	$\neq 0$

## 4.2. Observations

The existence of numerous discontinuities in the interplanetary magnetic field was first established experimentally by *Ness et al.* [1966]. Early studies on DDs found that the magnitude of the magnetic field and the density tend not to change across a DD [*Siscoe et al.*, 1968; *Burlaga*, 1969; *Burlaga*, 1971; *Solodyna et al.*, 1977]. *Burlaga* [1969] showed that the distribution of the time intervals between successive DDs follows an exponential decrease. This means that DDs tend to occur in clusters rather than being equally spaced in time.

An important question is whether DDs are produced near the Sun and then convected to larger heliocentric distances, or whether they are produced at all distances. In order to answer this question, the occurrence rate of DDs as a function of radial distance from the Sun has been determined [*Burlaga*, 1971; *Tsurutani and Smith*, 1979; *Lepping and Behannon*, 1986]. All of these studies reveal a decrease of DD occurrence rate with increasing heliospheric distance. This implies that DDs are generated close to the Sun and disintegrate at larger distances. However, it can also imply that the ratio of generation rate to disintegration rate becomes smaller as we increase the heliocentric distance, or that the discontinuities change size in some manner such that the used identification criteria bias the result [*Lepping and Behannon*, 1986].

The relative abundance of RDs and TDs in the solar wind has also been controversially discussed. *Siscoe et al.* [1968] find that for 80% of discontinuities the rotation of the magnetic field vector takes place in a plane, which is equivalent to the condition  $B_n = 0$ , thus concluding that these structures are TDs. *Burlaga* [1971] comes to a similar conclusion: less than 25% of DDs are RDs, and the majority of DDs are thus TDs. Studies that use both the normal magnetic field component and the change in field magnitude across the discontinuity usually find a predominance of RDs [*Smith*, 1973; *Lepping and Behannon*, 1980]. *Neugebauer et al.* [1984] estimate that the number of RDs is higher by a factor of 5 to 9 than the number of TDs.

Different solar wind conditions may be the reason to the discrepancy regarding the relative abundance of RDs and TDs. A detailed study on the dependence of occurrence of RDs and TDs on solar wind type is presented in *Neugebauer and Alexander* [1991]. They found that the highest frequency of occurrence of RDs is found in fast streams originating from coronal holes on the Sun. In contrast, a high rate of TDs is found in solar wind streams originating in the active regions of the Sun.

We point out that the results presented above are solely based on single-spacecraft techniques. There have also been studies utilizing the relative timing between multiple spacecraft to determine the normals [*Burlaga and Ness*, 1969; *Horbury et al.*, 2001a; *Knetter et al.*, 2004; *Knetter*, 2005]. *Horbury et al.* [2001a] finds that the relative timing method yields an abundance of TDs over RDs. Note, however, that most of the above mentioned results about the relative abundance of RDs and TDs have recently been seriously questioned by findings about the unreliability of the minimum-variance technique used in these findings [*Horbury et al.*, 2001a, b; *Knetter et al.*, 2004; *Knetter*, 2005].

The recent study by *Borovsky* [2008] and the review article by *Bruno and Carbone* [2013] revive the early filamentary model described by *McCracken and Ness* [1966] (see also Chapter 2, Section 2.2). *Borovsky* [2008] argues that the inner heliosphere is filled with a network of entangled magnetic flux tubes, which are structures originating at the solar surface, and that this tube texture impacts the flow properties and turbulence in the solar wind. *Bruno and Carbone* [2013] devote an entire Chapter to micro-scale turbulent structures in the solar wind. These turbulent, or coherent structures, which are localized zones of fluid where phase correlation exists [*Farge*, 1992], dominate the statistics of small scales. According to this idea, solar wind turbulence is made by a mixture of structures convected by the wind, most of which are very difficult or even impossible to classify within the framework of MHD discontinuities, and stochastic fluctuations.

These ideas motivated us to go beyond the simple MHD classification of discontinuities and study the statistical properties of coherent structures as part of solar wind turbulence (see, e.g., *Matthaeus et al.* [2015]). The next Chapter is dedicated to solar wind turbulence.

## 5. Solar wind turbulence

In this Chapter we present some basic equations used to describe the flow of charged fluids, and the phenomenological aspects of fully developed turbulence. Section 5.1 introduces the concept of turbulence and its basic phenomenological aspects from the Navier-Stokes equation and Reynolds number to Richardson cascade, Kolmogorov and Iroshnikov-Kraichnan spectra and finally to the critically balanced theory of *Goldreich and Sridhar* [1995]. Section 5.2 shows examples of observational evidence for turbulence in the solar wind, starting with the first paper by *Coleman* [1968], and more recently by *Podesta et al.* [2007] and *Horbury et al.* [2008].

### 5.1. Equations and phenomenology

The word turbulence used in the everyday experience indicates something which is not regular (coming from the Latin word *turba*, meaning something confusing or something which does not follow an ordered plan).

The solar wind is a supersonic and super-Alfvénic plasma stream which exhibits turbulent features. It is often said that the solar wind is a cosmic turbulence laboratory [*Bruno and Carbone*, 2013]. The fleet of spacecraft launched during the last decades offer the chance to investigate in-situ the structure of solar wind turbulence over long time intervals.

Fluid turbulence has a very special character: it is disordered, but it is not entirely chaotic and unpredictable; namely, small scale stochastic fluctuations and large scale macroscopic structure can coexist within the same turbulent stream [*Meyer-Vernet*, 2007].

Turbulence became an experimental science in the 19<sup>th</sup> century, when Osborne Reynolds was the first to observe and investigate the transition from laminar to turbulent flow. He noticed that the flow becomes turbulent whenever a single parameter, a certain combination of a characteristic velocity  $U$ , a characteristic length  $L$ , and the kinematic viscosity  $\nu = \eta/\rho$  (with  $\eta$  being the viscosity coefficient and  $\rho$ , the mass density), would increase. This is now called the Reynolds number:

$R = UL/\nu$ . At lower values, say  $R \leq 2000$ , the flow is laminar, but when  $R$  increases beyond a certain threshold of the order of  $R \approx 4000$ , the flow becomes turbulent [Bruno and Carbone, 2013].

Considering an incompressible (constant  $\rho$ ) neutral fluid, we can write the equation describing the dynamics of the flow, the so called Navier-Stokes (NS) equation, as follows:

$$\frac{\partial \mathbf{u}}{\partial t} + (\mathbf{u} \cdot \nabla) \mathbf{u} = -\frac{\nabla p}{\rho} + \nu \nabla^2 \mathbf{u} \quad (5.1)$$

where  $\mathbf{u}(\mathbf{r}, t)$  is the velocity field and  $p$  is the kinetic pressure.

Using the velocity  $U$  and the length scale  $L$  to define dimensionless coordinates  $r = r'L$  (from which  $\nabla = \nabla'/L$ ) and  $t = t'(L/U)$ , and dimensionless variables  $u = u'U$  and  $p = p'U^2\rho$ , we obtain:

$$\frac{\partial u'}{\partial t'} + (\mathbf{u}' \cdot \nabla') \mathbf{u}' = -\nabla' p' + R^{-1} \nabla'^2 \mathbf{u}' \quad (5.2)$$

The Reynolds number  $R$  is evidently the only parameter of the fluid flow. Equation 5.2 shows that the Reynolds number represents a measure of the relative strength between the non-linear convective term  $(\mathbf{u}' \cdot \nabla') \mathbf{u}'$  and the viscous term  $\nabla'^2 \mathbf{u}'$ . The higher  $R$  is, the smaller the viscous term is and the more important the non-linear term is in the dynamics of the flow.

The phenomenological description of turbulence is mainly based on the paradigm of an energy cascade that transports energy from larger to smaller scales by collections of eddies (“whirls”) at all scales: “Big whirls have little whirls that feed on their velocity, and little whirls have lesser whirls and so on to viscosity” [Richardson, 1922].

Energy injected at some large scale  $L$ , is transferred through non-linear interactions to the small (dissipation) scale  $l_D$  (Fig. 5.1). In a stationary situation, the energy injection rate must be balanced by the energy dissipation rate and also by the energy transfer rate  $\epsilon$  measured at any scale  $l$  within the intermediate range  $l_D \ll l \ll L$  (the so-called inertial range, in which inertia dominates over viscosity). If viscosity can be neglected, the only relevant physical parameter for an eddy is the energy transfer rate  $\epsilon$  that cascades through the system per unit time per unit mass. The energy per unit mass  $\sim u_l^2$  is transferred during a time  $\sim l/u_l$ , so that the energy rate is  $\epsilon \sim u_l^2/(l/u_l)$ . Hence, the velocity fluctuation at scale  $l$  varies as:

$$u_l \sim (l\epsilon)^{1/3} \propto l^{1/3} \quad (5.3)$$

where we have dropped  $\epsilon$  out of the parenthesis since it does not depend on the size  $l$  in the absence of viscous dissipation (i.e. for  $l_D \ll l \ll L$ ).

This is the classical law of Kolmogorov: the velocity fluctuation varies with the scale as  $l^{1/3}$  - a universal scaling for turbulent flows. By the same argument, the moments of order  $n$  of the velocity differences  $u_l$  at scale  $l$  (defining the so-called structure functions) obey the relation

$$\langle u_l^n \rangle \sim l^{n/3} \quad (5.4)$$

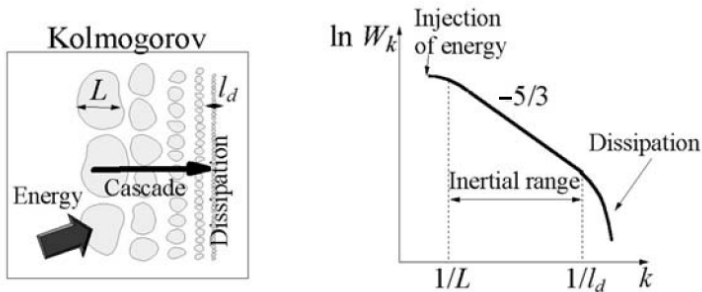


Fig. 5.1. Richardson's picture for energy cascade: the “Richardson cascade” (left) and the corresponding wave number spectrum of the turbulent energy (right) [Meyer-Vernet, 2007].

One can also estimate how the energy fluctuations at a given location are distributed over spatial scales. This is generally plotted as the spectral density of the energy fluctuations as a function of wave number:  $W_k(k)$ . Since the energy in the fluctuations at scale  $l$  varies as  $\langle u_l^2 \rangle \sim l^{2/3}$  (Eq. 5.4), the fluctuation energy per unit wave vector (in one direction)  $k \sim l^{-1}$  varies as  $l^{2/3} \times l \propto l^{5/3}$ , i.e. as  $k^{-5/3}$ . Hence the spectrum of the fluctuation energy varies as

$$W_k \propto k^{-5/3} \text{ for } L^{-1} \ll k \ll l_D^{-1} \quad (5.5)$$

This type of scaling for the inertial range is often referred to as the Kolmogorov K41 spectrum (see also Fig. 5.1), and is considered one of the main results of the phenomenology of turbulence [Frisch, 1995].

In order to apply these concepts to solar wind turbulence, which is a magnetized plasma flow, we first need to understand the effect of the magnetic field. The magnetic field introduces an anisotropy and additional forces, so that the turbulent “eddies” could be considered MHD waves (more precisely Alfvén waves since other waves are in general damped). We can picture the fluid eddies, whose interaction produces the energy cascade, as Alfvén waves moving at opposite Alfvén speeds  $V_A$ . In this case, they interact only during the time taken by an Alfvén wave to travel their size, i.e.  $t_A \propto l/V_A$ . The energy cascading through an eddy of size  $l$  during this time is  $\Delta E_l \propto u_l^2/(l/u_l) \times l/V_A \propto u_l^3/V_A$ . The energy  $u_l^2$  (per unit mass) exchanged with a number  $N$  of such interactions is (assuming a random walk process)  $u_l^2 \propto \sqrt{N}\Delta E_l$ , whence  $N \sim (V_A/u_l)^2$ . Since  $N$  interactions of duration  $t_A$  require the time  $Nt_A$ , the energy cascading per unit time is  $\epsilon \propto u_l^2/(Nt_A) \propto u_l^4/(lV_A)$ . We can thus estimate that velocity fluctuations at scale  $l$  vary as:

$$u_l \sim (\epsilon V_A l)^{1/4} \propto l^{1/4} \quad (5.6)$$

Since the energy in the fluctuations at scale  $l$  varies as  $\langle u_l^2 \rangle \sim l^{1/2}$ , the fluctuation energy per unit wave vector varies as  $l^{1/2} \times l \propto l^{3/2}$ , i.e. as  $k^{-3/2}$ . Thus the

spectrum of the fluctuation energy for the magnetized case is:

$$W_k \sim k^{-3/2} \quad (5.7)$$

The phenomenology for the magnetic field dominated case discussed above, has been developed by *Iroshnikov* [1964] and *Kraichnan* [1965] and it is now referred to as the IK model [*Bruno and Carbone*, 2013].

*Goldreich and Sridhar* [1995] describe a critically balanced case, referred to as the GS model, where the linear Alfvén time scale or wave period is balanced by the non-linear time scale needed to transfer energy to smaller scales. In these conditions, it can be shown that the power spectrum would scale as  $W_k \sim k^{-5/3}$  when the angle  $\theta_B$  between the mean field direction and the flow direction is  $90^\circ$ , while the scaling would be  $W_k \sim k^{-2}$  in case  $\theta_B = 0^\circ$ , whence the spectrum would also have a smaller energy content than in the perpendicular case.

## 5.2. Observations of MHD turbulence

The first evidence for turbulent fluctuations in solar wind was found by *Coleman* [1968] who, using Mariner 2 observations, investigated the statistics of interplanetary magnetic field fluctuations during August 27 - October 31, 1962. By analyzing spectral densities, he concluded that the solar wind flow is often turbulent, the energy being distributed over a very wide frequency range, from one cycle per solar rotation up to 0.1 Hz. The frequency spectrum, in a range of intermediate frequencies ( $2 \times 10^{-5} - 2.3 \times 10^{-3}$ ), was found to behave roughly as  $f^{-1.2}$ , i.e., less steeply than predicted by the IK model.

Recently *Podesta et al.* [2007] revisited the problem of the spectral exponents of magnetic energy spectra in the solar wind. They chose several time intervals between 1995 and 2003 lasting 2 to 3 solar rotations during which WIND spacecraft recorded the solar wind velocity and the magnetic field. Figure 5.2 shows the results obtained for a time interval from November 2000 to February 2001. Quite unexpectedly, these authors found that the power law exponent of magnetic field fluctuations often has a value near  $5/3$ . These results are opposite to the IK model, but agree with the GS model for the perpendicular case.

*Horbury et al.* [2008] studied the anisotropy of the energy spectrum in MHD turbulence taking the magnetic field orientation into account in order to further test the validity of the GS model. They used 30 days of Ulysses magnetic field observations (days 100-130 in 1995) with a time resolution of 1 second. At that time, Ulysses was at 1.4 AU from the Sun and immersed in the steady high speed solar wind coming from the Sun's northern polar coronal hole. They studied the anisotropy of turbulence by measuring how the spectrum of magnetic fluctuations in the spacecraft frame varies with  $\theta_B$ , and showed that for angles larger than about  $45^\circ$  the spectral index fluctuates around  $-5/3$ , while for smaller angles it approaches to a value of  $-2$ , in a good agreement with the GS model.

The solar wind is a magnetized compressible plasma flow. In supersonic compressible turbulence, the fluctuations tend to steepen into shock waves, where

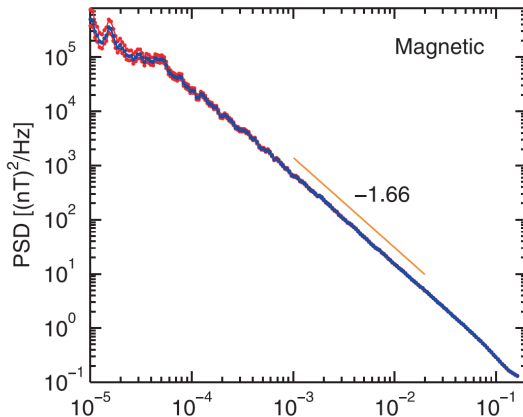


Fig. 5.2. Magnetic field energy spectrum obtained by *Podesta et al.* [2007] using 81 days of Wind data from November 2000 to February 2001.

dissipation may occur in one jump, without having to go through an intermediary cascade, as in the Kolmogorov scheme. The solar wind plasma is also collisionless, so the dissipation is expected to be driven by waves and instabilities rather than the ordinary viscosity. Recent studies argue that, due to the high complexity of solar wind plasma, the mutual interaction and merging of coherent structures (e.g. Alfvén solitons, resonances, pseudo-equilibrium structures, etc.) leads to turbulence and may also play a crucial role in dissipating energy in the coarse grained sense [*Chang, 2015*].

Recent efforts for a systematic investigation of solar wind turbulence over the last two solar cycles have been made within the STORM FP7 project [*STORM, 2015*]. The project investigates how the features of turbulence vary with the solar activity by analyzing in-situ satellite measurements. A package of advanced nonlinear analysis methods are applied on selected data sets, including: power spectral densities (PSD), probability distribution functions (PDF), the partition function multifractal analysis (PFMA) and the rank ordered multifractal analysis (ROMA). The computer programs are embedded in a graphical user interface, creating a user-friendly environment used to compute and visualize the results of the different analyses. Within STORM, the author is actively involved in the development of the software library cumulating the programs developed to implement the above mentioned analysis methods.

## 6. Analysis methods and tools

In this Chapter we present the main analysis methods and tools used in the original publications. We also present a brief mathematical background. All the analysis codes were developed within the MATLAB computing environment. For some analyses we constructed dedicated graphical user interfaces (GUIs) in order to streamline the analysis and to facilitate the cross-validation and reproducibility of our results. The Chapter is divided into 3 Sections: 6.1 Discontinuity analysis, 6.2 Wavelet denoising and 6.3 Spectral analysis.

### 6.1. Discontinuity analysis

Papers I to III are dedicated to the analysis of solar wind discontinuities. In Paper I we studied the propagation delay between ACE and Cluster 3 (C3) spacecraft for more than 200 discontinuities. We compared the observed time delay with the propagation time estimated by various single spacecraft methods, based on estimating the surface boundary normal, using ACE magnetic field data. Paper II proposes a new method of improving boundary normal estimation by using wavelet denoising techniques to remove low-amplitude high-frequency fluctuations, which are known to affect the boundary normal estimation accuracy. Paper III expanded the database of discontinuities observed by both ACE and C3 to more than 400 events during 2001-2012 and studied the time delay and its accuracy obtained by the same methods as those used in Paper I. In Paper III we also studied the effect of wavelet denoising on the accuracy of these methods. In the following we will briefly describe the boundary normal estimation methods and present the analysis tool developed to obtain the results of the various studies.

Solar wind discontinuities are often approximated by locally planar structures tilted at an arbitrary angle with respect to the Sun-Earth line. The configuration of a solar wind discontinuity propagating from ACE to C3 is illustrated in Fig. 6.1. The tilt of the discontinuity with respect to the flow direction, referred to as  $\theta$  angle, and the displacement of the two satellites from the Sun-Earth line can have an important influence on the estimated time delay between the two

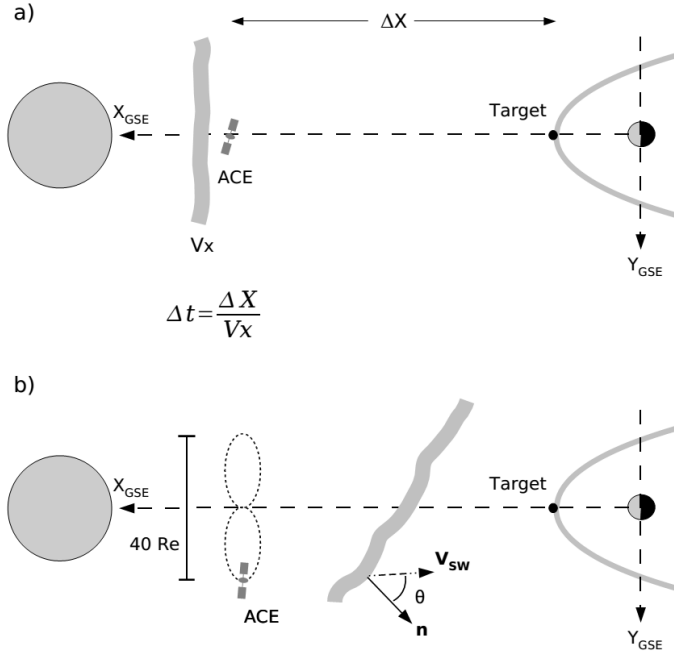


Fig. 6.1. Illustration of the two principal methods to calculate the solar wind propagation delay. (a) Flat delay: A planar structure is assumed to propagate with a constant velocity along the Sun-Earth line. Both the solar wind monitor (ACE) and the target (typically the Earth's upstream magnetopause) are assumed to lie on the Sun-Earth line. (b) The real position of the solar wind monitor as well as the orientation of the IMF phase front, represented by its boundary normal  $\mathbf{n}$ , and the measured solar wind velocity vector,  $\mathbf{V}_{SW}$  are taken into account.  $\theta$  is the angle between the phase front normal and the solar wind velocity.

satellites. Assuming that the propagation speed of the discontinuity is given by the projection of the solar wind velocity vector  $\mathbf{V}_{SW}$  onto the boundary normal direction  $\mathbf{n}$ , and that the relative distance between the two observation points with respect to the discontinuity is the observed distance  $\mathbf{D}$  projected onto  $\mathbf{n}$ , the time delay  $dt$  between the two points is given by:

$$dt = \frac{\mathbf{D} \cdot \mathbf{n}}{\mathbf{V}_{SW} \cdot \mathbf{n}} \quad (6.1)$$

In Papers I and III we used three boundary normal estimation methods : Cross Product (CP) [Colburn and Sonett, 1966], Minimum Variance Analysis of the magnetic field (MVAB) and Constrained minimum variance analysis (MVAB0) (see, e.g., Sonnerup and Scheible, 1998).

The CP method assumes that the discontinuity normal is given by the cross

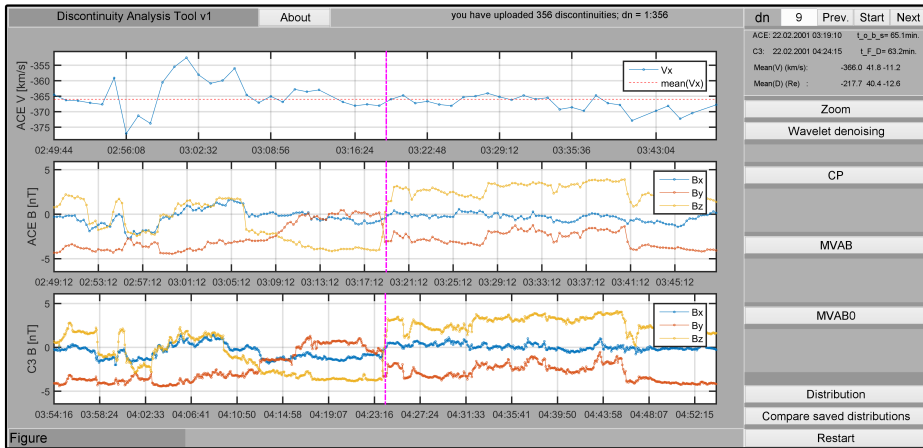


Fig. 6.2. Discontinuity Analysis Tool (DAT). The top plot shows the  $V_x$  component of the solar wind speed measured by ACE. The middle and bottom plots show the three components of the magnetic field ( $\mathbf{B}_x$  - blue,  $\mathbf{B}_y$  - red and  $\mathbf{B}_z$  - yellow) measured by ACE and by Cluster (C3). The magenta line spanning the three plots marks the time of the discontinuity at the two satellites. The user interface controls in the right part of the figure are discussed in text.

product between the mean upstream magnetic field  $\mathbf{B}_1$  and the mean downstream magnetic field  $\mathbf{B}_2$ :

$$\mathbf{n}_{CP} = \frac{\mathbf{B}_1 \times \mathbf{B}_2}{|\mathbf{B}_1 \times \mathbf{B}_2|}. \quad (6.2)$$

MVAB is the most frequently used method to obtain the orientation of a planar magnetic field structure. One first computes the eigenvectors and eigenvalues of the covariance matrix of magnetic field measurements,  $\mathbf{M}_{\nu\mu}$ :

$$\mathbf{M}_{\nu\mu} = \langle \mathbf{B}_\mu \mathbf{B}_\nu \rangle - \langle \mathbf{B}_\mu \rangle \langle \mathbf{B}_\nu \rangle, \quad (6.3)$$

where  $\langle \dots \rangle$  denotes averaging over a certain time interval centered on the discontinuity. The eigenvector corresponding to the smallest eigenvalue is considered an estimator for the boundary normal  $\mathbf{n}_{MVAB}$ .

Assuming that most solar wind discontinuities have properties specific for tangential discontinuities [Knetter, 2005], we can estimate the boundary normal using the constrained minimum variance analysis (MVAB0), where the normal magnetic field is zero by definition. In MVAB0, the covariance matrix  $\mathbf{M}_{\nu\mu}$  of Eq. 6.3 is replaced by:

$$\mathbf{Q}' = \mathbf{P}_{ik} M_{\nu\mu} \mathbf{P}_{nj}, \text{ with: } \mathbf{P}_{ij} = \delta_{ij} - \mathbf{b}_i \mathbf{b}_j, \quad (6.4)$$

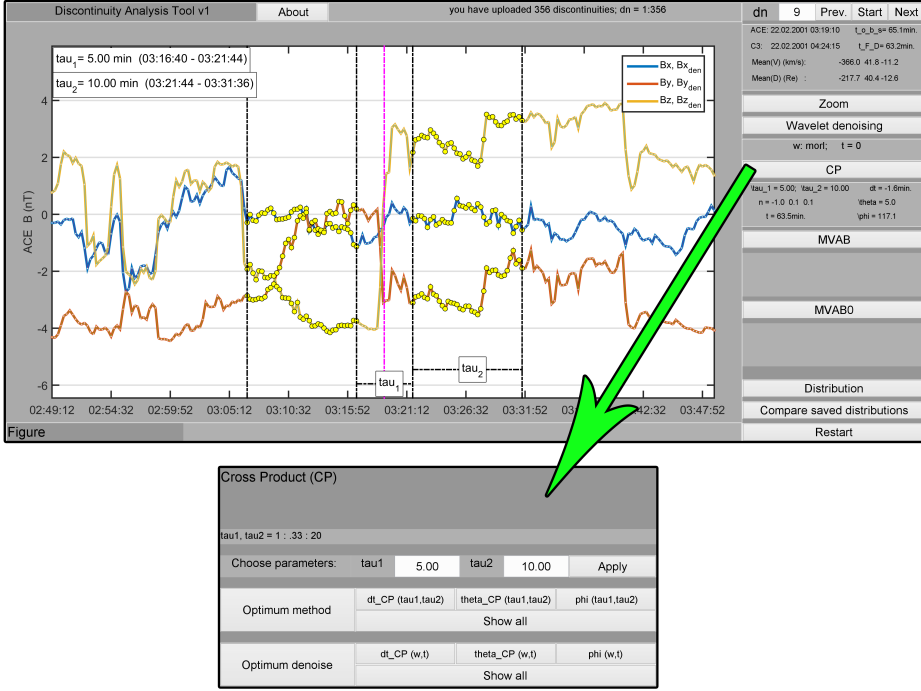


Fig. 6.3. Part of DAT: user interface panels for the Cross Product method. Top panel shows the graphical representation of the results, and bottom panel shows the user interface controls.

where  $\delta_{ij} = 1$  for  $i = j$  and 0 otherwise (Kronecker delta), and  $\mathbf{b} = \langle \mathbf{B} \rangle / |\langle \mathbf{B} \rangle|$  is the unit vector in the direction of the average magnetic field. The time interval centered on the discontinuity and used to calculate the covariance matrix  $\mathbf{Q}'$  is a free parameter in MVAB0.

In order to obtain the results presented in Paper III, we developed a dedicated software tool, the Discontinuity Analysis Tool (DAT). The analysis methods described above are embedded in a graphical user interface, which gives the user a very flexible way of computing the results.

Figure 6.2 shows the main graphical user interface of DAT. The central part of the interface shows the graphical representation of the results and the right part contains the user interface controls. The top part is the discontinuity selection part, where the user can choose one of the events in the database by setting the value for the discontinuity number ( $dn$ ), and easily visualize and navigate through discontinuities with the “next” and “previous” buttons. The discontinuity presented here corresponds to the event  $dn = 9$ , and was observed by ACE at  $t_{ACE} = 03 : 19 : 10 UT$  and by C3 at  $t_{C3} = 04 : 24 : 15 UT$  on 22.02.2001. The observed time delay ( $t_{obs} = t_{C3} - t_{ACE}$ ) for this event is 65.1 min. The propagation

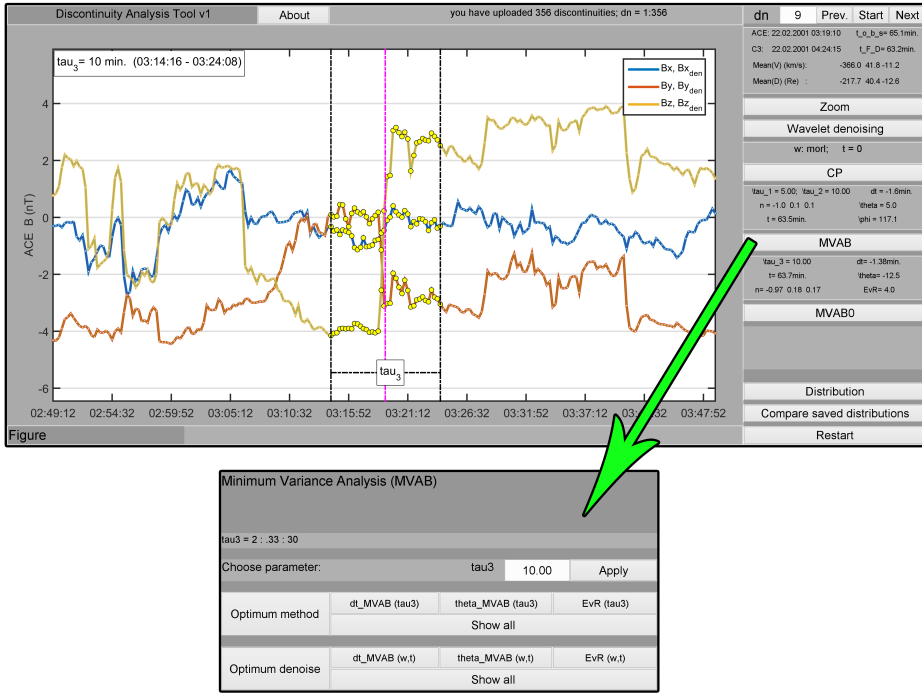


Fig. 6.4. Part of DAT: user interface panels for the Minimum Variance Analysis method. Top panel shows the graphical representation of the results, and bottom panel shows the user interface controls.

time estimated using the Flat Delay method ( $t_{FD}$ ), the mean solar wind velocity and the mean distance between the two satellites are also given in the top right part of Fig. 6.2. The “Zoom” button can be used to zoom-in or -out around the discontinuity. The “Wavelet denoising” button can be used to remove noise from the data using wavelet denoising (see Section 6.2 for details).

After this initial preprocessing part, one can test and compare the propagation delay models presented above. Figures 6.3 and 6.4 show the graphical results and the user interface panels for the CP and MVAB methods. CP analysis has two parameters:  $\tau_1$ , the time interval in minutes, centered on the discontinuity, and  $\tau_2$ , the time interval used to compute the mean magnetic field. For MVAB, the only controlling parameter is  $\tau_3$ , and it is defined in a similar way to  $\tau_1$ . MVAB0 (not shown), is implemented in DAT in a similar way to MAVB, with the analyzed time interval being denoted as  $\tau_4$ . The buttons labeled “Optimum method”, shown in the bottom panels of Figures 6.3 and 6.4, can be used to compute the optimum time intervals for the two methods. In the case of the CP method, for example, the parameters  $\tau_1$  and  $\tau_2$  are varied from 2 to 10 min, with a step size of 1/3 min (see also Fig. 3 of Paper III). The optimum set

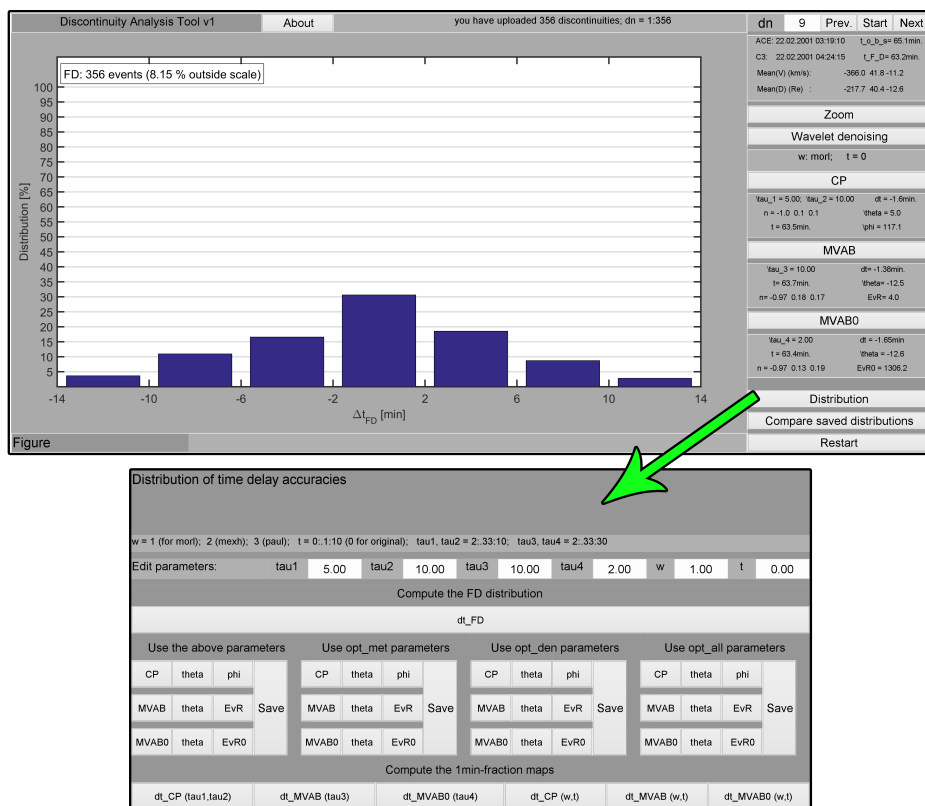


Fig. 6.5. Part of DAT: user interface panels used to visualize and save the distributions of time delay accuracy.

of parameters is the one corresponding to the minimum value of the time delay accuracy  $\Delta t_{CP}(\tau_1, \tau_2) = dt_{CP}(\tau_1, \tau_2) - t_{obs}$ , where  $dt_{CP}$  is the time delay estimated using the CP method. Similar determinations of the optimum method parameters are also implemented for MVAB and MVAB0. A similar optimization procedure can also be implemented to optimize the set of wavelet denoising parameters. Using the “Optimum denoise” buttons, shown in the bottom panels of Figures 6.3 and 6.4, one can determine the set of wavelet denoising parameters that minimizes the time delay accuracy  $\Delta t_{CP}(w, p) = dt_{CP}(w, t) - t_{obs}$ , where  $w$  denotes the wavelet function and  $p$ , the threshold parameter (see Section 6.2 for details).

DAT also contains a section dedicated to the analysis of time delay accuracy  $\Delta t_{met}$ , where “met” denotes one of the three methods (CP, MVAB, or MVAB0), for all discontinuities. Figure 6.5 shows the user interface panels dedicated to the analysis of time delay accuracy. Using the  $dt_{FD}$  button, one can compute the

distribution of time delay accuracy obtained using the simple Flat Delay method (also see Fig 6.1a). DAT can also compute the time delay accuracy distributions for CP, MVAB and MVAB0 using various method or wavelet denoising parameters (see the various buttons in the bottom panel of Fig. 6.5).

As a final remark, the Discontinuity Analysis Tool was instrumental not only in obtaining the results, but also in guiding us towards the conclusions expressed in Paper III. We first initiated the study with the hope of finding a fixed set of wavelet denoising parameters, for which the time delay accuracy would be significantly improved. DAT, with its flexible user interface, helped us in testing in a systematic way the range of possible parameters. This lead us to conclude that using only a fixed set of denoising parameters for all discontinuities in our database, does not lead to an overall improvement of time delay accuracy. This result shows that the internal structure of discontinuities, i.e., the small scale fluctuations, is variable, which has an impact on time delay accuracy. By using an optimum set of denoising parameters for each discontinuity, we determined that MVAB gives the best estimates for time delay accuracy, predicting almost 90% of discontinuities to within  $\pm 2$  min of the observed time delay.

## 6.2. Wavelet denoising

Wavelet denoising is a powerful technique, bearing similarities with frequency filtering. Instead of removing frequency components from the signal, wavelet denoising removes certain wavelet coefficients based on their amplitude.

In wavelet denoising, one first computes the continuous wavelet transform of a time series  $f(t)$ , using:

$$T(a, b) = \int_{-\infty}^{\infty} f(t)\psi^{a,b}(t) dt, \quad \text{with } \psi^{a,b}(t) = a^{-1/2}\psi\left(\frac{t-b}{a}\right) \quad (6.5)$$

where  $a$  is the scale parameter,  $b$  is the translation parameter,  $\psi$  is the wavelet mother function and  $T(a, b)$  is the wavelet coefficient matrix (see, e.g., *Daubechies*, 1992, for more details).

The next step is to remove a part of the wavelet coefficients. This is motivated by the fact that the large-amplitude low-frequency components of the time series and the small-amplitude high-frequency ones (the “noise”) occupy different amplitude ranges in the coefficient matrix  $T(a, b)$ . We used hard thresholding in wavelet denoising, in which all coefficients below a certain amplitude level were set to zero. The threshold amplitude level  $p$  was defined as a percentage of the total amplitude range of the coefficient matrix. The denoised coefficient matrix is defined as:

$$T^d(a, b) = \begin{cases} T(a, b) & , \text{ if } |T(a, b)| > (p/100) \cdot \max(|T(a, b)|), \\ 0 & , \text{ if } |T(a, b)| \leq (p/100) \cdot \max(|T(a, b)|). \end{cases} \quad (6.6)$$

The final step is to perform the inverse wavelet transform:



Fig. 6.6. Part of DAT: user interface panels used for wavelet denoising.

$$f^d(t) = C_\psi \int_a \int_b a^{-2} T^d(a, b) \psi^{a, b}(t) da db, \quad (6.7)$$

where  $C_\psi$  is a constant depending only on the wavelet mother function  $\psi$  (see, e.g. *Torrence and Compo, 1998*).

An important factor to be considered in wavelet analysis is the wavelet shape, which should reflect the type of features present in the time series. Paper III tested three wavelet functions: Morlet, Paul and the Mexican Hat. Another important free parameter in wavelet denoising is the threshold level  $p$ .

Figure 6.5 shows the user interface panels for the wavelet denoising implemented in DAT. The wavelet function can be chosen by setting the value of  $w$  to 1 (for Morlet), 2 (for the Mexican Hat), and 3 (for Paul). The threshold parameter, denoted in DAT as  $t$ , can also be changed, or it can be set to zero in order to use the original time series.

### 6.3. Spectral analysis

Spectral analysis is a widely used tool in many fields of science, with ready-made toolboxes in most modern packages of statistical analysis software. The Fast Fourier Transform algorithm, which is extremely fast and reliable, is the most

popular method to compute the Fourier Transform  $y(\omega)$ , which, for a given signal  $x(t)$ , is defined as:

$$y(\omega) = \int_{-\infty}^{+\infty} x(t)e^{-i\omega t} dt \quad (6.8)$$

The simplest technique to estimate the power spectral density (PSD) is the Periodogram, defined as the modulus squared of  $y(\omega)$ . Despite its simplicity, the Periodogram suffers from severe deficiencies like, e.g., high variance and spectral leakage. The abrupt behavior at the edges of the rectangular window used in computing the Periodogram causes a leakage of energy from the dominant peaks to other frequencies. This is addressed by using a windowing procedure to reduce the effect of spectral leakage. The Periodogram computed using various window functions is called a Modified Periodogram. Variance of the Modified Periodogram is a major drawback, e.g., in estimating the spectral index, i.e., the power-law slope of PSD as a function of frequency. One way of reducing this variance is to use Welch's method of Averaged Modified Periodograms [Welch, 1967]. The method first divides the time series into a number of segments, computes the Modified Periodogram for each segment, and then calculates the PSD as the ensemble average of the Modified Periodograms. The window function used to calculate the Modified Periodogram, as well as the segment length and possibly an overlap between adjacent segments are free parameters of the method, and can be used to increase or decrease the variance of the PSD to match the needs of the specific applications.

Paper IV uses the Welch method to compute PSDs from Venus Express observations of magnetic field fluctuations during the deep minimum of solar cycle 23 (2007-2009). The Welch method parameters used are: a Hamming window function and a segment length of 2048 points with a 90% overlap between adjacent segments.

The Fast Fourier transform requires a strictly uniform sampling and no data gaps. Small data gaps can be filled-in using a simple linear interpolation procedure, but large gaps, or multiple data gaps distributed throughout the time series, can have an important negative effect on the PSD. In Paper IV, for example, from a total of 1094 orbits between January 2007 and December 2009, only 204 time intervals satisfied the data quality requirements (time intervals longer than 1 hour and data gaps smaller than 30 consecutive points). This means that more than 80% of the dataset had to be discarded from the analyses, mostly due to large data gaps.

In Paper V, we address the very common problems of data gaps and non-uniform sampling. In addition to the FFT method described above, we also test three other methods of estimating the amplitude spectrum: the Discrete Fourier Transform (DFT), the Z-Transform (ZTR) and the Lomb-Scargle algorithm (LST).

The DFT and the ZTR methods are quite similar and they are both often referred to as the Discrete Fourier Transform. DFT is a simple discretization of the Fourier integral (Eq. 6.8), which we chose to do using the trapezoidal method:

$$y(\omega) = \sum_{j=1}^n x(t_j)e^{-i\omega t_j} \Delta t_j / 2 \quad (6.9)$$

The Z transform is a generalization of the Fourier Transform for discrete series:

$$y(\omega) = \sum_{j=1}^n x(t_j) e^{-i\omega t_j} \quad (6.10)$$

The Lomb-Scargle method performs a least squares fit of the data using a superposition of sinusoidal modes [*Lomb*, 1976; *Scargle*, 1982, 1989; *Hocke and Kämpfer*, 2009].

Paper V applies these methods to two datasets: a synthetic dataset composed of a simple superposition of four sinusoidal modes and magnetic field measurements made by the Venus Express spacecraft in orbit around the planet Venus. The datasets are altered by introducing various gap configurations, and then comparing the original spectrum (computed without gaps) with the spectrum of the altered signals. The results show that the simple interpolation procedure often used in practice, can have a significant distorting effect on the resulting spectrum, depending on the length and/or distribution of data gaps.

## 7. Summary

This thesis presents a study on solar wind microstructure. The term microstructure used throughout the thesis, is defined as the range of time scales between 36 sec and 1 hour [Burlaga, 1969]. The main topics addressed are the solar wind discontinuities, solar wind turbulence and related methods and analysis tools.

Paper I deals with the propagation delay of solar wind discontinuities. The propagation delays between the ACE spacecraft orbiting the L1 libration point and the Cluster C3 spacecraft near the Earth's magnetopause for almost 200 discontinuities during 2001-2007 are compared with the predicted times from four propagation models. The models include the simple convection of solar wind disturbances along the Sun-Earth line, the Flat Delay (FD) method, and three more advanced models, which take into account the orientation of the discontinuity as well as the real positions of the two spacecraft: cross product (CP) method, the minimum variance analysis of the magnetic field (MVAB), and the constrained minimum variance analysis (MVAB0) method. The results show that the advanced methods give more precise time delay estimations in most cases, and that the best predictions are obtained using the MVAB0 method.

In Paper II we point out some undesirable effects of the MVAB based propagation delay calculation presented in *Pulkkinen and Rastätter* [2009] (hereafter PR09). We show that, the sometimes dominant normal magnetic field component and the fact that sharp changes in the IMF are not allowed, contradict our present understanding of directional discontinuities in the solar wind. We suggest that any attempt to remove the effect of small scale fluctuations, known to affect boundary normal estimations using MVAB, should be done on the input data, rather than on the estimated boundary normals like in PR09. One way to achieve this is through the use of wavelet denoising technique.

Paper III expands the database of discontinuities studied in Paper I to 356 events during 2001-2012 and also studies the effect of wavelet denoising of the propagation delay accuracy. We find that the free parameters of the three methods have to be adapted to each event in order to obtain accurate propagation delays. We also find that by using denoising parameters optimized to each event, 88% of our database are estimated to arrive within  $\pm 2$ min from the observed time delay with MVAB, 74% with CP and 69% with the MVAB0 method. This shows that

wavelet denoising significantly improves the prediction of the propagation time delay of solar wind discontinuities.

In paper IV we investigate Venus Express observations of solar wind magnetic field fluctuations during the minimum of solar cycle 23 (2007-2009). We show that power spectral densities for the fast solar wind have higher levels of power than the slow solar wind. The spectral slopes in the inertial range are shown to exhibit a normal distribution, with average values of:  $\alpha_x^{fast} = -1.57 \pm 0.02$ ,  $\alpha_y^{fast} = -1.58 \pm 0.02$ ,  $\alpha_z^{fast} = -1.60 \pm 0.02$ ,  $\alpha_x^{slow} = -1.67 \pm 0.01$ ,  $\alpha_y^{slow} = -1.64 \pm 0.01$ , and  $\alpha_z^{slow} = -1.64 \pm 0.01$ , with  $\alpha_i^{fast/slow}$  indicating the mean spectral index of magnetic i component and the fast or slow type of wind. We also show the variation of the spectral index as a function of the solar wind speed, and find that the spectral indices of the magnetic field become shallower (less steep) with increasing plasma velocity.

Paper V studies the effect of data gaps to four commonly used methods of estimating the amplitude spectrum of a time series: Fast Fourier Transform, Discrete Fourier Transform, Z-Transform and Lomb-Scargle algorithm. We applied several configurations of data gaps to two datasets: a synthetic dataset composed of a superposition of four sinusoidal modes and the magnetic field measured by Venus Express, and compared the results for the altered dataset with the original results. For single data gaps, FFT and DFT are shown to give an amplitude decreasing with increasing gap size, while the shape of spectrum remains almost unmodified even for large data gaps. On the other hand, ZTR and LST are shown to preserve the absolute level for increasing gap size. We also analyze time series with multiple small data gaps randomly distributed throughout the time series. In this case, we show that DFT, ZTR and LST can estimate the correct amplitudes of sinusoidal modes even for large data gap percentage. However, for the more turbulent case of the VEX dataset, these three methods seriously overestimate the high-frequency part of the spectrum above a threshold depending on the maximum gap size.

## References

- ACE, [http://www.srl.caltech.edu/ace/ace\\_mission.html](http://www.srl.caltech.edu/ace/ace_mission.html), 2015, accessed: August, 2015.
- Archer, M. O., T. S. Horbury, and J. P. Eastwood, Magnetosheath pressure pulses: Generation downstream of the bow shock from solar wind discontinuities, *Journal of Geophysical Research: Space Physics*, *117*, n/a–n/a, 2012.
- Balogh, A., et al., The Cluster Magnetic Field Investigation: overview of in-flight performance and initial results, *Annales Geophysicae*, *19*, 1207–1217, 2001.
- Barabash, S., et al., The analyzer of space plasmas and energetic atoms (aspera-3) for the mars express mission, *Space Science Reviews*, *126*, 113–164, 2006.
- Borovsky, J. E., Flux tube texture of the solar wind: Strands of the magnetic carpet at 1 AU?, *Journal of Geophysical Research (Space Physics)*, *113*, 8110, 2008.
- Bruno, R., and V. Carbone, The solar wind as a turbulence laboratory, *Living Reviews in Solar Physics*, *10*, 2013.
- Burlaga, L., Micro-scale structures in the interplanetary medium, *Solar Physics*, *4*, 67–92, 1968.
- Burlaga, L., Hydromagnetic waves and discontinuities in the solar wind, *Space Science Reviews*, *12*, 600–657, 1971.
- Burlaga, L., and N. Ness, Tangential discontinuities in the solar wind, *Solar Physics*, *9*, 467–477, 1969.
- Burlaga, L. F., Directional Discontinuities in the Interplanetary Magnetic Field, *Solar Physics*, *7*, 54–71, 1969.
- Burlaga, L. F., *Interplanetary magnetohydrodynamics.*, vol. 3, Oxford University Press, 1995.
- Burlaga, L. F., J. D. Scudder, L. W. Klein, and P. A. Isenberg, Pressure-balanced structures between 1 au and 24 au and their implications for solar wind electrons and interstellar pickup ions, *Journal of Geophysical Research: Space Physics*, *95*, 2229–2239, 1990.
- CDAWeb, <http://cdaweb.gsfc.nasa.gov/>, 2015, accessed: September, 2015.

- Chang, T. T. S., *An Introduction to Space Plasma Complexity*, Cambridge University Press, 2015.
- Cluster, <http://sci.esa.int/cluster/47348-fact-sheet>, 2015, accessed: August, 2015.
- Colburn, D. S., and C. P. Sonett, Discontinuities in the Solar Wind, *Space Sci. Rev.*, *5*, 439–506, 1966.
- Coleman, P. J., Jr., Turbulence, Viscosity, and Dissipation in the Solar-Wind Plasma, *The Astrophysical Journal*, *153*, 371, 1968.
- Daubechies, I., *Ten Lectures on Wavelets*, Cbms-Nsf Regional Conference Series in Applied Mathematics, Society for Industrial and Applied Mathematics, 1992.
- Dungey, J. W., Interplanetary Magnetic Field and the Auroral Zones, *Physical Review Letters*, *6*, 47–48, 1961.
- Escoubet, C. P., M. Fehringer, and M. Goldstein, Introduction: The cluster mission, *Annales Geophysicae*, *19*, 1197–1200, 2001.
- Farge, M., Wavelet transforms and their applications to turbulence, *Annual Review of Fluid Mechanics*, *24*, 395–457, 1992.
- Frisch, U., *Turbulence. The legacy of A. N. Kolmogorov.*, Cambridge University Press, Cambridge (UK), 1995.
- Goldreich, P., and S. Sridhar, Toward a theory of interstellar turbulence. 2: Strong alfvenic turbulence, *The Astrophysical Journal*, *438*, 763–775, 1995.
- Hocke, K., and N. Kämpfer, Gap filling and noise reduction of unevenly sampled data by means of the lomb-scargle periodogram, *Atmospheric Chemistry and Physics*, *9*, 4197–4206, 2009.
- Horbury, T. S., D. Burgess, M. Fränz, and C. J. Owen, Three spacecraft observations of solar wind discontinuities, *Geophys. Res. Lett.*, *28*, 677–680, 2001a.
- Horbury, T. S., D. Burgess, M. Fränz, and C. J. Owen, Prediction of Earth arrival times of interplanetary southward magnetic field turnings, *J. Geophys. Res.*, *106*, 30,001–30,010, 2001b.
- Horbury, T. S., M. Forman, and S. Oughton, Anisotropic Scaling of Magnetohydrodynamic Turbulence, *Physical Review Letters*, *101*, 175,005, 2008.
- Hudson, P. D., Discontinuities in an anisotropic plasma and their identification in the solar wind, *Planet. Space Sci.*, *18*, 1611–1622, 1970.
- Iroshnikov, P. S., Turbulence of a Conducting Fluid in a Strong Magnetic Field, *Soviet Astronomy*, *7*, 566, 1964.
- Knetter, T., A new perspective of the solar wind micro-structure due to multi-point observations of discontinuities, Ph.D. thesis, Universität zu Köln, 2005.
- Knetter, T., F. M. Neubauer, T. Horbury, and A. Balogh, Four-point discontinuity observations using Cluster magnetic field data: A statistical survey, *Journal of Geophysical Research (Space Physics)*, *109*, 6102, 2004.
- Landau, L. D., and E. M. Lifshitz, *Electrodynamics of continuous media*, Pergamon Press, 1960.

- Lepping, R. P., and K. W. Behannon, Magnetic field directional discontinuities. I - Minimum variance errors, *Journal of Geophysical Research*, *85*, 4695–4703, 1980.
- Lepping, R. P., and K. W. Behannon, Magnetic field directional discontinuities - Characteristics between 0.46 and 1.0 AU, *J. Geophys. Res.*, *91*, 8725–8741, 1986.
- Lomb, N., Least-squares frequency analysis of unequally spaced data, *Astrophysics and Space Science*, *39*, 447–462, 1976.
- Lyons, L. R., S. Liu, J. M. Ruohoniemi, S. I. Solov'yev, and J. C. Samson, Observations of dayside convection reduction leading to substorm onset, *Journal of Geophysical Research (Space Physics)*, *108*, 1119, 2003.
- Matthaeus, W. H., M. Wan, S. Servidio, A. Greco, K. T. Osman, S. Oughton, and P. Dmitruk, Intermittency, nonlinear dynamics and dissipation in the solar wind and astrophysical plasmas, *Philosophical Transactions of the Royal Society of London A: Mathematical, Physical and Engineering Sciences*, *373*, 2015.
- McComas, D. J., S. J. Bame, P. Barker, W. C. Feldman, J. L. Phillips, P. Riley, and J. W. Griffee, Solar Wind Electron Proton Alpha Monitor (SWEPAM) for the Advanced Composition Explorer, *Space Sci. Rev.*, *86*, 563–612, 1998.
- McComas, D. J., R. W. Ebert, H. A. Elliott, B. E. Goldstein, J. T. Gosling, N. A. Schwadron, and R. M. Skoug, Weaker solar wind from the polar coronal holes and the whole sun, *Geophysical Research Letters*, *35*, –, 2008.
- McCracken, K. G., and N. F. Ness, The collimation of cosmic rays by the interplanetary magnetic field, *Journal of Geophysical Research*, *71*, 3315–3318, 1966.
- Meyer-Vernet, N., *Basics of the Solar Wind*, Cambridge University Press, 2007.
- Ness, N. F., C. S. Scarce, and S. Cantarano, Preliminary results from the Pioneer 6 Magnetic Field Experiment, , *71*, 3305–3313, 1966.
- Neubauer, F. M., Jump relations for shocks in an anisotropic magnetized plasma, *Zeitschrift fur Physik*, *237*, 205–223, 1970.
- Neugebauer, M., and C. J. Alexander, Shuffling foot points and magnetohydrodynamic discontinuities in the solar wind, *Journal of Geophysical Research: Space Physics*, *96*, 9409–9418, 1991.
- Neugebauer, M., D. R. Clay, B. E. Goldstein, B. T. Tsurutani, and R. D. Zwickl, A reexamination of rotational and tangential discontinuities in the solar wind, *J. Geophys. Res.*, *89*, 5395–5408, 1984.
- Podesta, J. J., D. A. Roberts, and M. L. Goldstein, Spectral Exponents of Kinetic and Magnetic Energy Spectra in Solar Wind Turbulence, *The Astrophysical Journal*, *664*, 543–548, 2007.
- Pross, G. W., *Physics of the Earth's Space Environment: An introduction*, Springer, 2004.
- Pulkkinen, A., and L. Rastätter, Minimum variance analysis-based propagation of the solar wind observations: Application to real-time global magnetohydrodynamic simulations, *Space Weather*, *7*, 12,001, 2009.
- Rème, H., et al., First multispacecraft ion measurements in and near the Earth's magnetosphere with the identical Cluster ion spectrometry (CIS) experiment, *Annales Geophysicae*, *19*, 1303–1354, 2001.

- Richardson, L. F., Weather prediction by numerical process. Cambridge (University Press), *Quarterly Journal of the Royal Meteorological Society*, 48, 282–284, 1922.
- Scargle, J. D., Studies in astronomical time series analysis. II - Statistical aspects of spectral analysis of unevenly spaced data, *Astrophys. J.*, 263, 835–853, 1982.
- Scargle, J. D., Studies in astronomical time series analysis. III - Fourier transforms, autocorrelation functions, and cross-correlation functions of unevenly spaced data, *Astrophys. J.*, 343, 874–887, 1989.
- Siscoe, G. L., L. Davis, Jr., P. J. Coleman, Jr., E. J. Smith, and D. E. Jones, Power spectra and discontinuities of the interplanetary magnetic field: Mariner 4, *J. Geophys. Res.*, 73, 61, 1968.
- Smith, C. W., J. L'Heureux, N. F. Ness, M. H. Acuña, L. F. Burlaga, and J. Scheifele, The ACE Magnetic Fields Experiment, *Space Sci. Rev.*, 86, 613–632, 1998.
- Smith, E. J., Identification of interplanetary tangential and rotational discontinuities, *J. Geophys. Res.*, 78, 2054, 1973.
- Solodyna, C. V., J. W. Sari, and J. W. Belcher, Plasma field characteristics of directional discontinuities in the interplanetary medium, *Journal of Geophysical Research*, 82, 10–14, 1977.
- Sonnerup, B. U. Ö., and M. Scheible, Minimum and Maximum Variance Analysis, *Analysis Methods for Multi-Spacecraft Data*, G. Paschmann, P.W. Daly (Eds.), *ISSI Scientific Reports Series, ESA/ISSI*, 1, 185–220, 1998.
- Stone, E., A. Frandsen, R. Mewaldt, E. Christian, D. Margolies, J. Ormes, and F. Snow, The advanced composition explorer, *Space Sci. Rev.*, 86, 1–22, 1998.
- STORM, <http://www.storm-fp7.eu/>, 2015, accessed: September, 2015.
- SWPC, <http://www.swpc.noaa.gov/products/ace-real-time-solar-wind>, 2015, accessed: September, 2015.
- Titov, D. V., E. Lellouch, F. Taylor, L. Marinangeli, H. Opgenoorth, and VEX Team, Venus express: An orbiter for the study of the atmosphere, the plasma environment, and the surface of venus, mission definition rep. esa-sci, *Eur. Space Agency*, 6, –, 2001.
- Torrence, C., and G. P. Compo, A practical guide to wavelet analysis, *Bulletin of the American Meteorological Society*, 79, 61–78, 1998.
- Tsurutani, B. T., and C. M. Ho, A review of discontinuities and Alfvén waves in interplanetary space: Ulysses results, *Reviews of Geophysics*, 37, 517–524, 1999.
- Tsurutani, B. T., and E. J. Smith, Interplanetary discontinuities - Temporal variations and the radial gradient from 1 to 8.5 AU, *J. Geophys. Res.*, 84, 2773–2787, 1979.
- VEX, <http://sci.esa.int/venus-express/47115-fact-sheet>, 2015, accessed: August, 2015.
- Zhang, T., et al., Magnetic field investigation of the venus plasma environment: Expected new results from venus express, *Planetary and Space Science*, 54, 1336 – 1343, 2006.

Original publications



# Paper I



# What is the best method to calculate the solar wind propagation delay?

B. Mailyan<sup>1</sup>, C. Munteanu<sup>2</sup>, and S. Haaland<sup>3,\*</sup>

<sup>1</sup>Yerevan State University, Armenia

<sup>2</sup>Alexandru Ioan Cuza, University Iasi, Romania

<sup>3</sup>University of Bergen, Norway

\*also at: Max-Planck Institute for Solar Systems, Germany

Received: 2 April 2008 – Revised: 29 May 2008 – Accepted: 2 June 2008 – Published: 5 August 2008

**Abstract.** We present a statistical study of propagation times of solar wind discontinuities between Advanced Composition Explorer (ACE) spacecraft orbiting the L1 libration point and the Cluster quartet of spacecraft near the Earth's magnetopause. The propagation times for almost 200 events are compared with the predicted times from four different models. The simplest model assumes a constant convective motion of solar wind disturbances along the Sun-Earth line, whereas more sophisticated models take the orientation of the discontinuity as well as the real positions of the solar wind monitor and target into account. The results show that taking orientation and real position of the solar wind monitor and target into account gives a more precise time delay estimation in most cases. In particular, we show that recent modifications to the minimum variance technique can improve the estimation of propagation times of solar wind discontinuities.

**Keywords.** Interplanetary physics (Discontinuities; Interplanetary magnetic fields; Instruments and techniques)

## 1 Introduction

Disturbances in Earth's magnetosphere, like e.g. aurora, magnetospheric storms and substorms, are often associated with disturbances in the solar wind, in particular directional changes in the interplanetary magnetic field (IMF). At the Earth's dayside magnetopause, a southward directed IMF can reconnect with the geomagnetic field, and allow energy and momentum to be transferred from the solar wind into the magnetosphere, and set up a large scale circulation of plasma in the magnetosphere (Dungey, 1961). It has also been argued that sudden northward turnings of the IMF can alter the magnetospheric equilibrium, and act as a trigger for mag-

netospheric substorms (Sergeev et al., 1986; Lyons, 1996; Lyons et al., 2003). The study of such interactions requires an exact timing of the IMF change at the Earth's dayside magnetopause.

A challenge in this connection is that solar wind measurements are usually taken at large distances away from Earth, for example by the Advanced Composition Explorer (ACE) spacecraft, and has to be time shifted in order to be representative for the Earth's upstream magnetopause. For ACE, the typical time shift to the Earth is of the order of one hour, depending on the solar wind speed. Although many studies have used one hour as a rule of thumb, a more careful approach requires observations from the solar wind, and then time shift the observations accordingly to be representative for the conditions at the frontside magnetopause.

Earlier studies, e.g. Ridley (2000); Horbury et al. (2001a,b); Weimer et al. (2002, 2003); Weimer and King (2008) have emphasized that not only the solar wind speed, but also the orientation of the IMF plays an important role for the propagation delay.

Horbury et al. (2001a) used data from the ACE spacecraft orbiting the L1 libration point and the Wind spacecraft closer to the Earth to study the propagation times of IMF discontinuities. Although they only considered IMF discontinuities with distinct southward turnings, they found that the best estimates of the propagation times were obtained if the orientation for each discontinuity was calculated from the cross product of the upstream and downstream magnetic field.

Weimer et al. (2003); Weimer and King (2008) took a different approach. They emphasized that knowledge about the IMF direction is important for any time intervals – not only during intervals with distinct discontinuities. In particular, the concurrent IMF direction (and partly also the time history of the solar wind) upstream of the Earth's magnetopause is used to parameterize magnetic field models (Tsyganenko, 2002a,b) and simulation models (e.g. Ogino et al., 1994; Gombosi et al., 2000). Likewise, statistical studies

*Correspondence to:* B. Mailyan  
(bagrat.mailyan@yahoo.co.uk)

of magnetospheric convection (e.g. Papitashvili and Rich, 2002; Weimer, 2005; Ruohoniemi and Greenwald, 2005, and references therein) sort the results according to concurrent IMF direction. Weimer et al. (2003) applied a running minimum variance analysis technique to determine the orientation of the IMF for each data point in a continuous time series of magnetic field data. The obtained normal, together with the solar wind velocity and spacecraft position is then used to predict the time delay between a monitor and a target for each data point. A large data set shifted according to this procedure (although with some modifications – see Sect. 3.2.3 below) is now available in electronic form through NASA's OMNIWEB system ([http://omniweb.gsfc.nasa.gov/html/ow\\_data.html](http://omniweb.gsfc.nasa.gov/html/ow_data.html)). To our knowledge, the first large scale usage of this method to time shift IMF data were the convection studies by Haaland et al. (2007) and Förster et al. (2007).

More recently, Tsurutani et al. (2005) used measurements from ACE and Cluster to study the evolution of 7 distinct interplanetary magnetic field decreases and discontinuities preceded by long periods of strong alfvénic wave activity. 6 of the 7 events were observed at both ACE and Cluster so that the propagation time could be established. Although they primarily focused on the steepening of the wave front during the propagation from ACE to Cluster, they also noted that the structures were essentially convected with the solar wind speed. The difference between the observed propagation time and the time predicted from a convective motion were less than a minute for all 6 cases.

In the present work, we have used data from Cluster mission and the ACE solar wind monitor to study the propagation delay of almost 200 well identified solar wind discontinuities. In particular, we test out the models of Weimer et al. (2003); Weimer and King (2008) on these events.

The paper is organized as follows; In Sect. 2, we give a brief overview of the data sources used in this study. Section 3 contains an overview of the procedures for calculating the time shift, as well as a brief description of the methods used to find the boundary normals of solar wind discontinuities. In Sect. 4, we show a case study and present the statistical results of the study. Section 5 summarizes the paper.

## 2 Data sources

Our primary data sources for this study have been the Advanced Composition Explorer (ACE) spacecraft in the solar wind and the Cluster spacecraft quartet near the Earth's magnetopause.

ACE was put into an approximately  $40 \times 40 R_E$  Lissajous orbit around the L1 libration point some  $1.5 \times 10^6$  km upstream of the Earth in 1998, and have since been frequently used as a solar wind monitor. The expected lifetime of ACE is until 2022, so ACE is going to be an important monitor of the solar wind also the next decade. In this work, we have used IMF data obtained from the ACE magnetic field

instrument (MAG – see Smith et al., 1998), at 16-s resolution and plasma data from the ACE solar wind instrument (SWEPAM – see McComas et al., 1998). at 64-s resolution. These data sets were downloaded via the Coordinated Data Analysis Web (CDAWeb) facility (<http://cdaweb.gsfc.nasa.gov/about.html>).

To check the IMF near the Earth's upstream magnetopause, we have utilized observations from the Cluster satellites. Cluster is a European Space Agency (ESA) project comprising four identical satellites flying in close formation around the Earth. Cluster has a nearly  $90^\circ$  inclination elliptical polar orbit, with perigee at around  $4 R_E$  and apogee around  $20 R_E$  geocentric distance, and an orbital period of approximately 57 h. This orbit takes Cluster into the upstream solar wind during apogee in the months January to March every year. Our study is therefore focused on this season. All Cluster measurements are obtained within an  $Y_{GSE}$  range between  $-8$  to  $+8 R_E$ , and  $X_{GSE}$  positions between approximately  $14 R_E$  and Cluster's apogee around  $20 R_E$ .

Since we focus on IMF discontinuities, we have primarily used measurement from the magnetic field Experiment (FGM – see Balogh et al., 2001), but also data from the Cluster Ion Spectrometry (CIS) Experiment (Rème et al., 2001) were inspected to verify that Cluster was located in the solar wind. The Cluster data used are the official prime parameters with approximately 4-s time resolution, provided by the Cluster Data Center System (CSDS).

Our motivation was primarily to study the solar wind propagation delay, and not the evolution or properties of the solar wind discontinuities as such. We have therefore not utilized Clusters four-spacecraft capability in this study, and most of the Cluster measurements are taken from the C3 spacecraft. However, some of the events included in this work has also been studied by Knetter et al. (2004) and Knetter (2004), where the nature of the discontinuity as well as a comparison of single- and multi spacecraft methods are discussed in detail. In particular, these authors concluded that results based on four-spacecraft triangulation agreed fairly well with the cross product method, which we have also used.

## 3 Methodology

To calculate the exact propagation time of a plasma structure one needs to be able to uniquely identify the same structure at two locations in space. In practice, a reliable identification of a structure is only possible if the observations exhibit a distinct signature which does not change much between the two locations. Interplanetary discontinuities, characterized by sharp changes in the direction or magnitude of the magnetic field are particularly suitable for this purpose. Since the beginning of space age, discontinuities have been extensively studied both from a theoretical view (e.g. Landau and Lifshitz, 1960; Hudson, 1970), but also experimentally (e.g.

Colburn and Sonett, 1966; Siscoe et al., 1968; Turner and Siscoe, 1971; Smith, 1973).

The actual definition of the term discontinuity depends both on the measurements used (plasma, magnetic field or a combination of these) as well as the required change of that parameter. In the following we use the term discontinuity to describe events where we observe pronounced changes in the magnetic field direction within a time interval of less than a minute. As our intention is to study the propagation time, we did not specifically check whether these distinct changes matched the criteria used by, e.g. Tsurutani and Smith (1979) or Lepping and Behannon (1986) to identify discontinuities.

We first identified a large number of time segments containing distinct magnetic field rotations in the Cluster measurements when spacecraft quartet was located in the upstream solar wind. A number of these events could also be identified in the ACE magnetic field measurements. The events were initially selected by visually examining Cluster quick look plots (available at [http://www.cluster.rl.ac.uk/csdswb-cgi/csdswb\\_pick](http://www.cluster.rl.ac.uk/csdswb-cgi/csdswb_pick)). To avoid discontinuities associated with magnetopause crossings or bow-shock activity, we also checked the Cluster nominal position and the CIS ion spectrogram. Only periods with Cluster positions on the dayside, outside the bow shock location which displayed ion temperatures around 1 keV were considered. Cases where the same discontinuity could be observed at both ACE and Cluster were recorded and examined in more detail; The observed time shift between the ACE and Cluster observations were noted and compared to the time shift predicted by various models.

During the years 2001–2007, a total of 198 events with unambiguously matched signatures observed at both ACE and Cluster could be identified from this visual inspection of the data. We should emphasize that these 198 events by no means constitute the complete set of discontinuities for this period, but is a sufficient subset for our study. At this stage, we did not filter out any events, even if we suspected that one or more of the methods would fail or give poor results.

For time delay calculations, we tested four different methods, hereafter referred to as flat delay, cross product, minimum variance and constrained minimum variance. In the following, we give a brief description of each method.

### 3.1 Flat delay

This is the simplest way to estimate the solar wind propagation time between a monitor and a target near the upstream magnetopause. It assumes that a plasma element and the embedded IMF is convected at a constant speed along the Sun-Earth line (i.e. antiparallel to the  $X_{GSE}$  axis) to the Earth's magnetopause. This approach, illustrated in the top panel of Fig. 1, is purely one-dimensional, and does not take into account either orientation of the IMF nor any displacement of

the solar wind monitor away from the Sun-Earth line. The estimated time delay,  $t_{\text{flat}}$ , is then given by

$$t_{\text{flat}} = \frac{\Delta x}{V_x}, \quad (1)$$

where  $\Delta x$  is the distance between the solar wind monitor and the target along the Sun-Earth line, and  $V_x$  is the measured solar wind speed. As the solar wind propagation is predominantly along the  $X_{GSE}$  direction, the approximation  $|V_x| \simeq |V|$  is often used.

Since the method relies on the solar wind velocity only, it can in theory be applied to any time interval where the measurements of the velocity is available – not only time intervals containing distinct IMF discontinuities.

### 3.2 Taking IMF direction into account

As pointed out in e.g. Weimer et al. (2002, 2003), variations in the IMF are often contained in planar structures which are tilted at arbitrary angles with respect to the Sun-Earth line. (Weimer et al., 2003, refers to these tilted planar structures as IMF phase planes). As illustrated the lower panel of Fig. 1, a solar wind monitor displaced from the Sun-Earth line will measure the IMF at a different time (later or earlier, depending on the tilt direction of the phase plane) than it would if it had been located on the Sun-Earth line.

A more realistic calculation of the propagation delay would therefore have to take into account the orientation of these IMF phase planes as well as the real position of the solar wind monitor and target. Also, since the solar wind flow direction can have a significant Y or Z component, the full solar wind velocity vector should be used. Noting that the orientation of a planar structure or discontinuity can be described by its boundary normal,  $\mathbf{n}$ , the time delay can be expressed as:

$$t_d = \frac{(\mathbf{r}_{\text{target}} - \mathbf{r}_{\text{monitor}}) \cdot \mathbf{n}}{\mathbf{V}_{sw} \cdot \mathbf{n}}. \quad (2)$$

Here,  $\mathbf{r}_{\text{target}}$  is the position of the target (typically the upstream magnetopause position at around  $X_{GSE}=10-15 R_E$ ),  $\mathbf{r}_{\text{monitor}}$  is the position of the solar wind monitor, in our case the ACE spacecraft orbiting the L1 libration point, and  $\mathbf{V}_{sw}$  is the measured solar wind velocity.

There are several methods to infer the boundary normal of a plasma boundary. The typical IMF orientation is aligned along the Parker spiral, approximately  $45^\circ$  to the solar wind flow direction. Horbury et al. (2001a) calculated propagation times using both normals parallel and perpendicular to the Parker spiral, but found that these assumptions often gave poorer results than simply assuming a flat delay. More sophisticated methods require in-situ measurements and then trying to estimate the normal from multi spacecraft timing or gradient methods (e.g. Horbury et al., 2001b; Knetter et al., 2004), or use the local field or plasma measurements from a single spacecraft (see e.g. overviews in Sonnerup et al., 2006; Volwerk, 2006).

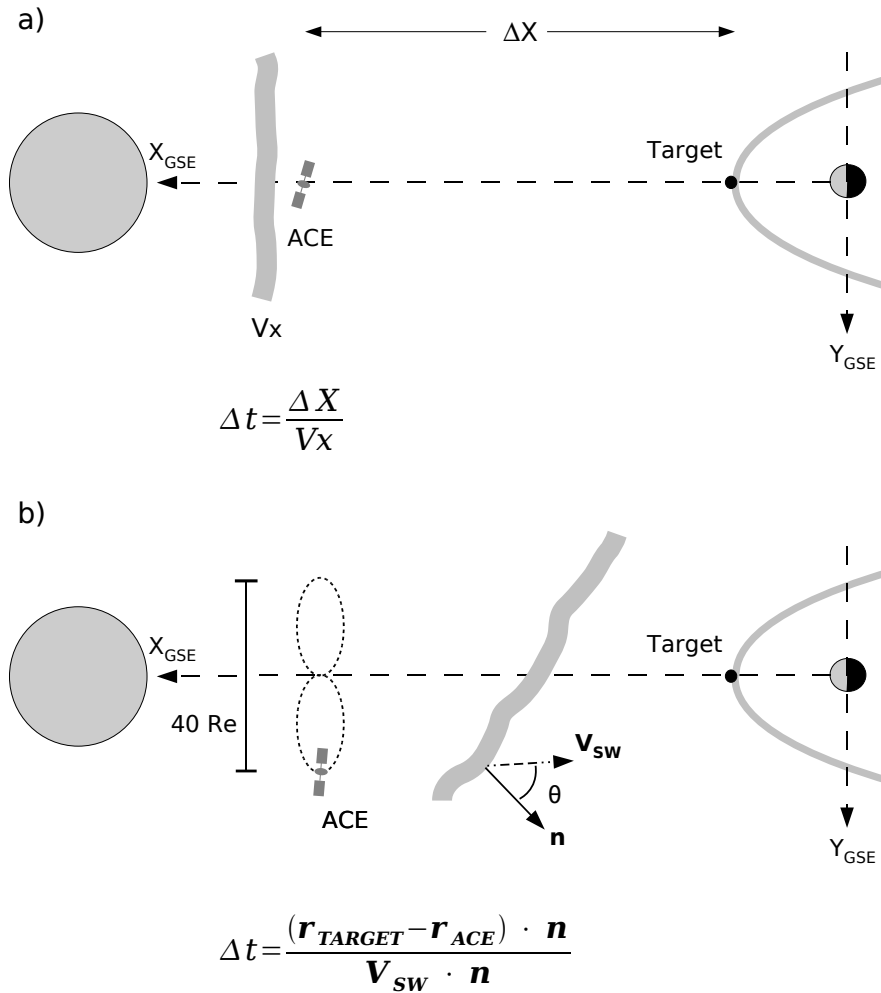


**Fig. 1.** Illustration of the two principal methods to calculate the solar wind propagation delay. **(a)** Flat delay: A planar structure is assumed to propagate with a constant velocity along the Sun-Earth line. Both the solar wind monitor (ACE) and the target (typically the Earth’s upstream magnetopause) are assumed to lie on the Sun-Earth line. **(b)** The real position of the solar wind monitor as well as the orientation of the IMF phase front, represented by its boundary normal  $\mathbf{n}$ , and the actual solar wind velocity vector,  $\mathbf{v}_{sw}$  are taken into account.  $\theta$  is the angle between the phase front normal and the solar wind velocity (in Weimer et al., 2003, the angle  $\theta$  is measured between the normal and the Sun-Earth line).

### 3.2.1 Discontinuity orientation from cross product

The cross product method can be used to get the orientation of a tangential discontinuity (TD – see e.g. Colburn and Sonett, 1966; Smith, 1973), i.e. a discontinuity where there is no net plasma flow across the discontinuity ( $\langle \mathbf{V} \rangle \cdot \mathbf{n} = 0$ ), and where the average magnetic field is tangential to the discontinuity ( $\langle \mathbf{B} \rangle \cdot \mathbf{n} = 0$ ). If these conditions are satisfied, or nearly satisfied, an estimate of the boundary normal is given by:

$$\mathbf{n}_{cross} = \frac{\langle \mathbf{B}_1 \rangle \times \langle \mathbf{B}_2 \rangle}{|\langle \mathbf{B}_1 \rangle \times \langle \mathbf{B}_2 \rangle|} \quad (3)$$

where  $\langle \mathbf{B}_1 \rangle$  and  $\langle \mathbf{B}_2 \rangle$  are the average magnetic field upstream respectively downstream of the discontinuity.

In our study, we have calculated the downstream average  $\langle \mathbf{B}_1 \rangle$  from 10 magnetic field samples ending approximately 3.5 min before the center of the discontinuity. Likewise, the upstream average  $\langle \mathbf{B}_2 \rangle$  is calculated from 10 samples starting approximately 3.5 min after. These time intervals are indicated in the example shown in Fig. 2.

### 3.2.2 Minimum variance of the magnetic field – MVAB

Minimum variance of the magnetic field (MVAB – see e.g. Sonnerup and Cahill, 1967; Sonnerup and Scheible, 1998, and references therein) is perhaps the most frequently used method to obtain the orientation of a discontinuity. MVAB is based on a one-dimensional model of a current sheet. From

the magnetic field vector measurements during the transversal of a discontinuity, one tries to find the apriori unknown direction in which the magnetic field has no variance. In practice, however, this ideal case does not exist, and one seeks to find the direction with minimum variance of the magnetic field. Mathematically, this is achieved by first constructing a magnetic covariance matrix,  $\mathbf{M}_{v\mu}$ , from the measurements, and thereafter finding the eigenvectors and eigenvalues of this matrix. In the present work, we have used a covariance matrix of the form

$$\mathbf{M}_{v\mu} = \langle B_\mu B_\nu \rangle - \langle B_\mu \rangle \langle B_\nu \rangle \quad (4)$$

where  $\langle \dots \rangle$  denotes averaging over a number of measurements. This corresponds to the standard covariance matrix introduced in Sonnerup and Cahill (1967). Other types of covariance matrices are also conceivable. For example, Siscoe et al. (1968) used a simplified covariance matrix of the form

$$\mathbf{M}_{v\mu} = \langle B_\mu B_\nu \rangle \quad (5)$$

for the study of discontinuities in the IMF observed by the Mariner 4 spacecraft. A similar approach was used by Snekvik et al. (2007) to establish the orientation of the tail current sheet. Weimer et al. (2003) initially used a covariance matrix of the form

$$\mathbf{M}_{v\mu} = \langle B_\mu B_\nu \rangle - N \langle B_\mu \rangle \langle B_\nu \rangle \quad (6)$$

where  $N$  is the number of samples used to form the averages. As pointed out in a later correction (Weimer, 2004), this matrix is dominated by the mean magnetic field, and results in negative eigenvalues. The eigenvector corresponding to the smallest, non-negative eigenvalue is nearly orthogonal (but not completely – see discussions in Bargatze et al., 2005, and Haaland et al., 2006) to the mean magnetic field, and thus similar to the cross product method described above. The variance matrix used by Siscoe et al. (1968) and Snekvik et al. (2007) has a similar property.

Weimer et al. (2003) provided a recipe-like procedure for establishing the phase front orientation; first, a short time interval of approximately 8 min was used to construct a covariance matrix. Thereafter, an eigenanalysis was performed on this matrix. If the resulting eigenvalue ratio was poor (i.e.  $\lambda_{\text{int}}/\lambda_{\text{min}} \leq 10$ ), the calculation was discarded and a longer time interval of approximately 28 min was tried. For the long time interval, Weimer et al. (2003) also reduced the eigenvalue criteria, so that a ratio  $\lambda_{\text{int}}/\lambda_{\text{min}} \geq 2$  was accepted. If both time intervals failed, the previous valid normal was used for the delay calculation.

However, since we use a different covariance matrix, we cannot directly adapt the criteria from Weimer et al. (2003). In our calculations we have therefore used a fix 7-min interval centered around the magnetic field rotation to establish the phase front normal. This time interval is marked “A” in Fig. 2. The choice of 7 min seems arbitrary, but was found to

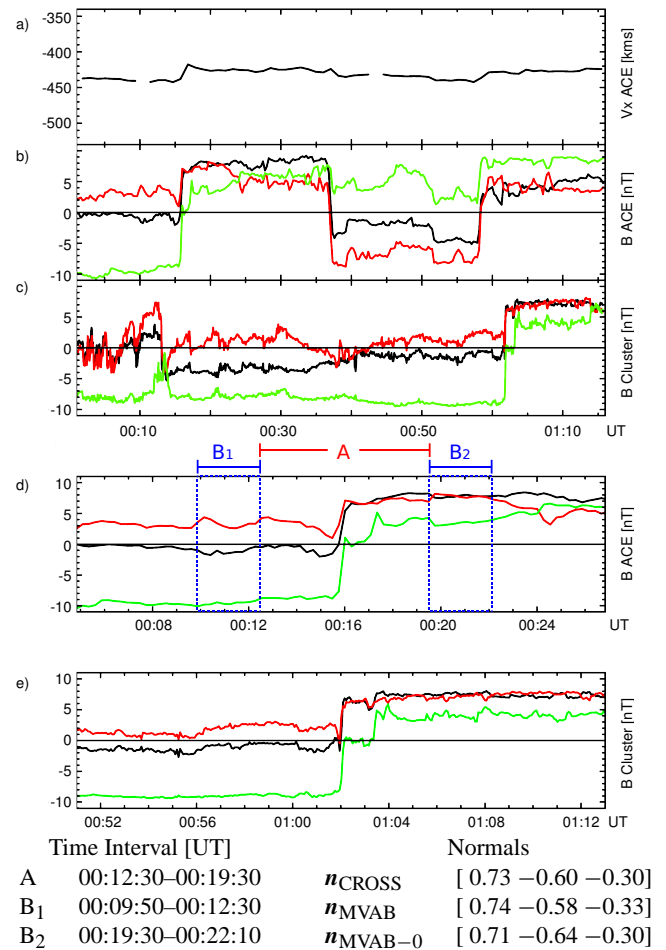


**Fig. 2.** Example of an IMF discontinuity observed by both ACE and Cluster on 30 March 2003. The panels show: (a) the X component of the solar wind speed measured by ACE. (b) magnetic field at ACE, (c) magnetic field at Cluster. (d, e) Same as panels (b) and (c), but zoomed in and centered around the main magnetic field rotation. In panel (d), the marked interval A is the time segment used to calculate the IMF orientation as described in Sects. 3.2.2 and 3.2.3. Similarly, B<sub>1</sub>, B<sub>2</sub> are the corresponding upstream and downstream time intervals used for the cross product calculation – see Sect. 3.2.1. Black, red and green line colors indicate the X, Y, respectively Z<sub>GSE</sub> components of the magnetic fields. The bottom part of the figure shows the exact time intervals used and the normals obtained for this particular case.

be a good compromise which ensures sufficient data points within and on both sides of the discontinuity. With 16-s time resolution in the ACE magnetic field observations, this interval contains 28–30 samples.

### 3.2.3 Constrained minimum variance – MVAB-0

If one has apriori knowledge about the nature of a discontinuity, it may be desirable to impose constraints to the minimum variance analysis. For example, an ideal TD has zero

magnetic field along the normal. One can then constrain perform the analysis so that the predicted normal,  $\mathbf{n}$ , is guaranteed to be perpendicular to the direction of the average magnetic field  $\mathbf{b} = \langle \mathbf{B} \rangle / |\langle \mathbf{B} \rangle|$ . Such a constraint can easily be imposed to the variance analysis by replacing the above covariance matrix,  $\mathbf{M}_{v\mu}$ , by the projection  $\mathbf{Q}' = P_{ik} M_{v\mu} P_{nj}$ , where the projection matrix is given by

$$P_{ij} = \delta_{ij} - b_i b_j \quad (7)$$

where  $\delta_{ij}$  is the delta operator ( $\delta_{ij}=1$  for  $i=j$ , 0 otherwise). The eigenvectors of  $\mathbf{Q}'$  now have a different meaning; since we introduce a known quantity (the vector  $\mathbf{b}$ ), the lowest eigenvalue will be zero, whereas its eigenvector,  $\mathbf{X}_3 = \mathbf{b}$ . The eigenvector  $\mathbf{X}_2$ , corresponding to the lowest, non-zero eigenvalue will now be the normal predictor, and the third eigenvector completes the right handed, orthogonal system.

An alternative procedure to obtain a discontinuity normal orthogonal to the mean magnetic field is given by Bargatze et al. (2005). Their method uses a variance matrix based on  $\mathbf{B}_\perp(t) = \mathbf{B}(t) - \mathbf{B}_\parallel$ , where  $\mathbf{B}_\parallel$  is the magnetic field parallel to the average magnetic field of the 8 or 28 min time interval mentioned in Weimer et al. (2003).

Experience has shown that constrained variance analysis, often referred to as MVAB-0, provides more stable results, also for discontinuities of Alfvénic nature (Sonnerup et al., 2006).

In a survey, Knetter et al. (2003, 2004) applied multi-spacecraft timing methods to a number of discontinuities observed by Cluster in the solar wind, and concluded that most of the observed discontinuities could be classified as TDs. Also, in a recent publication, Weimer and King (2008), adapted the MVAB-0 method, and performed a thorough check of the method, and basically confirmed its usefulness for propagation delay calculations. Although the abundances of rotational and tangential discontinuities in the solar wind have been debated (Neugebauer et al., 1984; Tsurutani and Ho, 1999; Ridley, 2000; Knetter et al., 2004; Neugebauer, 2006), it seems that the assumption that solar wind discontinuities are TDs is justified for this purpose.

### 3.3 Error sources and quality criteria

The “observed” delay in our study is established through visual inspection of the data, and trying to line up the ACE and Cluster magnetic field measurements as shown in Fig. 2. Since most of our events are manifested as distinct and sharp rotations in the magnetic field, we estimate the determination of the observed propagation time to be accurate to within  $\pm 1$  min or less. With only one solar wind monitor available, we cannot say anything about the planarity of the discontinuities, so in the following, we assume that the observed discontinuities are planar.

For the model calculations, the most critical parameter is the orientation of the discontinuity. For MVAB based methods, analytical expressions for the errors in the form of er-

ror ellipses around the normal exist (e.g. Lepping and Behannon, 1980; Khrabrov and Sonnerup, 1998; Sonnerup and Scheible, 1998). A similar approach can in theory also be implemented for the cross product method. However, error estimates of this character are purely statistical and mainly depends on the number of samples used to establish the normal. Errors due to e.g. breakdown of the underlying model assumptions are not taken into account by such error estimates. We have therefore not performed any detailed error analysis of this sort in our study. However, we are able to formulate a set of quality criteria which can be used to determine whether a particular method makes sense for a specific event.

For the MVAB based results, the ratio between the intermediate and minimum eigenvalue provides a rough quality control of the result. As a rule of thumb, an eigenvalue ratio,  $\lambda_{\text{int}}/\lambda_{\text{min}} \geq 10$  has often been used as a criteria for a valid normal determination, although this is rarely achieved without fine tuning of the time interval used for analysis. In our data set, and using the variance matrix as described in Sect. 3.2.2, less than 20% of the discontinuities had an eigenvalue ratio  $\lambda_{\text{int}}/\lambda_{\text{min}} \geq 10$ . We have therefore required an minimum eigenvalue ratio of  $\lambda_{\text{int}}/\lambda_{\text{min}} \geq 3$ .

It should be emphasized, however, that a high eigenvalue ratio in itself is no guarantee for a correct normal estimation. Normals obtained from minimum variance and normals obtained from multi spacecraft methods can in some cases be widely different, despite high eigenvalue ratios (Knetter et al., 2004; Haaland et al., 2004; Sonnerup et al., 2008). Also, the eigenvalue ratio only describes the statistical uncertainty in the eigenvector determination. As with some of the error estimates, the eigenvalue ratio does not account for breakdown of the model assumptions.

For the constrained minimum variance, the lowest eigenvalue is per definition zero, and the only sensible eigenvalue ratio is  $\lambda_{\text{max}}/\lambda_{\text{int}}$ . Since the maximum variance direction is typically well defined for a 1-D or 2-D structure, this ratio is usually much higher (typically a factor 10 or more) than the above  $\lambda_{\text{int}}/\lambda_{\text{min}}$  ratio. In our data set, the majority of the events had eigenvalue ratios  $\lambda_{\text{max}}/\lambda_{\text{int}} \geq 60$ , so we decided to require a minimum eigenvalue ratio of 10 for this quality parameter.

For the cross product methods, we checked the angular difference,  $\phi$ , between the upstream and downstream magnetic field (i.e. the field rotation). Values around  $0^\circ$  or  $180^\circ$  indicate parallel or antiparallel fields, and thus a poorly determined cross product. In our study, we have required that the orientation of  $\langle \mathbf{B}_1 \rangle$  and  $\langle \mathbf{B}_2 \rangle$  differs at least  $30^\circ$ . This criteria is similar to the definition used by Lepping and Behannon (1986).

In addition to the above, we also required that the calculated normal should be within  $\theta = \pm 70^\circ$  of the solar wind velocity direction (see Fig. 1). A similar criteria was used by Weimer et al. (2003).

## 4 Results

During the period February 2001 to April 2007, we found a total of 198 clear discontinuities that could be unambiguously identified at both ACE and Cluster. For each event, we first plotted the ACE magnetic field, solar wind velocity, the corresponding Cluster magnetic field, and recorded the position of ACE relative to Cluster. Thereafter, we calculated the time delays as well as the quality parameters for the four methods.

### 4.1 Example

Figure 2 shows an example of a single event. On 30 March 2003, the ACE spacecraft observed a series of distinct magnetic field rotations. At about 00:16 UT the IMF direction turns from a predominantly southward direction to a more Parker spiral like orientation. Prior to the rotation, the IMF is fairly stable with a solar wind velocity of about  $435 \text{ km s}^{-1}$ . The same magnetic field rotation is seen at Cluster about 01:02 UT, i.e. around 46 min later. Cluster was located around  $14 R_E$  upstream, and the average separation in Y-direction between Cluster and ACE was only about  $13 R_E$  in this case.

The calculated normals from the three methods MVAB, MVAB-0 and cross product are very similar, and have a significant  $X_{GSE}$  component. All methods, including the flat delay method, were able to predict the propagation time from ACE to Cluster to within 4 min for this event. The poorest performance was the flat delay, which predicted a propagation time of 51 min in this case, whereas the best prediction was obtained with the MVAB-0 method, which predicted the arrival time to within one minute.

Although our selection of events may be biased, this example is by no means atypical; due to the high velocity of the solar wind compared to the available time resolution of the data, most events are manifested as sharp transitions in the IMF which allows for a fairly precise determination of the real time delay.

### 4.2 Statistical deviations between observed and predicted arrival times

In the following, we discuss the deviations between predicted and observed arrival times of the discontinuities in a statistical sense. For all 198 events, we calculate a timing error for each method, defined as  $\Delta t = t_{\text{model}} - t_{\text{observed}}$ , and try to find correlations with quality parameters, IMF orientation and spacecraft separation distances.

Figure 3 shows the relative distribution of the timing errors for the four models. To show the effect of the quality parameters discussed above, we also show the distributions from a filtered data set (lower panels). Depending on method, a number of events fall below our quality criteria.

We did not apply any filters to the flat delay, so this is equal in the top and bottom panels. As seen from the distribution, the predicted arrival time of the the discontinuities at Cluster are within 10 min in most cases, and a substantial number of events even arrive at Cluster within  $\pm 5$  min of the time predicted by the flat delay method.

For the cross product method, the majority of discontinuities arrive at Cluster within  $\pm 5$  min of the predicted time, regardless of whether we consider the filtered or unfiltered set. For the filtered data set, an arrival accuracy of  $\pm 2$  min is obtained for almost 30% of the cases.

In our data set, the MVAB method perform worse than the simple delay of cross product method. Still, most of the discontinuities arrive within  $\pm 10$  min of the predicted time. Removing events which do not satisfy the quality criteria, results improves the relative accuracy, and more than 50% of the cases arrives within  $\pm 5$  min.

For the constrained minimum variance method, 65% of the cases have a timing accuracy of  $\pm 5$  min or better, and more than 30% have an arrival accuracy of  $\pm 2$  min or less. For the filtered dataset, the results are even better – more than 35% of the events arrive within the  $\pm 2$  min of the predicted time, and 82% arrive within  $\pm 5$  min of the predicted time.

In summary, the constrained minimum variance analysis gives the best performance, but the cross product also provides a fairly accurate estimate of the arrival time in most cases.

#### 4.2.1 Spacecraft separation effect

One of the motivations for Weimer et al. (2003) was to devise a method that takes into account the lateral displacement, i.e. primarily  $Y_{GSE}$  separation between the monitor and the target. In Fig. 4 we have plotted the timing errors of each method as function of the spacecraft separation distance in y-direction:  $\Delta Y = \text{ACE } Y_{GSE} - \text{Cluster } Y_{GSE}$ . The ACE orbit alone takes the spacecraft out to approximately  $40 R_E$  away from the Sun-Earth line, whereas for the seasons we have studied, Cluster is maximum  $8 R_E$  away from the Sun-Earth line. Both Weimer et al. (2003) and Horbury et al. (2001a) additionally used the Wind spacecraft, and partly the Interplanetary Monitoring Platform (IMP-8) and the Geotail spacecraft, so their data set and discussion had significantly larger lateral separations.

As shown in Fig. 4, the best prediction of the arrival time, i.e. a  $\Delta t \simeq 0$  is typically obtained when both ACE and Cluster are located roughly on the same  $Y_{GSE}$  position. In particular, the flat delay method shows large spreads in the results when the lateral separation is more than  $40 R_E$ . For large positive separations  $\Delta t$  tends to be negative, (i.e. the calculated time delay is smaller than the observed), whereas the opposite is the case for large negative distances. This is as expected for a typical Parker spiral like orientation of the IMF.

From Fig. 4, it also appears that some of the events with large timing errors are common to several methods (e.g. the

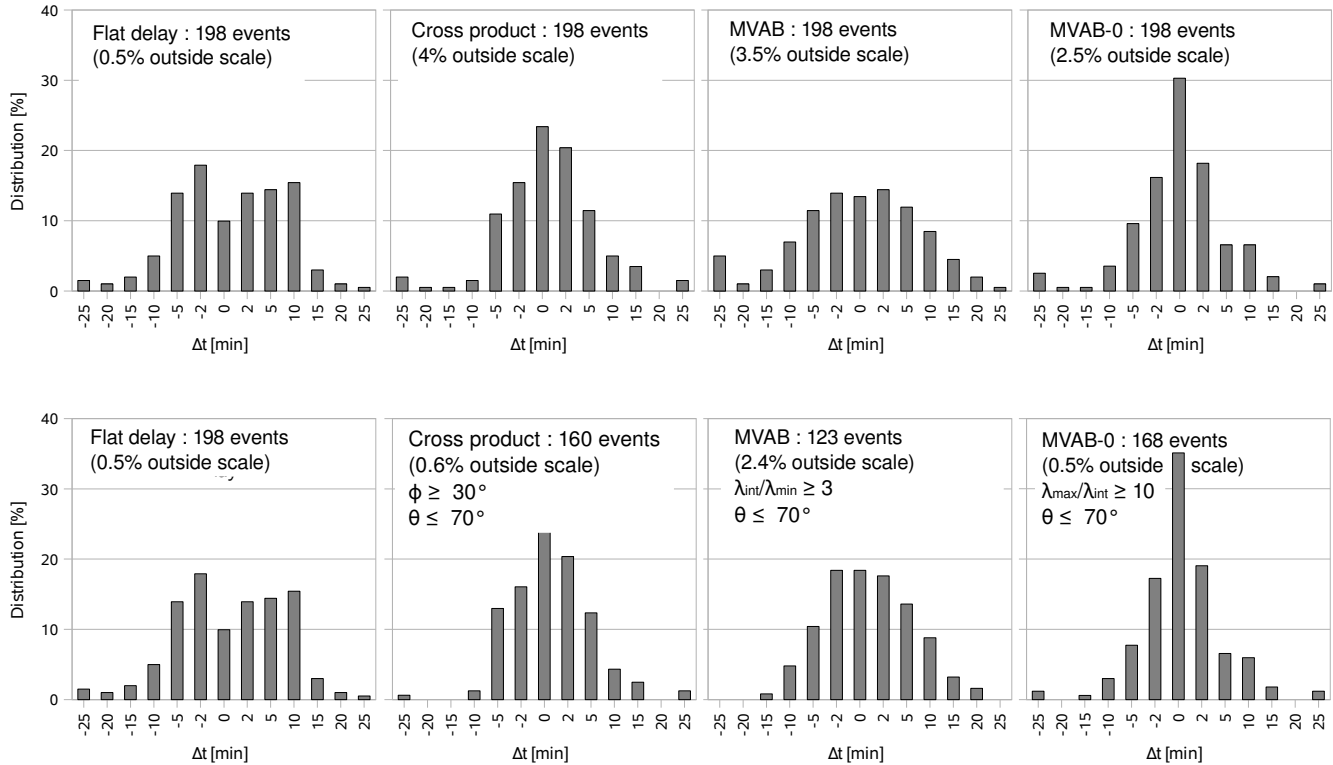


**Fig. 3.** Distributions of timing errors for each of the four tested methods. Top panels: results from the full data set, containing 198 events. Bottom panels: results from the filtered data set, i.e. events not satisfying the quality criteria described in Sect. 3.3 have been removed. The horizontal axes indicate the time differences  $\Delta t = t_{\text{model}} - t_{\text{observed}}$  for each method, and the vertical axes, common to all panels in that row, show the relative distribution within that  $\Delta t$  range. Note that the horizontal axes are non-linear; the center bin (marked 0) means  $\pm 0$ –2 min, the next bin  $\pm 2$ –5 min, thereafter  $\pm 5$ –10 min etc. Also, the horizontal scale is limited to  $\pm 25$  min, but a few events from each method had larger discrepancies. These are indicated in each panel as (% outside scale).

two data points with  $\Delta t \approx 22$  min seen in the panels for cross product and MVAB-0 results). This could either mean that both methods fail to give correct orientations, or that other effects such as non-planarity or scale sizes of the discontinuity also affect the results.

In this sense, the results of Tsurutani et al. (2005) are somewhat exceptional. Although their  $\Delta Y$  were in the range  $28$ – $39 R_E$ , the observed arrival times were less than a minute from the flat delay predictions.

#### 4.2.2 Influence of IMF orientation

A critical factor for time shift estimations relying on the MVAB, MVAB-0 and cross product method is the discontinuity orientation. The top panel of Fig. 5 shows the timing error as function of the  $\theta$  angle, which is the angle between the discontinuity normal and the solar wind velocity (also illustrated in the lower panel of Fig. 1). A large angle indicate a slant discontinuity orientation, whereas the typical Parker spiral like orientation would give a  $\theta$  angle around  $45^\circ$ . For all three methods, a deterioration is seen for large angles.

To check the reliability of our normal estimations, we checked the correlation between the quality criteria described in Sect. 3.3 and the timing errors:

For the minimum variance methods, we checked the dependence on the eigenvalue ratios  $\lambda_{\text{int}}/\lambda_{\text{min}}$  for MVAB and  $\lambda_{\text{max}}/\lambda_{\text{int}}$  for MVAB-0. The bottom panel of Fig. 5 shows the timing errors as function of these two ratios. As explained in Sect. 3.3, the eigenvalue ratios for MVAB and MVAB-0 are not directly comparable; the MVAB-0 eigenvalue ratio  $\lambda_{\text{max}}/\lambda_{\text{int}}$  is typically a factor 10 higher than the ratio  $\lambda_{\text{int}}/\lambda_{\text{min}}$  from MVAB. We have therefore used two horizontal axes and color coded the results in the lower panel of Fig. 5. The plot shows a clear dependence; low eigenvalue ratios, which typically indicate poorly determined normals, gives a larger difference between the predicted and observed time delays. From the plot, one would conclude that an eigenvalue ratio  $\lambda_{\text{int}}/\lambda_{\text{min}} \geq 10$  for MVAB and  $\lambda_{\text{max}}/\lambda_{\text{int}} \geq 100$  would be desirable for optimal results. Unfortunately, very few of our events have such large eigenvalue ratios.

For the cross product method, we also checked the correlation between the timing error and the  $\phi$  angle (i.e. the field rotation between the upstream and downstream B-field).

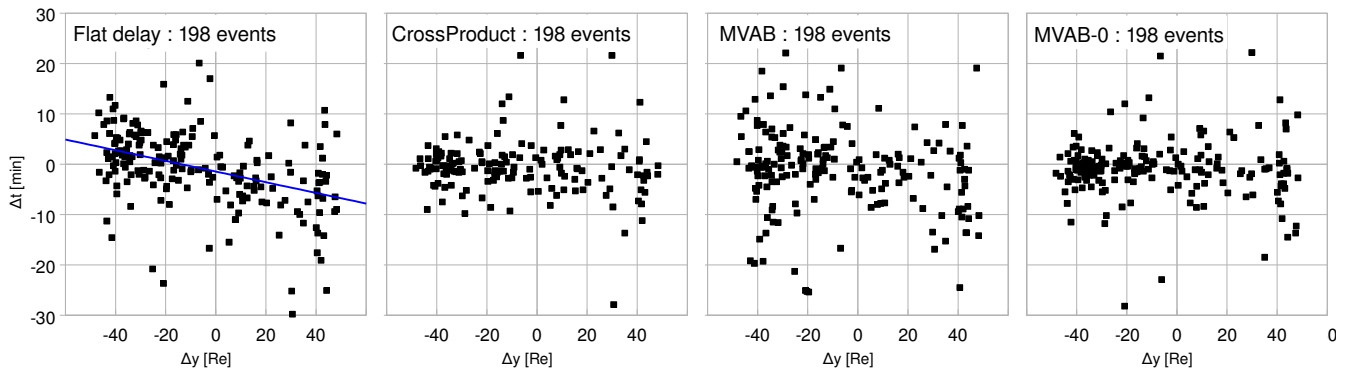


**Fig. 4.** Arrival time errors as function of the separation between ACE and Cluster in the  $Y_{GSE}$  direction. The vertical axis, common to all panels, shows the time differences  $\Delta t = t_{\text{model}} - t_{\text{observed}}$ , and the horizontal axes show the  $Y_{GSE}$  separation between the ACE and Cluster spacecraft,  $\Delta Y = Y_{ACE} - Y_{CLUSTER}$  for each method. Since the Cluster orbit in our data set has only has a maximum  $Y_{GSE}$  position of  $\pm 8 R_E$ , this plot can roughly be interpreted as the dependence of the ACE  $Y_{GSE}$  position. The blue line in the panel for flat delay indicates the linear trend calculated from the data points.

However, we could not find any correlation here, and only a few events had field rotations of less than  $30^\circ$ .

#### 4.3 Cases with no discontinuities

So far, we have focused on time intervals which contain a distinct discontinuity, observed as a clear rotation in the magnetic field. Despite the frequent occurrence of discontinuities in the solar wind, a more typical situation is a fairly stable IMF, often aligned along the Parker spiral. As pointed out above, the knowledge of the IMF conditions at the Earth's magnetopause is also important for such cases, and is one of the key aspects addressed by the methods of (Weimer et al., 2003; Weimer and King, 2008).

To test the ability of the various methods to predict propagation times under such conditions, we repeated the calculations from Sect. 3, but now using a time interval 7 min later. This interval typically does not contain any distinct discontinuity (although it may). In most of our cases, the change in the solar wind velocity between the upstream and downstream of the discontinuity was small, and the changes in separation between ACE and Cluster within 7 min are also negligible. The flat delay results are therefore similar, and the true propagation,  $t_{\text{obs}}$  from the data set with distinct discontinuities can therefore still be used as a reference for benchmarking. An alternative method would have been to pick out random time intervals for this test, and tried to establish the true time delay from e.g. cross correlation, but we did not try this out.

In this displaced time interval, one would expect that the methods relying on the orientation would fail or deteriorate since there is no clear rotation of the field any more, and the assumptions implied by both minimum variance (a quasi 1-D current sheet) and the cross product method (a tangential discontinuity) would fail.

This is also exactly what happens to our data set. Our quality criteria for the cross product ( $\phi \geq 30^\circ$  – see Sect. 3.3) fails for more than half of the events, and a reliable cross product normal can only be obtained for 63 of our 198 events. Of these, arrival times within  $\pm 5$  min are obtained for 41 events, compared to 84 events for a simple flat delay. The MVAB based propagation times also performs worse for this data set. The eigenvalue ratios are often very low which indicate poorly determined normals.

The performance of the MVAB-0 method is also reduced, but this methods still gives the the overall best estimate of the propagation delay. Approximately 71% of the calculated propagation times are within 10 min of the observed time, but a few of the predicted times are very much longer than the observed. However, the flat delay method, not relying on the IMF orientation performs equally well as for the data set with discontinuities. With almost 70% of the cases arriving within 10 min of the observed times, it performs only marginally worse than the MVAB-0 results.

## 5 Summary and conclusions

We have done a statistical study of the propagation times of IMF discontinuities between the ACE solar wind monitor orbiting the L1 libration point and the Cluster quartet of spacecraft close to the Earth's bow shock. The two spacecraft are separated between 0 and  $\pm 48 R_E$  in the  $Y_{GSE}$  direction.

For 198 distinct discontinuities, we calculated the time shift as predicted by four different models, and compared this to the observed time delay.

The results can be summarized as follows:

- The most precise determination of the arrival of a discontinuity at a target near the Earth's magnetopause is

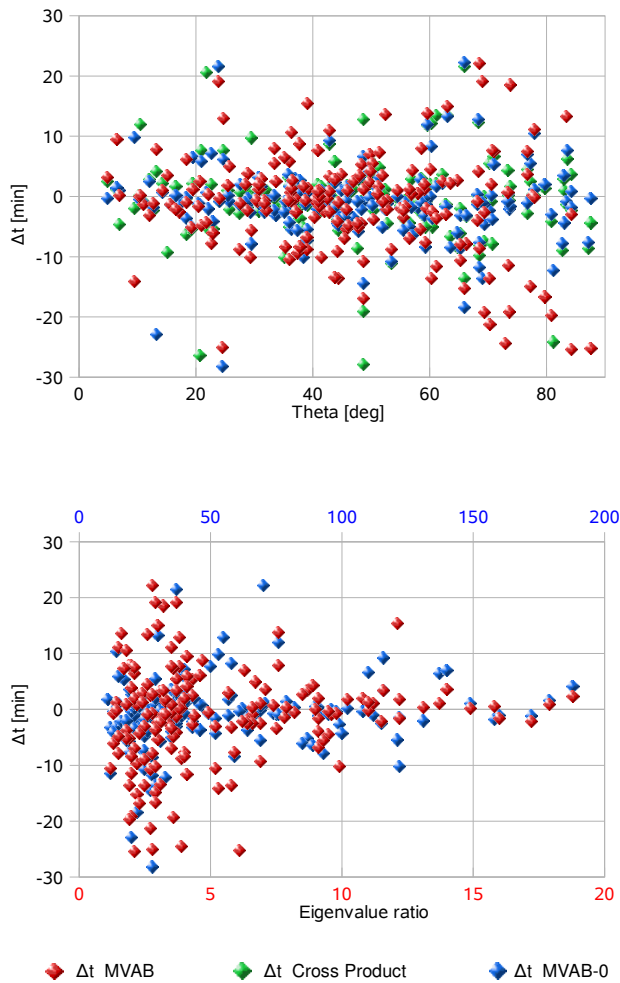


**Fig. 5.** Top panel : Difference between observed and predicted arrival times as function of the angle  $\theta$  (the angle between the discontinuity normal and the solar wind velocity – see also Fig. 1). Bottom panel: Difference between observed and predicted arrival times as function of eigenvalue ratio for the minimum variance based methods. The vertical axes in both panels show the time differences  $\Delta t = t_{\text{model}} - t_{\text{observed}}$ . In the lower panel, red data points, and the lower vertical axis indicate the  $\lambda_{\text{int}}/\lambda_{\text{min}}$  eigenvalue ratio for MVAB, whereas the blue symbols and the upper horizontal axis indicate the corresponding ratio  $\lambda_{\text{max}}/\lambda_{\text{int}}$  for the MVAB-0 method.

achieved if the orientation of the discontinuity is taken into account.

- For the data set discussed here, the best predictions of arrival times of discontinuities at the Earth’s magnetopause are obtained if the orientation of the discontinuity is obtained from constrained minimum variance analysis of the magnetic field as suggested by Weimer et al. (2003).

- The arrival predictions using flat delay deteriorates, but not significantly, if the solar wind monitor is far away from the Sun-Earth line. This argument may not be very important in cases where the ACE spacecraft with its maximum  $\pm 40 R_E$  displacement from the Sun-Earth line, but should be kept in mind if the IMF observations are taken other solar wind monitors with larger lateral displacements are used.
- In our data set, the MVAB-0 based method works fairly well even for cases without a distinct discontinuity, and provide more reliable predictions than the other methods.
- For cases without any clear discontinuities, the prediction of the arrival times becomes less precise for both the cross product method and the minimum variance method.
- Despite the fact that propagation delay calculations based on the constrained minimum variance analysis performed better than the other methods, there are some drawbacks with the method. Compared to a simple flat delay calculation, which may be “good enough”, it is computational much more complex.

*Acknowledgements.* This project was initiated as a student project at the COSPAR Regional Workshop for Space Physicists from Central and Eastern Europe, held in Sinaia, Romania, 4–16 June 2007. B. Mailyan thanks the Centre national de la recherche scientifique (CNRS), France for financial support to attend and present these results at the STAMMS-2 conference, held in Orleans, France in September 2007. Parts of the data analysis were done with the QSAS science analysis system provided by the United Kingdom Cluster Science Centre (Imperial College London and Queen Mary, University of London) supported by the United Kingdom Science and Technology Facilities Council (STFC). We also thank the International Space Science Institute, Bern, Switzerland for providing computer resources and infrastructure for data exchange. ACE data were obtained from the Coordinated Data Analysis Web (CDAWeb – see <http://cdaweb.gsfc.nasa.gov/about.html>).

Topical Editor R. Nakamura thanks D. Weimer and another anonymous referee for their help in evaluating this paper.

## References

- Balogh, A., Carr, C. M., Acuña, M. H., Dunlop, M. W., Beek, T. J., Brown, P., Fornacq̃n, K. H., Georgescu, E., Glassmeier, K. H., Harris, J., Musmann, G., Oddy, T., and Schwingenschuh, K.: The Cluster Magnetic Field Investigation: Overview of in-flight performance and initial results, *Ann. Geophys.*, 19, 1207–1217, 2001, <http://www.ann-geophys.net/19/1207/2001/>.
- Bargatze, L. F., McPherron, R. L., Minamora, J., and Weimer, D.: A new interpretation of Weimer et al.’s solar wind propagation delay technique, *J. Geophys. Res.*, 110, 7105, doi: 10.1029/2004JA010902, 2005.

- Colburn, D. S. and Sonett, C. P.: Discontinuities in the Solar Wind, *Space Sci. Rev.*, 5, 439–506, doi:10.1007/BF00240575, 1966.
- Dungey, J. R.: Interplanetary magnetic field and the auroral zones, *Phys. Rev. Lett.*, 6, 47–48, 1961.
- Förster, M., Paschmann, G., Haaland, S. E., Quinn, J. M., Torbert, R. B., Vaith, H., and Kletzing, C. A.: High-latitude plasma convection from Cluster EDI: variances and solar wind correlations, *Ann. Geophys.*, 25, 1691–1707, 2007, <http://www.ann-geophys.net/25/1691/2007/>.
- Gombosi, T. I., Dezeewu, D. L., Groth, C. P. T., and Powell, K. G.: Magnetospheric Configuration for Parker-Spiral IMF Conditions: Results of A 3D AMR MHD Simulation, *Adv. Space Res.*, 26, 139–149, 2000.
- Haaland, S., Sonnerup, B. U. Ö., Dunlop, M. W., Balogh, A., Hasegawa, H., Klecker, B., Paschmann, G., Lavraud, B., Dandouras, I., and Rème, H.: Four-Spacecraft Determination of Magnetopause Orientation, Motion and Thickness: Comparison with Results from Single-Spacecraft Methods, *Ann. Geophys.*, 22, 1347–1365, 2004, <http://www.ann-geophys.net/22/1347/2004/>.
- Haaland, S., Paschmann, G., and Sonnerup, B. U. Ö.: Comment on “A new interpretation of Weimer et al.’s solar wind propagation delay technique” by Bargate et al., *J. Geophys. Res.*, 111, 6102–6106, doi:10.1029/2005JA011376, 2006.
- Haaland, S. E., Paschmann, G., Förster, M., Quinn, J. M., Torbert, R. B., McIlwain, C. E., Vaith, H., Puhl-Quinn, P. A., and Kletzing, C. A.: High-latitude plasma convection from Cluster EDI measurements: method and IMF-dependence, *Ann. Geophys.*, 25, 239–253, 2007, <http://www.ann-geophys.net/25/239/2007/>.
- Horbury, T. S., Burgess, D., Fränz, M., and Owen, C. J.: Prediction of Earth arrival times of interplanetary southward magnetic field turnings, *J. Geophys. Res.*, 106, 30 001–30 009, 2001a.
- Horbury, T. S., Burgess, D., Fränz, M., and Owen, C. J.: Three spacecraft observations of solar wind discontinuities, *Geophys. Res. Lett.*, 28, 677–680, doi:10.1029/2000GL000121, 2001b.
- Hudson, P. D.: Discontinuities in an anisotropic plasma and their identification in the solar wind, *Planet. Space Sci.*, 18, 1611–1622, doi:10.1016/0032-0633(70)90036-X, 1970.
- Khrabrov, A. V. and Sonnerup, B. U. Ö.: Error estimates for minimum variance analysis, *J. Geophys. Res.*, 103, 6641, 1998.
- Knetter, T.: A new perspective of the solar wind micro-structure due to multi-point observations of discontinuities, Ph.D. thesis, University of Cologne, Germany, 2004.
- Knetter, T., Neubauer, F. M., Horbury, T., and Balogh, A.: Discontinuity observations with Cluster, *Adv. Space Res.*, 32, 543–548, doi:10.1016/S0273-1177(03)00335-1, 2003.
- Knetter, T., Neubauer, F. M., Horbury, T., and Balogh, A.: Four-point discontinuity observations using Cluster magnetic field data: A statistical survey, *J. Geophys. Res.*, 109, 6102, doi:10.1029/2003JA010099, 2004.
- Landau, L. D. and Lifshitz, E. M.: *Electrodynamics of continuous media*, vol. 8, Pergamon Press., 1960.
- Lepping, R. P. and Behannon, K. W.: Magnetic field directional discontinuities. I – Minimum variance errors, *J. Geophys. Res.*, 85, 4695–4703, 1980.
- Lepping, R. P. and Behannon, K. W.: Magnetic field directional discontinuities – Characteristics between 0.46 and 1.0 AU, *J. Geophys. Res.*, 91, 8725–8741, 1986.
- Lyons, L. R.: Substorms: Fundamental observational features, distinction from other disturbances, and external triggering, *J. Geophys. Res.*, 101, 13 011–13 026, doi:10.1029/95JA01987, 1996.
- Lyons, L. R., Liu, S., Ruohoniemi, J. M., Solov'yev, S. I., and Samson, J. C.: Observations of dayside convection reduction leading to substorm onset, *J. Geophys. Res. (Space Physics)*, 108, doi:10.1029/2002JA009670, 2003.
- McComas, D. J., Bame, S. J., Barker, P., Feldman, W. C., Phillips, J. L., Riley, P., and Griffee, J. W.: Solar Wind Electron Proton Alpha Monitor (SWEPAM) for the Advanced Composition Explorer, *Space Sci. Rev.*, 86, 563–612, 1998.
- Neugebauer, M.: Comment on the abundances of rotational and tangential discontinuities in the solar wind, *J. Geophys. Res.*, 111, A04103, doi:10.1029/2005JA011497, 2006.
- Neugebauer, M., Clay, D. R., Goldstein, B. E., Tsurutani, B. T., and Zwickl, R. D.: A reexamination of rotational and tangential discontinuities in the solar wind, *J. Geophys. Res.*, 89, 5395–5408, 1984.
- Ogino, T., Walker, R. J., and Ashour-Abdalla, M.: A global magnetohydrodynamic simulation of the response of the magnetosphere to a northward turning of the interplanetary magnetic field, *J. Geophys. Res.*, 99, 11 027–11 042, doi:10.1029/93JA03313, 1994.
- Papitashvili, V. O. and Rich, F. J.: High-latitude ionospheric convection models derived from Defense Meteorological Satellite Program ion drift observations and parameterized by the interplanetary magnetic field strength and direction, *J. Geophys. Res.*, 107, 17–1, doi:10.1029/2001JA000264, 2002.
- Rème, H., Aoustin, C., Bosqued, J. M., Dandouras, I., Lavraud, B., Sauvaud, J. A., Barthe, A., Bouyssou, J., Camus, T., Coeur-Joly, O., Cros, A., Cuvilo, J., Ducay, F., Garbarowitz, Y., Medale, J. L., Penou, E., Perrier, H., Romefort, D., Rouzaud, J., Vallat, C., Alcaydé, D., Jacquey, C., Mazelle, C., D’Uston, C., Möbius, E., Kistler, L. M., Crocker, K., Granoff, M., Moukikis, C., Popecki, M., Vosbury, M., Klecker, B., Hovestadt, D., Kucharek, H., Kuenneth, E., Paschmann, G., Scholer, M., Scokpe, N., Seidenschwang, E., Carlson, C. W., Curtis, D. W., Ingraham, C., Lin, R. P., McFadden, J. P., Parks, G. K., Phan, T., Formisano, V., Amata, E., Bavassano-Cattaneo, M. B., Baldetti, P., Bruno, R., Chionchio, G., di Lellis, A., Marcucci, M. F., Pallocchia, G., Korth, A., Daly, P. W., Graeve, B., Rosenbauer, H., Vasyliunas, V., McCarthy, M., Wilber, M., Eliasson, L., Lundin, R., Olsen, S., Shelley, E. G., Fuselier, S., Ghielmetti, A. G., Lennartsson, W., Escoubet, C. P., Balsiger, H., Friedel, R., Cao, J.-B., Kovrazhkin, R. A., Papamastorakis, I., Pellat, R., Scudder, J., and Sonnerup, B.: First multispacecraft ion measurements in and near the Earth’s magnetosphere with the identical Cluster ion spectrometry (CIS) experiment, *Ann. Geophys.*, 19, 1303–1354, 2001, <http://www.ann-geophys.net/19/1303/2001/>.
- Ridley, A. J.: Estimations of the uncertainty in timing the relationship between magnetospheric and solar wind processes, *J. Atmos. Solar-Terr. Phys.*, 62, 757–771, 2000.
- Ruohoniemi, J. M. and Greenwald, R. A.: Dependencies of high-latitude plasma convection: Consideration of interplanetary magnetic field, seasonal, and universal time factors in statistical patterns, *J. Geophys. Res.*, 110, A09204, doi:10.1029/2004JA010815, 2005.
- Sergeev, V. A., Dmitrieva, N. P., and Barkova, E. S.: Triggering of

- substorm expansion by the IMF directional discontinuities: Time delay analysis, *Planet. Space Sci.*, 34, 1109–1118, doi:10.1016/0032-0633(86)90023-1, 1986.
- Siscoe, G. L., Davis, Jr., L., Coleman Jr., P. J., Smith, E. J., and Jones, D. E.: Power Spectra and Discontinuities of the Interplanetary Magnetic Field: Mariner 4, *J. Geophys. Res.*, 73, 61–79, 1968.
- Smith, C. W., L'Heureux, J., Ness, N. F., Acuña, M. H., Burlaga, L. F., and Scheifele, J.: The ACE Magnetic Fields Experiment, *Space Sci. Rev.*, 86, 613–632, 1998.
- Smith, E. J.: Identification of interplanetary tangential and rotational discontinuities., *J. Geophys. Res.*, 78, 2054–2063, 1973.
- Snekvik, K., Haaland, S., Østgaard, N., Hasegawa, H., Nakamura, R., Takada, T., Juusola, L., Amm, O., Pitout, F., Rème, H., Klecker, B., and Lucek, E. A.: Cluster observations of a field aligned current at the dawn flank of a bursty bulk flow, *Ann. Geophys.*, 25, 1405–1415, 2007, <http://www.ann-geophys.net/25/1405/2007/>.
- Sonnerup, B. U. Ö. and Cahill, L.: Magnetopause structure and altitude from Explorer-12 observations, *J. Geophys. Res.*, 72, 171–183, 1967.
- Sonnerup, B. U. Ö. and Scheible, M.: Minimum and Maximum Variance Analysis, in: *Analysis Methods for Multi-Spacecraft Data*, edited by: Paschmann, G. and Daly, P. W., ISSI SR-001, p. 1850, ESA Publications Division, 1998.
- Sonnerup, B. U. Ö., Haaland, S., Paschmann, G., Dunlop, M. W., Rème, H., and Balogh, A.: Orientation and motion of a plasma discontinuity from single-spacecraft measurements: Generic residue analysis of Cluster data, *J. Geophys. Res.*, 111, 5203–5223, doi:10.1029/2005JA011538, 2006.
- Sonnerup, B. U. Ö., Haaland, S., and Paschmann, G.: Discontinuity Orientation, Motion and Thickness, in: *Multi-spacecraft Analysis Methods Revisited*, edited by Paschmann, G. and Daly, P. W., ISSI SR-005, pp. 1–10, ESA Publications Division, 2008.
- Tsurutani, B. T. and Ho, C. M.: A review of discontinuities and Alfvén waves in interplanetary space: Ulysses results., *Rev. Geophys.*, 37, 517–541, 1999.
- Tsurutani, B. T. and Smith, E. J.: Interplanetary discontinuities - Temporal variations and the radial gradient from 1 to 8.5 AU, *J. Geophys. Res.*, 84, 2773–2787, 1979.
- Tsurutani, B. T., Guarnieri, F. L., Lakhina, G. S., and Hada, T.: Rapid evolution of magnetic decreases (MDs) and discontinuities in the solar wind: ACE and Cluster, *Geophys. Res. Lett.*, 32, 10 103, doi:10.1029/2004GL022151, 2005.
- Tsyganenko, N. A.: A model of the near magnetosphere with a dawn-dusk asymmetry 1. Mathematical structure, *J. Geophys. Res.*, 107, 12–1, doi:10.1029/2001JA000219, 2002a.
- Tsyganenko, N. A.: A model of the near magnetosphere with a dawn-dusk asymmetry 2. Parameterization and fitting to observations, *J. Geophys. Res.*, 107, 10–1, doi:10.1029/2001JA000220, 2002b.
- Turner, J. M. and Siscoe, G. L.: Orientations of "rotational" and "tangential" discontinuities in the solar wind., *J. Geophys. Res.*, 76, 1816–1822, 1971.
- Volwerk, M.: Multi-Satellite observations of ULF waves, in: *Magnetospheric ULF waves: Synthesis and new directions*, edited by: Takahashi, K., Chi, P. J., Denton, R. E., and Lysak, R. L., pp. 109–135, AGU, Washington, 2006.
- Weimer, D. R.: Correction to "Predicting interplanetary magnetic field (IMF) propagation delay times using the minimum variance technique", *J. Geophys. Res.*, 109, 12 104, doi:10.1029/2004JA010691, 2004.
- Weimer, D. R.: Improved ionospheric electrodynamic models and application to calculating Joule heating rates, *J. Geophys. Res.*, 110, 5306, doi:10.1029/2004JA010884, 2005.
- Weimer, D. R. and King, J. H.: Improved calculations of IMF phase front angles and propagation time delays, *J. Geophys. Res.*, 113, A01105, doi:10.1029/2007JA012452, 2008.
- Weimer, D. R., Ober, D. M., Maynard, N. C., Burke, W. J., Collier, M. R., McComas, D. J., Ness, N. F., and Smith, C. W.: Variable time delays in the propagation of the interplanetary magnetic field, *J. Geophys. Res.*, 107, 29–1, doi:10.1029/2001JA009102, 2002.
- Weimer, D. R., Ober, D. M., Maynard, N. C., Collier, M. R., McComas, D. J., Ness, N. F., Smith, C. W., and Watermann, J.: Predicting interplanetary magnetic field (IMF) propagation delay times using the minimum variance technique, *J. Geophys. Res.*, 108, 16–1, doi:10.1029/2002JA009405, 2003.

## Paper II





# Solar wind propagation delay: Comment on “Minimum variance analysis-based propagation of the solar wind observations: Application to real-time global magnetohydrodynamic simulations” by A. Pulkkinen and L. Raststätter

S. Haaland,<sup>1,2</sup> C. Munteanu,<sup>3</sup> and B. Mailyan<sup>4</sup>

Received 6 November 2009; revised 22 January 2010; accepted 16 February 2010; published 19 June 2010.

**Citation:** Haaland, S., C. Munteanu, and B. Mailyan (2010), Solar wind propagation delay: Comment on “Minimum variance analysis-based propagation of the solar wind observations: Application to real-time global magnetohydrodynamic simulations” by A. Pulkkinen and L. Raststätter, *Space Weather*, 8, S06005, doi:10.1029/2009SW000542.

## 1. Introduction

[1] Many space weather phenomena, like geomagnetic storms, aurora etc., are typically associated with disturbances in the solar wind, in particular directional changes in the interplanetary magnetic field (IMF). A southward directed IMF interacts with the geomagnetic field at the dayside magnetopause and causes enhanced energy and momentum transfer from the solar wind to the magnetosphere. The subsequent entry of this energy into the terrestrial ionosphere can lead to disturbances in radio communication, navigation systems and power grids. The ability to predict such consequences is therefore a central topic for space weather applications.

[2] Since actual measurements of the solar wind and IMF are typically taken at large distances from the Earth, e.g., from the Advanced Composition Explorer (ACE) spacecraft orbiting the L1 libration point some  $1.5 \cdot 10^8$  km upstream of the Earth, any measurements need to be time shifted to be representative for the conditions near the upstream magnetopause where the interaction takes place. The propagation time depends on both solar wind velocity, orientation of the IMF and the location of the solar wind monitor.

[3] A lot of effort has therefore been made to be able to predict the propagation time of solar wind disturbances between a monitor and a target position. One of the most successful methods in terms of prediction accuracy is the phase front model introduced by *Weimer et al.* [2003, hereafter W03] and later benchmarked by, e.g., *Weimer and King* [2008] and *Mailyan et al.* [2008].

[4] W03 noted that variations in the IMF primarily occur within surfaces that can be arbitrarily tilted with respect to the IMF orientation. They use the term phase front normal (PFN) to describe the orientation of these surfaces, and use minimum variance analysis on sliding time segments of IMF measurements to determine the PFNs. In many aspects, the analyzed time segments are thus treated as discontinuities, although IMF variations within a time segment usually do not fulfill more formal classifications of a discontinuity suggested by, e.g., *Tsurutani and Smith* [1979] and *Lepping and Behannon* [1986].

[5] As pointed out by *Pulkkinen and Raststätter* [2009, hereafter PR09], one problem with the W03 method arises from the use of quality criteria imposed on the minimum variance analysis. Failure to satisfy these quality criteria can lead to “locking” to certain orientations of the phase fronts, and therefore an erroneous propagation time estimation. To circumvent this problem, PR09 suggested a modification which does not rely on these quality criteria, and which prevents abrupt changes in the phase front orientation. In this comment we point out some undesirable effects of the PR09 approach, and present an alternative solution.

[6] The outline of this paper is as follows. In section 2 we give a brief review of the W03 method and the alterations and optimizations proposed by PR09. In section 3 we point

<sup>1</sup>Department of Physics and Technology, University of Bergen, Bergen, Norway.

<sup>2</sup>Also at Max-Planck Institute for Solar Systems Research, Lindau, Germany.

<sup>3</sup>Department of Physics, Alexandru Ioan Cuza University of Iasi, Iasi, Romania.

<sup>4</sup>Physics Faculty, Yerevan State University, Yerevan, Armenia.

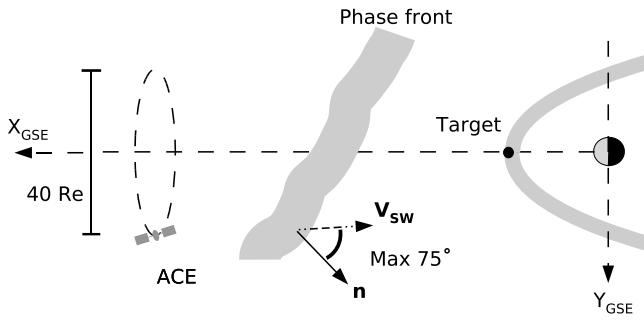


**Figure 1.** Illustration of the phase front method to calculate the solar wind propagation time between a monitor (here ACE) and a target (the Earth’s magnetopause). The real positions of the monitor and targets, as well as the phase front orientation (represented by its boundary normal,  $\vec{n}$ ), are taken into account. The predicted propagation time can then be calculated from the expression in equation (1) [after *Mailyan et al.*, 2008].

out and discuss some of the undesirable implications of the PR09 modifications. In section 4 we then present an alternate method to address some of the issues with the W03 method. Section 5 contains a summary and recommendations.

## 2. Brief Review of the *Weimer et al.* [2003] and *Pulkkinen and Rastst tter* [2009] Methods

[7] In the W03 method, illustrated in Figure 1, the orientation of an IMF phase front, represented by its boundary normal,  $\vec{n}$ , is essential. The propagation time,  $\tau$ , of a solar wind phase front from the monitor at position  $\vec{r}_{mon}$  to a target at  $\vec{r}_{tar}$  is given by

$$\tau = \frac{(\vec{r}_{mon} - \vec{r}_{tar}) \cdot \vec{n}}{\langle \vec{v} \rangle \cdot \vec{n}} \quad (1)$$

where  $\langle \vec{v} \rangle$  is the average solar wind bulk flow velocity within the sliding time segment.

[8] W03 uses minimum variance analysis of the magnetic field (MVAB) to obtain the normal. MVAB implies finding a new coordinate system organized according to the variance of the magnetic field. The direction of minimum variance serves as an estimator of the boundary normal of a structure. Mathematically, MVAB involves diagonalization of the magnetic covariance matrix to obtain a set of eigenvalues and eigenvectors which defines the new coordinate system [e.g., *Sonnerup and Scheible*, 1998].

[9] Although not explicitly apparent from the original W03 paper, the covariance matrix they used gave a normal direction almost (but not perfectly) perpendicular to the average magnetic field. *Bargatze et al.* [2005] and *Haaland et al.* [2006] pointed out that this property can be perfectly satisfied either by performing the MVA on a data set with the average B field subtracted, or by projecting the

covariance matrix from both sides with a projection matrix containing averages. As demonstrated by PR09, these two approaches are mathematically equivalent. In the literature, this form for minimum variance is sometimes referred to as MVAB0 (where the 0 is used to indicate the  $\langle \vec{B} \rangle \cdot \vec{n} = 0$  property) or MVABC, (where the C is for constrained (where the constrain may also be formulated to satisfy other properties) [see *Sonnerup et al.*, 2004, 2006]). Among others, the MVAB0 method is routinely used to generate time shifted solar wind data in the OMNI data set available from CDAWEB ([http://cdaweb.gsfc.nasa.gov/istp\\_public/](http://cdaweb.gsfc.nasa.gov/istp_public/)).

[10] Physically, the  $\langle \vec{B} \rangle \cdot \vec{n} = 0$  condition implies that the IMF phase fronts have the nature of tangential discontinuities (TDs); that is, there is no magnetic field along the normal and no flow of plasma through the discontinuity. Recent studies by, e.g., *Knetter et al.* [2004] seem to indicate that this assumption is valid, in particular for discontinuities in the solar wind, but also for time periods without any distinct discontinuities [*Weimer and King*, 2008; *Mailyan et al.*, 2008].

[11] A frequently used quality criteria for MVAB is the ratio between the three eigenvalues. Well separated eigenvalues,  $\lambda_{max} \gg \lambda_{int} \gg \lambda_{min}$  typically indicate well defined eigenvectors [*Sonnerup and Scheible*, 1998]. For the constrained MVAB0 analysis, the only sensible ratio is  $\lambda_{max}/\lambda_{int}$ , the ratio between the largest and the intermediate eigenvalue (the smallest eigenvalue will by definition be zero). W03 put certain minimum requirements on the eigenvalue ratio, and in a comprehensive benchmarking, *Weimer and King* [2008] found that optimal results were achieved if the eigenvalue ratio  $\lambda_{max}/\lambda_{int}$  was above 7.8. In addition to this eigenvalue threshold, they also required that the cone angle between the boundary normal and the solar wind bulk speed was below  $75^\circ$  (see Figure 1). For time segments where these criteria were not fulfilled, the previous valid phase front normal was used in the time delay calculation.

[12] As pointed out by PR09, a undesirable effect of the eigenvalue threshold was that the normal could remain “locked” in certain directions if the MVAB results did not provide eigenvalue ratios above this threshold. This locking can in theory also occur if the IMF phase planes change their orientation. A plausible explanation for poor MVA results is the presence of fluctuations caused by small-scale structures in the solar wind. PR09 therefore devised a method which did not utilize any eigenvalue thresholds at all, but instead uses a weight function to get smooth variations of the boundary normal:

$$\vec{n}(t_{j+1}) = \vec{n}(t_j) + \frac{2}{m} (\vec{n}^* - \vec{n}(t_j)) \Delta t \quad (2)$$

where  $\vec{n}^*$  is the phase front normal obtained from the W03 method,  $m$  is a weight factor and  $\Delta t$  is the sampling time of the IMF. This scheme is effectively a low-pass filtering of the IMF phase plane orientation. The weight factor  $m$  determines the degree of “smoothing.” Unlike the W03

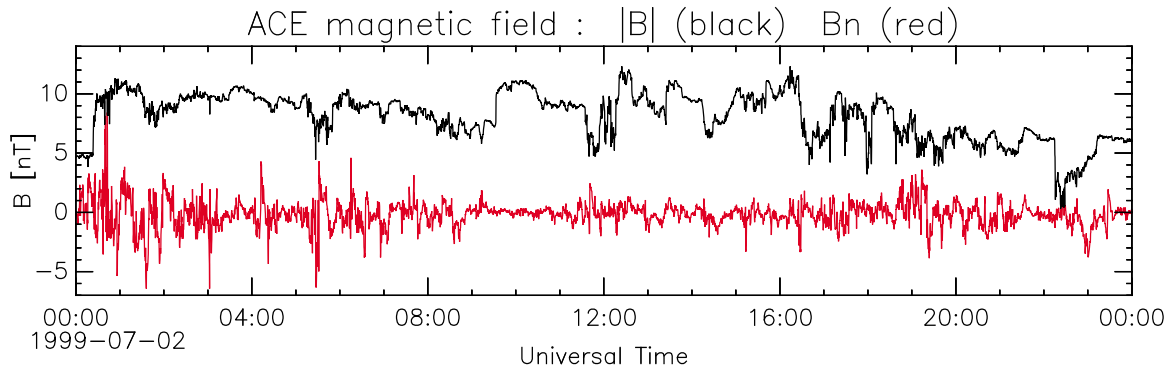


**Figure 2.** IMF magnitude (black line) and normal component of  $B$  ( $\langle \vec{B} \rangle \cdot \vec{n}$ ) (red line) resulting from application of the modification in the work by *Pulkkinen and Raststatter* [2009]. During some periods, the normal component constitutes a significant fraction of the total IMF.

method, the above approach provides a forward prediction of the orientation which may be of advantage for real time computations. The PR09 method also reduces the issue of one phase front overtaking another.

### 3. Implications of the Alterations Proposed by *Pulkkinen and Raststatter* [2009]

[13] While the alterations proposed by PR09 removes the locking in issue, two undesirable implications arise with this approach; First, the proposed modifications do not preserve the  $\langle \vec{B} \rangle \cdot \vec{n} = 0$  condition that is the underlying assumption in the W03 model, and which is the key to the success of the phase front method [*Bargatze et al.*, 2005]. Also, since the proposed modifications effectively acts as a low-pass filter, no sharp changes in the IMF phase plane orientation can occur. To our knowledge, however, no mechanisms preventing such sharp changes exist in nature.

[14] To demonstrate our concern, we refer to Figure 2, which shows the magnitude of the IMF and the normal component of IMF for the same event as shown in Figure 1 of PR09 (this time interval is also part of Figure 2 of *Weimer and King* [2008]). We have here calculated the normal according to equation (3) of PR09 (with the free parameter  $m = 30$ ) and projected it into the IMF measured by ACE. Both PR09 and *Weimer and King* [2008] write that they interpolate and resample the IMF data, but they do not elaborate on details. In this paper we have applied the interpolation and resampling procedure described by *Harvey and Schwartz* [1998]. Apparent from Figure 2 is the sometimes significant normal component (red line). For the time interval shown, the normal component is on average 11% of the total IMF magnitude, and during some periods, the normal magnetic field constitutes 98% of  $|B_{IMF}|$ , i.e., almost as big as the IMF itself. Recall that the normal component of the unmodified W03 model is by definition zero, which is also more in agreement with our present knowledge about solar wind discontinuities [e.g., *Knetter et al.*, 2004].

[15] Physically, a significant normal component in the magnetic field can be taken as an indication of ongoing reconnection, and hence transfer of plasma from one side to the other side of the phase plane surface. For a rotational discontinuity and any planar Alfvén wave, the plasma flow is proportional to the normal component [*Paschmann and Sonnerup*, 2008]. In theory, an independent check of to determine whether a structure is of Alfvénic nature can be done by consulting the plasma data, and performing the so-called Walén test [*Khrabrov and Sonnerup*, 1998a; *Paschmann and Sonnerup*, 2008]. However, due to the high flow speed of the solar wind, combined with the limited time resolution of present generation plasma instrumentation, one can at best only resolve structures with scale sizes of a few 1000 km. In the case of ACE, plasma data are routinely available at 64 s resolution [*McComas et al.*, 1998], corresponding to spatial resolutions of several 10,000 km.

[16] We should here strongly emphasize that we do not claim that the rotational discontinuities cannot exist in the solar wind (see, e.g., *Gosling et al.* [2009, and references therein] for an updated discussion about Alfvén fluctuations and reconnection in the solar wind). For this particular purpose, however, and given the insignificant improvement provided by the PR09 method, the assumption that the phase planes are TDs seem to be more justified. We therefore suggest that any improvements of the phase plane method should take this into account.

### 4. Proposal for an Alternative Method to Improve Boundary Normal Determination

[17] As pointed out, the PR09 modification is effectively a low-pass filtering of the phase front normal direction to exclude the effect of small-scale fluctuations in the IMF. Rather than using this approach, we propose that filtering should be performed on the input data to the MVAB, i.e., a filtering of the  $B$  field measurements. Also, instead of a

filtering in the frequency domain, we suggest to do the filtering in amplitude domain.

[18] A drawback with frequency filtering (averaging, low-pass filtering, using spin averages etc.) is that any sharp transitions in the data disappear. In particular for solar wind applications, the high solar wind bulk velocity cause shock fronts and discontinuities to be smeared out unless the time resolution of the measurements is sufficiently high. Furthermore, since MVAB is a statistical method, any reduction of the number of data points also increases the statistical uncertainty and thus error bounds for the variance analysis [Khrabrov and Sonnerup, 1998b; Sonnerup and Scheible, 1998].

[19] A method which has proved to yield better results is wavelet denoising. The original signal (the measured IMF) is then transformed into wavelet domain, which effectively decomposes the signal into a finite number of frequency and amplitude bins. The part of the signal that represents “noise” (in this case the low-amplitude fluctuations and wave activity) are then removed. Thereafter, the signal is transformed back into time domain again. If the signal in question is a vector, each component is treated individually.

[20] Any localized function,  $h(t)$ , can be used as a basis for wavelet transforms as long as it satisfies the *admissibility* criteria:

$$\int_{-\infty}^{\infty} h(t) dt = 0; \quad \int_{-\infty}^{\infty} |h(t)|^2 dt < \infty \quad (3)$$

For more information about wavelets types and wavelet denoising in general, we refer to papers by, e.g., Donoho [1992], Graps [1995], Daubechies [1992], and Torrence and Compo [1998, and references therein].

[21] Wavelet denoising, using Morlet wavelets, was tested out on magnetic field measurements obtained by the AMPTE IRM and UKS spacecraft during a series of magnetopause crossings by Haaland and Paschmann [2001]. The purpose of that study was to establish accurate boundary normals of the terrestrial magnetopause. Wavelet filtering of the input signal prior to MVAB gave an improvement of the eigenvalue ratio in 28 of 30 cases investigated.

[22] In Figure 3 we show some results from this technique applied to the IMF during the period 0500–0700 UT on 2 July 1997 (same event as discussed above, and also used for benchmarking by Weimer and King [2008] and PR09). The first three panels show the three GSE components of the IMF for this day. Black lines are the original measurements and the red lines show the “denoised” signal. In the wavelet domain, we have here removed (i.e., set to zero) all coefficients representing amplitudes below 2% of the total dynamic range of the signal, and then transformed back to the time domain. The large-scale variations, and in particular the fast rotations seen, e.g., in By component around 0612 UT are retained.

[23] It should be pointed out that we did not try any optimization at all on the wavelet filtering. The 2% threshold mentioned above is the same as that used by

Haaland and Paschmann [2001]. Further improvements can be achieved by adjusting the wavelet threshold and/or trying different data segment lengths.

[24] If we now use the denoised signal as input for the Weimer model, we obtain the eigenvalue ratios shown in the fourth panel of Figure 3. The average (i.e., both mean and median) eigenvalue ratio is now significantly improved. For the 2 h time interval (i.e., 480 samples with 15 s resolution) shown here, 165 samples fail to meet the eigenvalue ratio of 7.8 when using the unmodified measurements. For the denoised signal, only 64 samples fail to meet this threshold. For the full 24 h period as shown in Figure 2 of PR09, the corresponding numbers are 2192 and 796, respectively. Much of the arguments for the PR09 modifications are thus resolved.

[25] Alternatively, if phase front locking is not an issue, the use of wavelet denoised signals as inputs to the minimum variance allows for higher eigenvalue quality thresholds for the W03 method.

## 5. Summary

[26] In this paper, we have pointed out some undesirable effects of the MVA based propagation delay calculation presented by PR09. In particular, the sometimes dominant normal magnetic field component and the fact that no sharp changes in IMF are allowed, contradict our present understanding of solar wind phase planes and directional discontinuities in the solar wind. Although the sole purpose of the modifications suggested by PR09 was to improve the arrival prediction of solar wind phase fronts, we suggest that any tools and methods should be based on known physical properties of the solar wind.

[27] While we recognize that small-scale structures and fluctuations in the IMF can distort or invalidate minimum variance based normal determination, we suggest that any attempt to remove effects of such structures should be done in the input data. One way to achieve this is to use a wavelet based denoising technique for removal of such fluctuations. As demonstrated, the use of this technique largely reduces the issue which was the motivation for the modifications by PR09. Wavelet toolboxes are readily available for many software packages, so the implementation and application are not necessarily more complicated than the modification suggested by PR09. The required calculations are not very computer intensive, so near real-time denoising should also be possible.

[28] We have not tested how our alternate method performs for the MHD simulation by PR09 or any other real-time applications for that case. Given the insignificant improvement the PR09 method provided, and the number of other sources of complications for real-time space weather predictions, we remain somewhat sceptical. However, we plan to test out the denoising technique extensively on the data set discussed by Mailyan *et al.* [2008] to address this issue.

[29] The PR09 results demonstrate how important accurate solar wind input data can be for modeling pos-

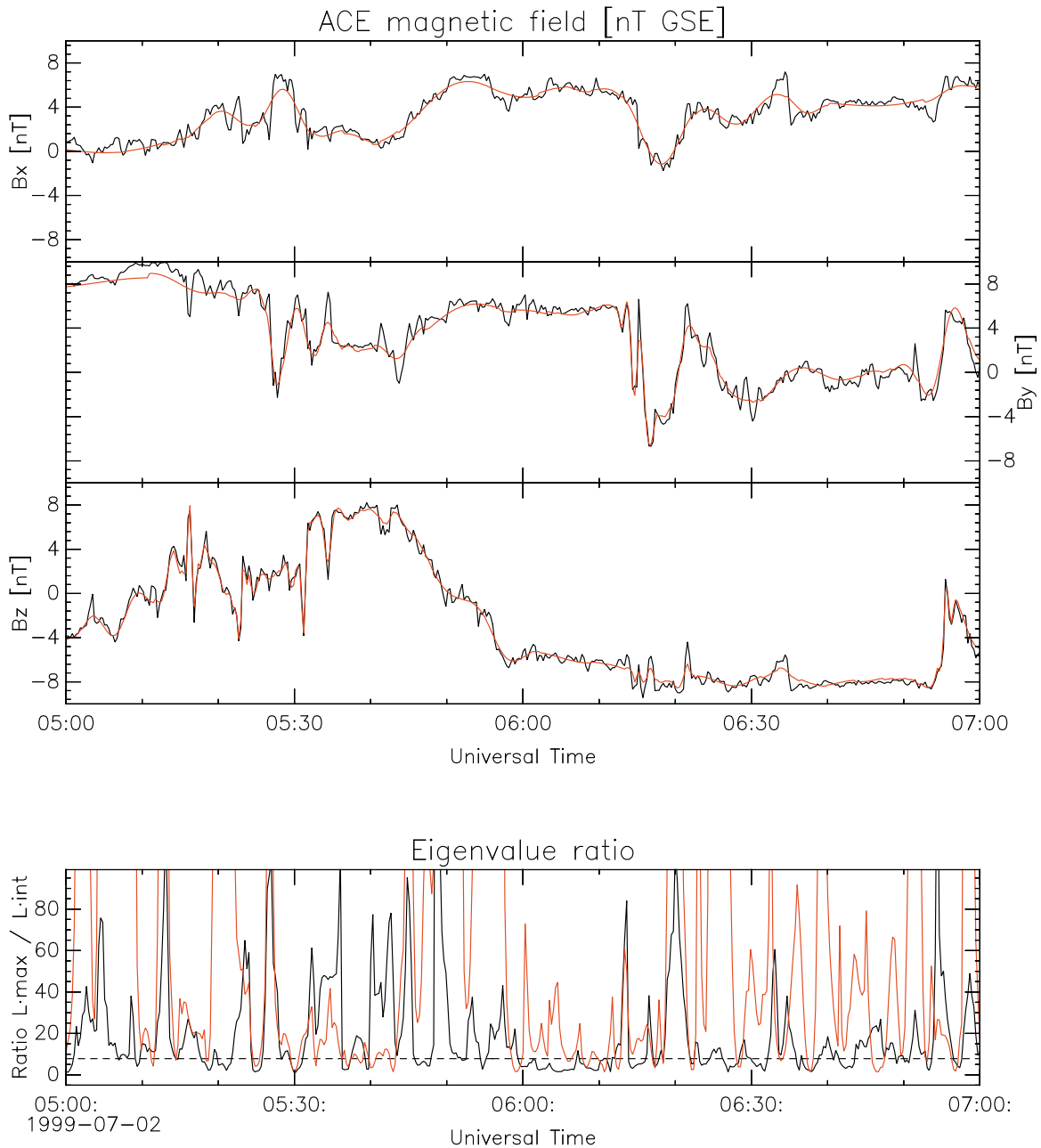


**Figure 3.** Time segment with results from the proposed wavelet denoising technique. First three panels show GSE components of the IMF at ACE. Solid black lines show the original ACE measurements but resampled to 15 s resolution as in the work by *Weimer et al.* [2003] and *Pulkkinen and Rastst tter* [2009]. Red lines are the corresponding denoised signal. Sharp transitions are retained, but small amplitude variations are removed. Fourth panel shows eigenvalue ratio  $\lambda_{\max}/\lambda_{\text{int}}$ . The black line shows the ratio for the standard W03 method, and the red line shows the corresponding ratio for the denoised signal. The eigenvalue ratio for the denoised signal is significantly higher, and a fewer periods fail the eigenvalue threshold of 7.8, marked with a dashed line in the fourth panel.

sible consequences of space weather. Accurate propagation delay calculations and methods are therefore essential elements for space weather forecasts.

[30] **Acknowledgments.** The computer code used for the calculations in this paper has been made available as part of the QSAS science analysis system. QSAS is provided by the United Kingdom Cluster Science Centre (Imperial College London and Queen Mary, University of London) supported by the United Kingdom Science and Technology Facilities Council. ACE data were obtained from the Coordinated Data Analysis Web (see <http://cdaweb.gsfc.nasa.gov/about.html>). We also thank the International Space Science Institute, Bern, Switzerland, for providing computer resources and infrastructure for data exchange.

## References

- Bargatze, L. F., R. L. McPherron, J. Minamora, and D. Weimer (2005), A new interpretation of Weimer et al.'s solar wind propagation delay technique, *J. Geophys. Res.*, **110**, A07105, doi:10.1029/2004JA010902.
- Daubechies, I. (1992), *Ten Lectures on Wavelets*, CBMS-NSF Reg. Conf. Ser. Appl. Math., vol. 61, Soc. for Ind. and Appl. Math., Philadelphia, Pa.
- Donoho, D. L. (1992), De-noising via soft thresholding, *Tech. Rep. 409*, Stanford Univ., Stanford, Calif.
- Gosling, J. T., D. J. McComas, D. A. Roberts, and R. M. Skoug (2009), A one-sided aspect of Alfvénic fluctuations in the solar wind, *Astrophys. J.*, **695**, L213–L216.
- Graps, A. (1995), An introduction to wavelets, *IEEE Comput. Sci. Eng.*, **2**, 50–61.
- Haaland, S., and G. Paschmann (2001), Improved boundary normal calculations using minimum variance analysis and wavelet de-noising techniques, in *Proceedings of Les Woolliscroft Memorial Conference*, edited by B. Warmbein, *Eur. Space Agency Spec. Publ.*, ESA SP-492, 127–132.
- Haaland, S., G. Paschmann, and B. U. Ö. Sonnerup (2006), Comment on "A new interpretation of Weimer et al.'s solar wind propagation delay technique" by Bargatze et al., *J. Geophys. Res.*, **111**, A06102, doi:10.1029/2005JA011376.
- Harvey, C. C., and S. J. Schwartz (1998), Time series resampling methods, in *Analysis Methods for Multi-Spacecraft Data*, edited by G. Paschmann and P. W. Daly, *ISSI Sci. Rep. 001*, pp. 43–64, ESA Publ. Div., Noordwijk, Netherlands.
- Khrabrov, A. V., and B. U. Ö. Sonnerup (1998a), deHoffmann-Teller analysis, in *Analysis Methods for Multi-Spacecraft Data*, edited by G. Paschmann and P. W. Daly, *ISSI Sci. Rep. 001*, pp. 221–248, ESA Publ. Div., Noordwijk, Netherlands.
- Khrabrov, A. V., and B. U. Ö. Sonnerup (1998b), Error estimates for minimum variance analysis, *J. Geophys. Res.*, **103**, 6641–6651.
- Knetter, T., F. M. Neubauer, T. Horbury, and A. Balogh (2004), Four-point discontinuity observations using Cluster magnetic field data: A statistical survey, *J. Geophys. Res.*, **109**, A06102, doi:10.1029/2003JA010099.
- Lepping, R. P., and K. W. Behannon (1986), Magnetic field directional discontinuities: Characteristics between 0.46 and 1.0 AU, *J. Geophys. Res.*, **91**, 8725–8741.
- Mailyan, B., C. Munteanu, and S. Haaland (2008), What is the best method to calculate the solar wind propagation delay?, *Ann. Geophys.*, **26**, 2383–2394.
- McComas, D. J., S. J. Bame, P. Barker, W. C. Feldman, J. L. Phillips, P. Riley, and J. W. Griffee (1998), Solar Wind Electron Proton Alpha Monitor (SWEPAM) for the Advanced Composition Explorer, *Space Sci. Rev.*, **86**, 563–612.
- Paschmann, G., and B. U. Ö. Sonnerup (2008), Proper frame determination and Walén test, in *Multi-Spacecraft Analysis Methods Revisited*, edited by G. Paschmann and P. W. Daly, *ISSI Sci. Rep. 008*, pp. 65–74, ESA Comm., Noordwijk, Netherlands.
- Pulkkinen, A., and L. Raststatter (2009), Minimum variance analysis-based propagation of the solar wind observations: Application to real-time global magnetohydrodynamic simulations, *Space Weather*, **7**, S12001, doi:10.1029/2009SW000468.
- Sonnerup, B. U. Ö., and M. Scheible (1998), Minimum and maximum variance analysis, in *Analysis Methods for Multi-Spacecraft Data*, edited by G. Paschmann and P. W. Daly, *ISSI Sci. Rep. 001*, pp. 185–220, ESA Publ. Div., Noordwijk, Netherlands.
- Sonnerup, B. U. Ö., S. Haaland, G. Paschmann, B. Lavraud, M. W. Dunlop, H. Rème, and A. Balogh (2004), Orientation and motion of a discontinuity from single-spacecraft measurements of plasma velocity and density: Minimum mass flux residue, *J. Geophys. Res.*, **109**, A03221, doi:10.1029/2003JA010230.
- Sonnerup, B. U. Ö., S. Haaland, G. Paschmann, M. W. Dunlop, H. Rème, and A. Balogh (2006), Orientation and motion of a plasma discontinuity from single-spacecraft measurements: Generic residue analysis of Cluster data, *J. Geophys. Res.*, **111**, A05203, doi:10.1029/2005JA011538.
- Torrence, C., and G. P. Compo (1998), A practical guide to wavelet analysis, *Bull. Am. Meteorol. Soc.*, **79**, 61–78.
- Tsurutani, B. T., and E. J. Smith (1979), Interplanetary discontinuities: Temporal variations and the radial gradient from 1 to 8.5 AU, *J. Geophys. Res.*, **84**, 2773–2787.
- Weimer, D. R., and J. H. King (2008), Improved calculations of interplanetary magnetic field phase front angles and propagation time delays, *J. Geophys. Res.*, **113**, A01105, doi:10.1029/2007JA012452. (Correction, *J. Geophys. Res.*, **113**, A07106, doi:10.1029/2008JA013075.)
- Weimer, D. R., D. M. Ober, N. C. Maynard, M. R. Collier, D. J. McComas, N. F. Ness, C. W. Smith, and J. Watermann (2003), Predicting interplanetary magnetic field (IMF) propagation delay times using the minimum variance technique, *J. Geophys. Res.*, **108**(A1), 1026, doi:10.1029/2002JA009405. (Correction, *J. Geophys. Res.*, **109**, A12104, doi:10.1029/2004JA010691.)

S. Haaland, Department of Physics and Technology, University of Bergen, N-5020 Bergen, Norway. (stein.haaland@issi.unibe.ch)

B. Mailyan, Physics Faculty, Yerevan State University, Yerevan, Armenia. (bagrat\_mailyan@yahoo.co.uk)

C. Munteanu, Department of Physics, Alexandru Ioan Cuza University of Iasi, 700506 Iasi, Romania. (munteanu\_costel\_22@yahoo.com)

# Paper III



## Propagation delay of solar wind discontinuities: Comparing different methods and evaluating the effect of wavelet denoising

C. Munteanu,<sup>1,2,3</sup> S. Haaland,<sup>4,5</sup> B. Mailyan,<sup>6</sup> M. Echim,<sup>1,7</sup> and K. Mursula<sup>2</sup>

Received 14 November 2012; revised 29 May 2013; accepted 30 June 2013; published 23 July 2013.

[1] We present a statistical study of the performance of three methods used to predict the propagation delay of solar wind structures. These methods are based on boundary normal estimations between the Advanced Composition Explorer (ACE) spacecraft orbiting the L1 libration point and the Cluster spacecraft near the Earth's magnetopause. The boundary normal estimation methods tested are the cross product method (CP), the minimum variance analysis of the magnetic field (MVAB), and the constrained minimum variance analysis (MVAB0). The estimated delay times are compared with the observed ones to obtain a quantitative measure of each method's accuracy. Boundary normal estimations of magnetic field structures embedded in the solar wind are known to be sensitive to small-scale fluctuations. Our study uses wavelet denoising to reduce the effect of these fluctuations. The influence of wavelet denoising on the performance of the three methods is also analyzed. We find that the free parameters of the three methods have to be adapted to each event in order to obtain accurate propagation delays. We also find that by using denoising parameters optimized to each event, 88% of our database of 356 events are estimated to arrive within  $\pm 2$  min from the observed time delay with MVAB, 74% with CP, and 69% with the MVAB0 method. Our results show that wavelet denoising significantly improves the predictions of the propagation time delay of solar wind discontinuities.

**Citation:** Munteanu, C., S. Haaland, B. Mailyan, M. Echim, and K. Mursula (2013), Propagation delay of solar wind discontinuities: Comparing different methods and evaluating the effect of wavelet denoising, *J. Geophys. Res. Space Physics*, 118, 3985–3994, doi:10.1002/jgra.50429.

### 1. Introduction

[2] Due to the lack of continuous monitoring of solar wind properties close to the Earth, solar wind measurements often need to be translated from an upstream monitor to the Earth's bow shock location. To accurately predict the propagation time of magnetic field structures embedded in the solar wind, one needs to take into account the orientation of the boundary normal of those structures. The challenge here is that most methods used to estimate these boundary normals are affected by small-scale fluctuations superposed on the magnetic field structure. Instead of using frequency filtering, which smears out the discontinuities and reduces the number of data points, we use wavelet denoising to reduce the effect of these fluctuations. Wavelet denoising is especially

suited to remove low-amplitude high-frequency fluctuations while leaving the high-amplitude low-frequency parts of the signal unchanged.

[3] *Horbury et al.* [2001] used data from Advanced Composition Explorer (ACE) and Wind spacecrafts to study the propagation time of discontinuities characterized by southward interplanetary magnetic field (IMF) turnings. They showed that the best estimates of the propagation time were obtained when the orientation of discontinuities was calculated with the cross product method (CP), which assumes that the boundary normal is given by the cross product between the mean magnetic field upstream of the discontinuity and the mean magnetic field downstream of it.

[4] *Mailyan et al.* [2008] studied statistically the propagation time of about 200 IMF structures between ACE and Cluster. They computed the propagation time using four different methods: the flat delay method (FD), which assumes a constant convective motion of the structure along the Sun-Earth line, the CP method, the minimum variance analysis (MVAB), and the constrained minimum variance analysis (MVAB0) finding that the best results are obtained with MVAB0.

[5] *Pulkkinen and Rastätter* [2009] proposed a new method for computing the boundary normals of solar wind discontinuities. One of their motivations was the removal of the influence of small-scale fluctuations on the computed normals. Their method, based on MVAB0, uses a weight function to get smooth variations of the boundary normal,

<sup>1</sup>Institute of Space Sciences, Magurele, Romania.

<sup>2</sup>Department of Physics, University of Oulu, Oulu, Finland.

<sup>3</sup>Department of Physics, University of Bucharest, Magurele, Romania.

<sup>4</sup>Birkeland Center for Space Science, University of Bergen, Bergen, Norway.

<sup>5</sup>Max Planck Institute for Solar Systems Research, Lindau, Germany.

<sup>6</sup>Yerevan Physics Institute, Yerevan, Armenia.

<sup>7</sup>Belgian Institute for Space Aeronomy, Brussels, Belgium.

Corresponding author: C. Munteanu, Institute of Space Sciences, Atomistilor 409, P.O. Box MG-23, Bucharest-Magurele RO-077125, Romania. (costelm@spacescience.ro)

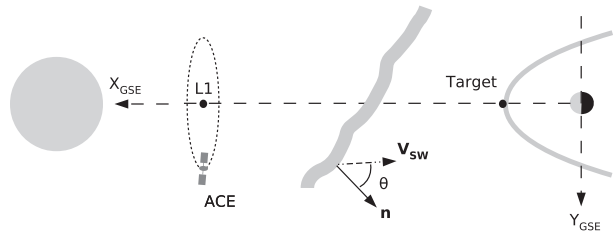


**Figure 1.** Illustration of a solar wind discontinuity propagating from ACE to Cluster (Target). Positions of the Sun, Earth, ACE and Cluster spacecraft, and the model discontinuity and its normal  $\mathbf{n}$  at angle  $\theta$  with respect to the solar wind velocity  $\mathbf{V}_{SW}$  are shown. Note that this is just a sketch and both position and dimensions are not to scale (adapted from *Mailyan et al.* [2008]).

thus effectively low-pass filtering the computed normals. To test their time shift method, they used a global MHD model that computed the ground magnetic field. Although their method did provide some improvement in the timing of the modeled magnetic field, the improvements were not systematic and could not be detected in a statistical sample.

[6] *Haaland et al.* [2010] proposed a different approach of improving the boundary normal determination. They emphasized that the filtering should be performed on the input data rather than on the obtained normals. Also, instead of frequency filtering, they suggested the use of wavelet denoising, which was already tested on magnetic field measurements by *Haaland and Paschmann* [2001].

[7] Our study extends the analysis in *Mailyan et al.* [2008] by including the effect of wavelet denoising on the timing accuracy of three propagation delay estimation methods: CP, MVAB, and MVAB0. We also analyze the effect of varying the free parameters of the three methods on the timing accuracy.

[8] The paper is organized as follows. Section 2 presents the data sources and database of events. Section 3 discusses the time delay estimation methods. In section 4 we describe the approach adopted for wavelet denoising. Section 5 illustrates the results obtained for a case study, and section 6 gives the statistical results of the study. Section 7 summarizes the paper.

**2. Data Description**

[9] We use data from the ACE spacecraft in the solar wind and the Cluster spacecraft near the Earth’s magnetopause. ACE orbits the L1 libration point at approximately  $1.5 \times 10^6$  km upstream of the Earth. Cluster contains four identical satellites flying in close formation around the Earth. It has a  $90^\circ$  inclination elliptical polar orbit, with perigee at  $4 R_E$ , apogee around  $20 R_E$ , and orbital period of approximately 57 h. Cluster’s apogee is in the upstream solar wind mainly from January to April every year, so our study will focus only on this period.

[10] In this work we use ACE magnetic field data from the MAG instrument [*Smith et al.*, 1998] at 16 s resolution and solar wind velocity data from the Solar Wind Electron, Proton, and Alpha Monitor instrument [*McComas et al.*,

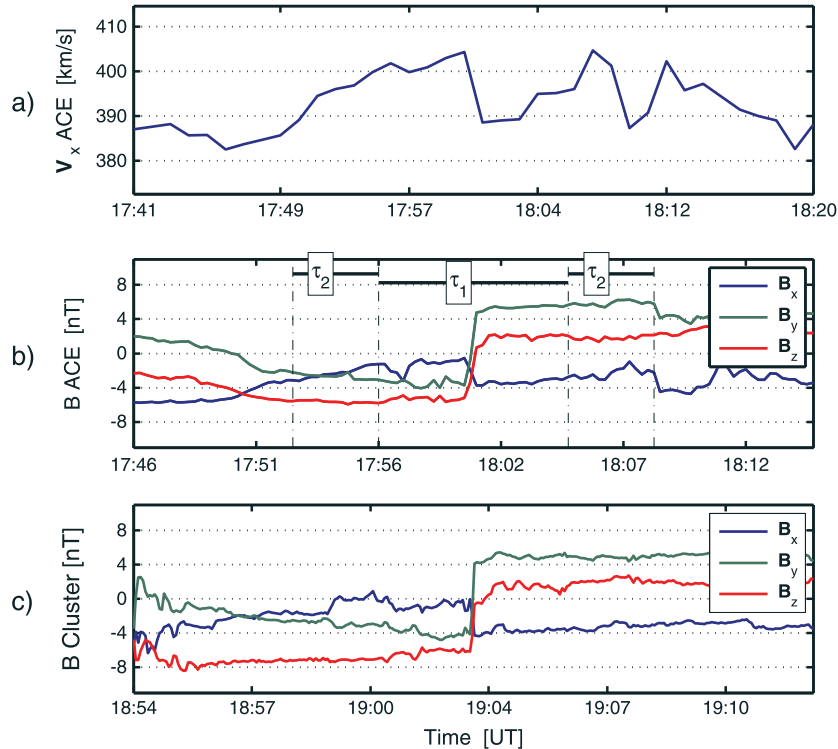


**Figure 2.** Sample IMF discontinuity observed by ACE and Cluster 3 on 06 January 2003: (a)  $X$  component of the solar wind velocity measured by ACE; (b) magnetic field components measured by ACE; (c) magnetic field components at C3 location. Figure 2b also depicts the time interval  $\tau_1 = 8$  min centered on the discontinuity and the time intervals  $\tau_2 = 4$  min on each side of  $\tau_1$ , used in the cross product (CP) method. In Figures 2b and 2c, blue, green, and red lines indicate  $B_x$ ,  $B_y$ , and  $B_z$  components of the IMF.

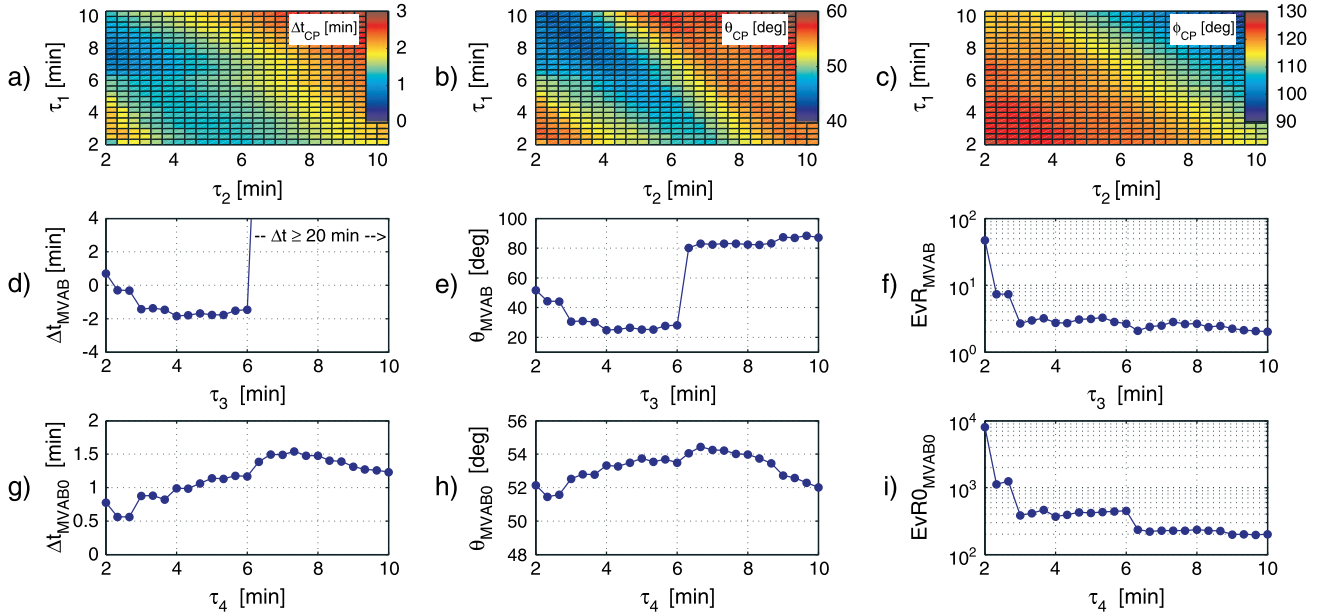


**Figure 3.** Illustration of the effect of varying the parameters of time delay estimation methods on the estimation accuracy and on the quality criteria of boundary normal estimation applied on the data from the 06 January 2003 event. The first row shows the CP method results: (a) the time delay estimation accuracy  $\Delta t_{CP} = t_{CP} - t_{observed}$  as a function of  $\tau_1$  and  $\tau_2$ , (b) the orientation angle  $\theta_{CP}$  as a function of  $\tau_1$  and  $\tau_2$ , and (c) the shear angle  $\phi_{CP}$  (the angle between the mean upstream and downstream magnetic field vectors) as a function of  $\tau_1$  and  $\tau_2$ . The second row shows the MVAB method results: (d) the time delay estimation accuracy  $\Delta t_{MVAB}$  as a function of  $\tau_3$ , (e) the orientation angle  $\theta_{MVAB}$  as a function of  $\tau_3$ , and (f) the eigenvalue ratio  $EvR_{MVAB}$  as a function of  $\tau_3$ . The third row shows the MVAB0 results: (g) the time delay estimation accuracy  $\Delta t_{MVAB0}$  as a function of  $\tau_4$ , (h) the orientation angle  $\theta_{MVAB0}$  as a function of  $\tau_4$ , and (i) the eigenvalue ratio  $EvR0_{MVAB0}$  as a function of  $\tau_4$ .

1998] at 64 s resolution. Cluster data are from the Fluxgate Magnetometer (FGM—see *Balogh et al.*, 2001) and from the Cluster Ion Spectroscopy (CIS) experiment [*Rème et al.*, 2001], both at 4 s time resolution. Since we focus on the propagation delay of solar wind discontinuities between two points, most of the Cluster measurements are taken only from one spacecraft, Cluster 3, from now on referred as C3.

[11] Our database consists of 356 solar wind discontinuities observed by both ACE and C3 in the period 2001–2012. This database expands the data set used in *Mailyan et al.* [2008]. We first identified clear magnetic field rotations in C3 measurements by visually examining the Cluster summary plots. Since we focus on periods when C3 is in the upstream solar wind, we also examined the Cluster nominal position and the ion temperature (from the CIS experiment) to avoid any influences of bow shock processes (*Gosling et al.* [1978], *Paschmann et al.* [1981], and, for a recent review, *Burgess et al.* [2012]). Then we examined the ACE magnetic field measurements about an hour earlier in order to see if the same field rotation could be found there. Throughout the paper we will interchangeably use the terms “magnetic field structure,” “magnetic field rotation,” “directional discontinuity,” or just “discontinuity.” From a theoretical point of view this is not completely correct, but, for the purpose of our study, every amplitude change of at least 5 nT in less than  $\sim 5$  min in one or more components of the magnetic field is considered a discontinuity.

[12] All the satellite data were downloaded through the Automated Multi Dataset Analysis system (AMDA)

[*Jacquey et al.*, 2010] (<http://cdpp-amda.cesr.fr/DDHTML/index.html>), a web-based facility for online data analysis of space physics data.

### 3. Time Delay Estimation Methods

[13] IMF discontinuities are considered to be locally planar structures tilted at arbitrary angles with respect to the Sun-Earth line. The configuration of a solar wind discontinuity propagating from ACE to C3 spacecraft is illustrated in Figure 1. The tilt of the discontinuity with respect to the flow direction, referred to as  $\theta$  angle, and the displacement of the two satellites from the Sun-Earth line can have an important influence on the estimated time delay between the two satellites. Assuming that the radial propagation speed of the discontinuity is given by the projection of the solar wind velocity vector  $\mathbf{V}_{SW}$  onto the boundary normal direction  $\mathbf{n}$  and that the relative distance between the two observation points with respect to the discontinuity is the observed distance  $\mathbf{D}$  projected onto  $\mathbf{n}$ , the time delay  $dt$  between the two points is given by

$$dt = \frac{\mathbf{D} \cdot \mathbf{n}}{\mathbf{V}_{SW} \cdot \mathbf{n}}. \quad (1)$$

We use here three boundary normal estimation methods : CP, MVAB, and MVAB0 (as in *Mailyan et al.* [2008]). The CP method assumes that the discontinuity normal is given by the cross product between the mean upstream magnetic field  $\mathbf{B}_1$

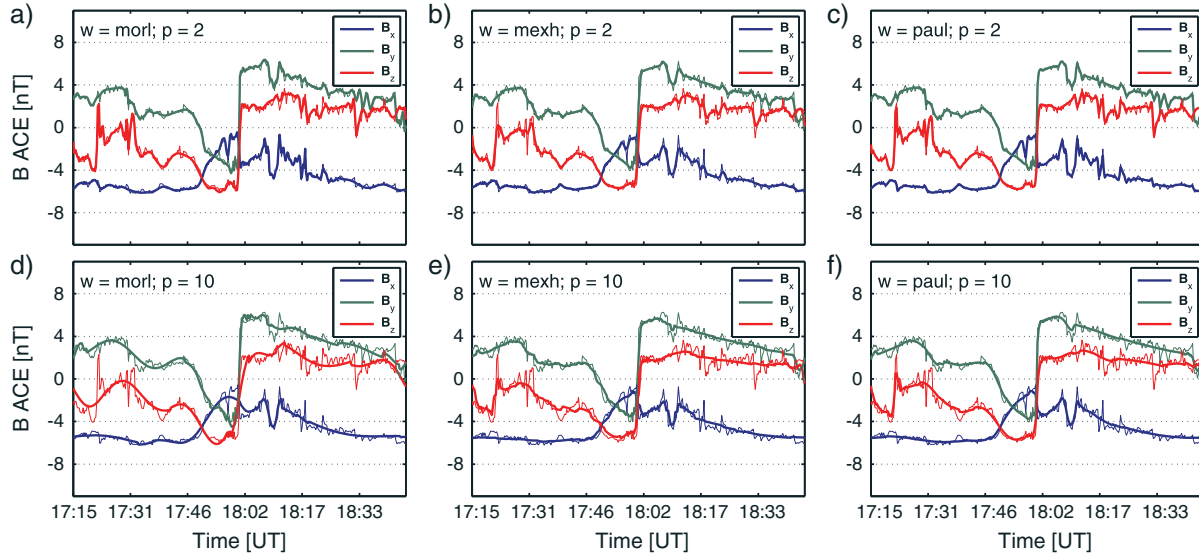


**Figure 4.** Illustration of wavelet denoising for the event on 06 January 2003. Shown are the denoising results for the Morlet wavelet function at the threshold levels (a)  $p = 2$  and (d)  $p = 10$ , the Mexican Hat wavelet at (b)  $p = 2$  and (e)  $p = 10$ , and Paul wavelet at (c)  $p = 2$  and (f)  $p = 10$ . Blue, green, and red lines indicate original (thin lines) and denoised (thick lines)  $\mathbf{B}_x$ ,  $\mathbf{B}_y$ , and  $\mathbf{B}_z$  components of the magnetic field measured by ACE.

and the mean downstream magnetic field  $\mathbf{B}_2$  [Colburn and Sonett, 1966]:

$$\mathbf{n}_{\text{CP}} = \frac{\mathbf{B}_1 \times \mathbf{B}_2}{|\mathbf{B}_1 \times \mathbf{B}_2|}. \quad (2)$$

Strictly speaking, equation (2) is valid only in case of tangential or quasi-tangential discontinuities (TDs), i.e., planar structures with zero magnetic field along the normal [Colburn and Sonett, 1966]. The use of the CP method is justified by the fact that the large majority of our discontinuities have a small magnetic field normal component (as shown in Figure 11 along with other results). To compute the two vectors, we need to set two time intervals:  $\tau_1$  and  $\tau_2$ . The time interval  $\tau_1$  is centered on the discontinuity with its left margin coinciding with the end point of a time interval of length  $\tau_2$  over which the average field at “left,”  $\mathbf{B}_1$ , is computed. The right margin of  $\tau_1$  coincides with the first point of a time interval of length  $\tau_2$  over which the average field at “right,”  $\mathbf{B}_2$ , is computed (see Figure 2 for a graphical representation of the two time intervals). The uncertainty in boundary normal estimation increases with increasing collinearity between  $\mathbf{B}_1$  and  $\mathbf{B}_2$  [Knetter, 2005]. The shear angle  $\phi$ , i.e., the angle between  $\mathbf{B}_1$  and  $\mathbf{B}_2$ , and the  $\theta$  angle can be used as quality factors for the normal estimation. Mailyan et al. [2008] showed that values of  $\theta$  larger than  $\sim 70^\circ$  can lead to erroneous time delay estimations.

[14] MVAB is the most frequently used method to obtain the orientation of a planar magnetic field structure [see, e.g., Sonnerup and Scheible, 1998]. One first computes the eigenvectors and eigenvalues of the covariance matrix of magnetic field measurements,  $\mathbf{M}_{v\mu}$ :

$$\mathbf{M}_{v\mu} = \langle B_\mu B_\nu \rangle - \langle B_\mu \rangle \langle B_\nu \rangle, \quad (3)$$

where  $\langle \dots \rangle$  denotes averaging over a certain time interval centered on the discontinuity, indicated here as  $\tau_3$ . The eigenvector corresponding to the smallest eigenvalue is used as an estimator for the boundary normal  $\mathbf{n}_{\text{MVAB}}$ . The ratio

between the intermediate and minimum eigenvalues, called  $EvR_{\text{MVAB}}$ , and the  $\theta$  angle can be used as quality factors of the normal estimation [Mailyan et al., 2008].

[15] Previous studies about solar wind discontinuities suggest that most of them resemble TDs [Knetter, 2005]. Knowing this, we can estimate the boundary normal using the constrained minimum variance analysis (MVAB0), where the normal magnetic field is zero by definition [Sonnerup and Scheible, 1998]. In MVAB0, the covariance matrix  $\mathbf{M}_{v\mu}$  (equation (3)) is replaced by

$$\mathbf{Q}' = \mathbf{P}_{ik} M_{v\mu} \mathbf{P}_{nj} \text{ with } : \mathbf{P}_{ij} = \delta_{ij} - \mathbf{b}_i \mathbf{b}_j, \quad (4)$$

where  $\delta_{ij} = 1$  for  $i = j$  and 0 otherwise, and  $\mathbf{b} = \langle \mathbf{B} \rangle / |\langle \mathbf{B} \rangle|$  is the direction of the average magnetic field. The time interval  $\tau_4$  centered on the discontinuity and used to calculate the covariance matrix  $\mathbf{Q}'$  is a free parameter in MVAB0. The eigenvalues and eigenvectors of  $\mathbf{Q}'$  have now a different meaning: the lowest eigenvalue is zero, and its corresponding eigenvector is  $\mathbf{b}$ . The eigenvector corresponding to the lowest nonzero eigenvalue is now the normal estimator  $\mathbf{n}_{\text{MVAB0}}$ . The ratio between the maximum and intermediate eigenvalues, called  $EvR0_{\text{MVAB0}}$ , and the  $\theta$  angle can be used as quality factors of the normal estimation [Mailyan et al., 2008].

[16] The results from the above mentioned three methods are also compared with the results obtained assuming a simple convective motion of discontinuities along the Sun-Earth line, referred to in the literature as the flat delay method (FD) [Mailyan et al., 2008]. Here, the time delay between the two observation points is given by

$$dt_{\text{FD}} = \frac{\mathbf{D}_x}{\mathbf{V}_x}, \quad (5)$$

where  $\mathbf{D}_x$  is the  $\mathbf{X}_{\text{GSE}}$  component of the distance  $\mathbf{D}$  between ACE and C3 and  $\mathbf{V}_x$  is the  $\mathbf{X}_{\text{GSE}}$  component of the solar wind velocity vector  $\mathbf{V}_{\text{SW}}$ .

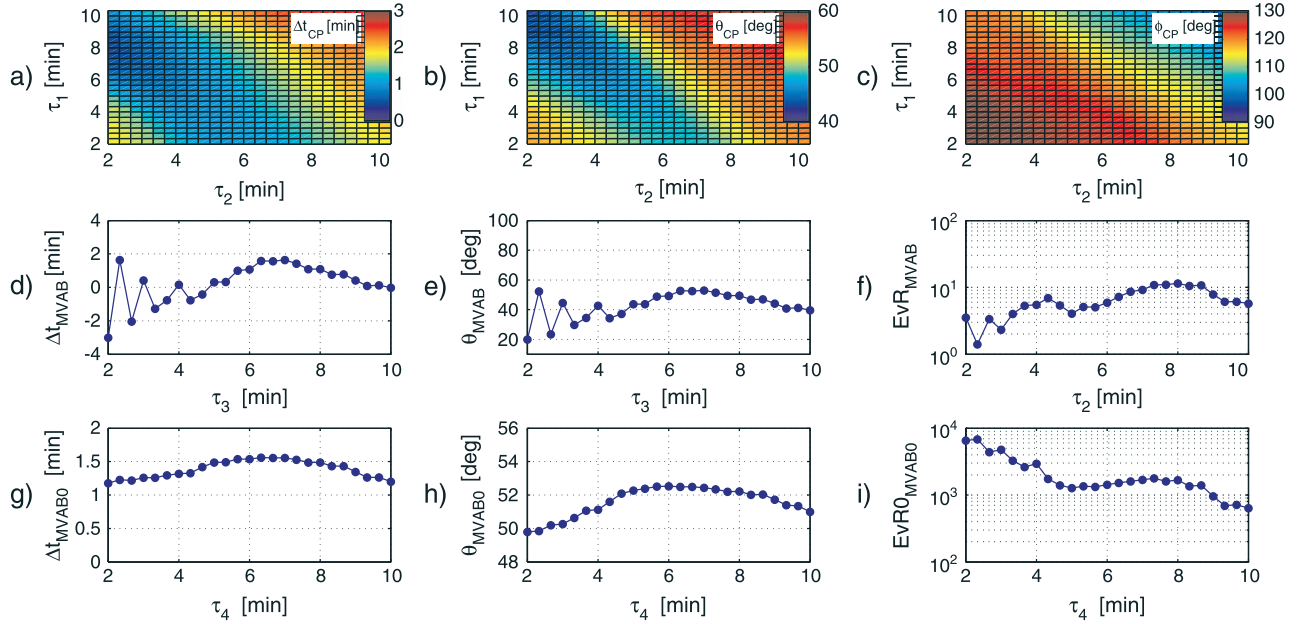


**Figure 5.** Illustration of the effect of model parameters on the accuracy of time delay estimation and quality criteria for the wavelet denoised data (Morlet,  $p = 10$ ) shown in Figure 4d. The format is the same as in Figure 3.

#### 4. Wavelet Denoising

[17] Wavelet denoising is a powerful technique bearing similarities with frequency filtering. Instead of removing frequency components from the signal, wavelet denoising removes certain wavelet coefficients based on their amplitude. The continuous wavelet transform of a time series  $f(t)$  is

$$T(a, b) = \int_{-\infty}^{\infty} f(t) \psi^{a,b}(t) dt, \quad \text{with } \psi^{a,b}(t) = a^{-1/2} \psi\left(\frac{t-b}{a}\right), \quad (6)$$

where  $a$  is the scale parameter,  $b$  is the translation parameter,  $\psi$  is the wavelet mother function, and  $T(a, b)$  is the wavelet coefficients matrix (see, e.g., *Daubechies* [1992] for more details).

[18] The large-amplitude low-frequency components of the time series and the low-amplitude high-frequency ones (the “noise”) are occupying different amplitude ranges in the coefficients matrix  $T(a, b)$ . Our study uses hard thresholding as a wavelet denoising method, in which all wavelet coefficients below a certain amplitude level are set to zero. The threshold amplitude level  $p$  is defined here as a percentage of the total amplitude range of the coefficients matrix. For example, a denoising with  $p = 0$  leaves the time series unchanged while a denoising with  $p = 10$  sets to zero all coefficients with amplitudes smaller than 10% of the total amplitude range of the matrix  $T(a, b)$ . The resulting wavelet coefficients are defined as

$$T^d(a, b) = \begin{cases} T(a, b), & \text{if } |T(a, b)| > (p/100) \cdot \max(|T(a, b)|), \\ 0, & \text{if } |T(a, b)| \leq (p/100) \cdot \max(|T(a, b)|). \end{cases} \quad (7)$$

There is also the possibility of using soft thresholding, where all wavelet coefficients are translated toward zero by the amount  $(p/100) \cdot \max(|T(a, b)|)$  [*Donoho*, 1995]. The soft thresholding technique was devised in order to preserve the smoothness of the original signal after denoising. Since we

are interested only in preserving the sharp discontinuities, the hard thresholding method is more appropriate.

[19] Because the continuous wavelet transform is redundant, there is no unique way of defining a reconstruction formula. The inverse continuous wavelet transform is presented classically in the double integral form:

$$f^d(t) = C_\psi \int_a \int_b a^{-2} T^d(a, b) \psi^{a,b}(t) da db, \quad (8)$$

where  $C_\psi$  is a constant depending only on the wavelet mother function  $\psi$  (empirically derived values of  $C_\psi$  for some commonly used wavelet functions are given in *Torrence and Compo* [1998]).

[20] An important factor to be considered in wavelet analysis is the wavelet shape, which should reflect the type of features present in the time series. We tested three families of wavelets: Morlet, known to be accurate in the frequency domain, Paul that has a good time resolution, and the second derivative of a Gaussian, also known as the Mexican Hat wavelet, that has lower frequency and time resolutions [*De Moortel et al.*, 2004]). Since our denoising thresholds are very low, i.e., only a small fraction of the signal is removed, properties such as frequency and time resolution will not have a profound effect on the reconstructed time signal. The effects of the wavelet basis on the denoising are discussed in sections 5 and 6.

[21] As used here, wavelet denoising has two free parameters: the wavelet function  $\psi$  and the threshold level  $p$ . Values of  $p$  larger than  $\sim 10$  lead to the smearing out of discontinuities; therefore, the maximum value of  $p$  is set to 10. This is by no means the only way of denoising a time series using wavelet-based algorithms, and we plan to extend our study in subsequent papers by testing other denoising schemes. The denoising procedure described above is applied independently to each of the three components of the magnetic

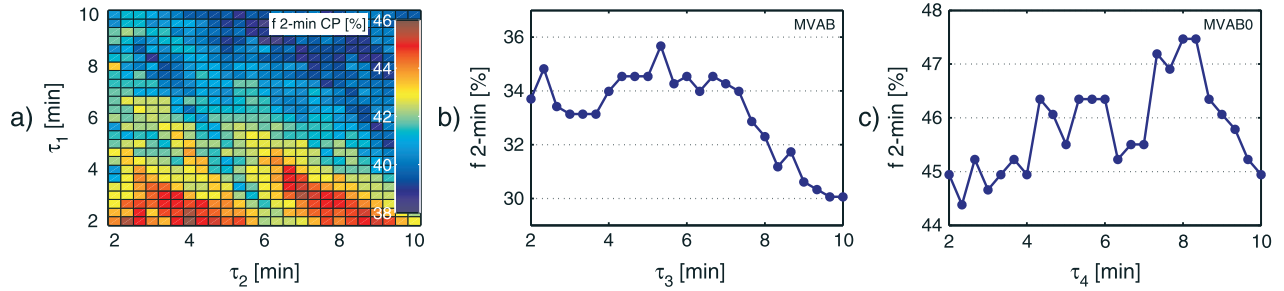


**Figure 6.** The fraction of discontinuities with time delay accuracy  $\Delta t$  within  $\pm 2$  min,  $f_{2\text{-min}}$ , as a function of method parameters:  $f_{2\text{-min}}$  for (a) CP as a function  $\tau_1$  and  $\tau_2$ , (b) for MVAB as a function  $\tau_3$ , and (c) for MVAB0 as a function of  $\tau_4$ . The parameters that maximize the 2 min fractions are  $\tau_1^m = 2$  min and  $\tau_2^m = 4$  min for CP, and  $\tau_3^m = 5.33$  min and  $\tau_4^m = 8.33$  min for MVAB and MVAB0, respectively.

field. Further details about wavelet denoising can be found in Donoho and Johnstone [1995], Donoho [1995], and Donoho et al. [1995].

### 5. Case Study, 6 January 2003

[22] Figure 2 shows a sample discontinuity observed by ACE at 18:01 UT on 06 January 2003. Figures 2a and 2b depict the  $X$  component of the solar wind velocity and the magnetic field measured by ACE respectively, while the magnetic field measurements of the same discontinuity detected by C3 at 19:03 UT are shown in Figure 2c. The observed time delay,  $dt_{\text{obs}}$ , between ACE and C3 is in this case 62 min.

[23] We have computed the time delay accuracy  $\Delta t_{\text{met}} = dt_{\text{met}} - dt_{\text{obs}}$ , where  $dt_{\text{met}}$  is the time delay estimated using one of the three methods (CP, MVAB, or MVAB0), and also the related quality factors ( $\theta_{\text{met}}$ ,  $\phi_{\text{CP}}$ ,  $EvR_{\text{MVAB}}$ , and  $EvR0_{\text{MVAB0}}$ ). The results are shown in Figure 3. The parameters  $\tau_1$ ,  $\tau_2$ ,  $\tau_3$ , and  $\tau_4$  are varied from 2 to 10 min, with a step size of  $1/3$  min  $\approx 0.33$  min. The choice of the  $1/3$  min (20 s)

time step is motivated mainly by the time resolution of ACE magnetic field data (16 s). If we had used an increment of  $1/4$  min (15 s), the time step would have been smaller than the time resolution of the data, and this would have introduced unnecessary and redundant computations. A step size of 20 s assures that every increment corresponds to adding at least one data point to the computations. The best result for CP is obtained when  $\tau_1 = 7.33$  min and  $\tau_2 = 2$  min, corresponding to a minimum in  $|\Delta t_{\text{CP}}|$  of  $\sim 35$  s. We see that good accuracy (values of  $|\Delta t_{\text{CP}}|$  smaller than 2 min) corresponds to fairly small values of  $\theta_{\text{CP}}$  and relatively large values of the quality factor  $\phi$ . Figure 3 shows that, in the case of this discontinuity, values of  $\theta_{\text{CP}}$  larger than about  $55^\circ$  and  $\phi$  smaller than  $115^\circ$  correspond to large values of  $|\Delta t_{\text{CP}}|$ , i.e., small accuracy of time delay estimation.

[24] Figure 3 also presents the results for  $\Delta t_{\text{MVAB}}$  ( $\Delta t_{\text{MVAB0}}$ ),  $\theta_{\text{MVAB}}$  ( $\theta_{\text{MVAB0}}$ ), and  $EvR$  ( $EvR0$ ) as a function of  $\tau_3$  ( $\tau_4$ ). The best results are obtained for  $\tau_3 = \tau_4 = 2.33$  min, which give a minimum  $|\Delta t|$  of  $\sim 30$  s. The sharp separation in MVAB between accurate time delay predictions for values of  $\tau_3 \leq 6$  min and highly inaccurate ones for  $\tau_3 > 6$  min

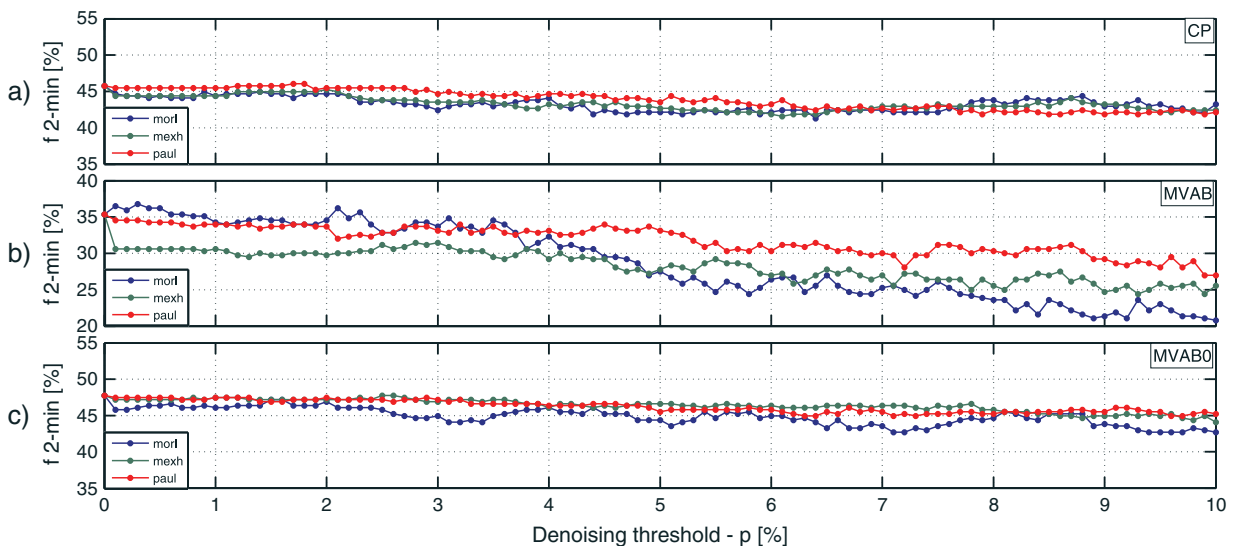


**Figure 7.**  $f_{2\text{-min}}$  for the three time delay estimation methods as a function of threshold amplitude level for (a) CP, (b) MVAB, and (c) MVAB0. The method parameters used in the calculations are  $\tau_1^m$ ,  $\tau_2^m$ ,  $\tau_3^m$ , and  $\tau_4^m$ . The blue, green, and red lines indicate the wavelet functions Morlet, Mexican Hat, and Paul, respectively.

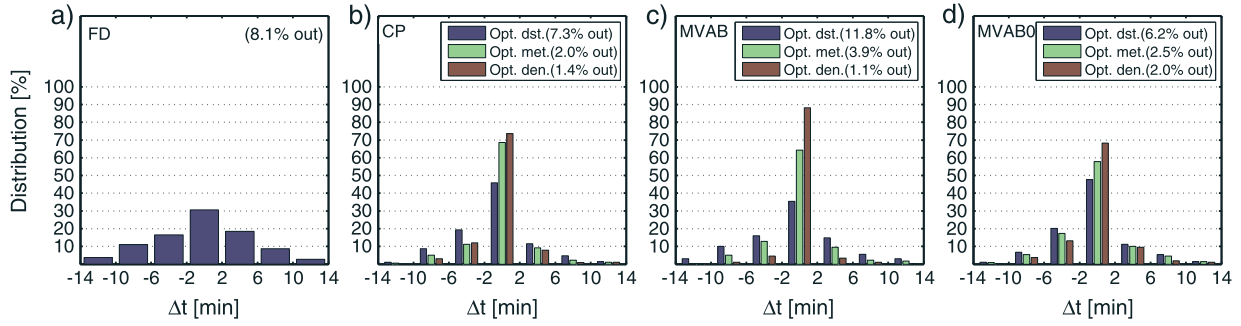


**Figure 8.** Distributions of time delay accuracy  $\Delta t$  for (b) CP, (c) MVAB, and (d) MVAB0 obtained using the method parameters that maximize the 2 min fractions presented in Figure 6 (Opt. dst., blue bins), the individually optimized method parameters (Opt. met., green bins), and the individually optimized denoising parameters (Opt. den., red bins). Also shown is the (a) histogram of time delay accuracy obtained with the FD method. The percentage of discontinuities outside the  $\pm 14$  min interval for  $\Delta t$  are shown in the top right corner for each method.

is due to the rapid decrease in the  $B_x$  component around 17:57 UT, which is included in estimates using  $\tau_3 > 6$  min. MVAB0 is much less influenced by the presence of the sharp decrease in  $B_x$ , leading to a more smooth dependence of  $\Delta t_{MVAB0}$  and  $\theta_{MVAB0}$  on  $\tau_4$ . Using values larger than 6 min for the parameter  $\tau_3$ , the quality factor  $\theta_{MVAB}$  increases abruptly to values larger than  $80^\circ$ , and  $EvR_{MVAB}$  decreases to values smaller than 2. This shows that, in the case of this discontinuity, poor time delay accuracy corresponds to large values of  $\theta_{MVAB}$  and small values for  $EvR_{MVAB}$ .

[25] Figure 4 shows the denoised magnetic field superimposed on the original time series for the three wavelet functions mentioned in the previous section and two threshold levels,  $p = 2$  and  $p = 10$ . We see that the threshold level has a more important effect on the results than the wavelet function (see also Figure 7). We also see that denoising with  $p = 10$ , for all wavelet bases, removes the sharp decrease in  $B_x$  (at 17:57 UT) responsible for the erroneous time delays obtained using  $\tau_3 > 6$  min.

[26] Figure 5 shows an analysis similar to the one presented in Figure 3 using the denoised time series presented in Figure 4d (Morlet wavelet function and threshold level  $p = 10$ ). While denoising leaves the results of CP and MVAB0 largely unchanged, the MVAB results are significantly improved. The MVAB method applied on denoised data predicts now a correct time delay (with an accuracy within  $\pm 2$  min) for all values of the parameter  $\tau_3$  between 2 to 10 min. Denoising also increases the eigenvalue ratio  $EvR_{MVAB}$ , thus allowing the use of increased lower limits for this quality factor, resulting in a better overall data quality.

## 6. Statistical Results

[27] Figure 6 shows how the fraction of discontinuities with accurate time delay estimation (i.e., within  $\pm 2$  min, indicated as  $f_{2-\text{min}}$ ) varies as a function of method parameters, for each of the three methods. The  $f_{2-\text{min}}$  were computed with  $\tau_1$ ,  $\tau_2$ ,  $\tau_3$ , and  $\tau_4$  ranging from 2 to 10 min with the

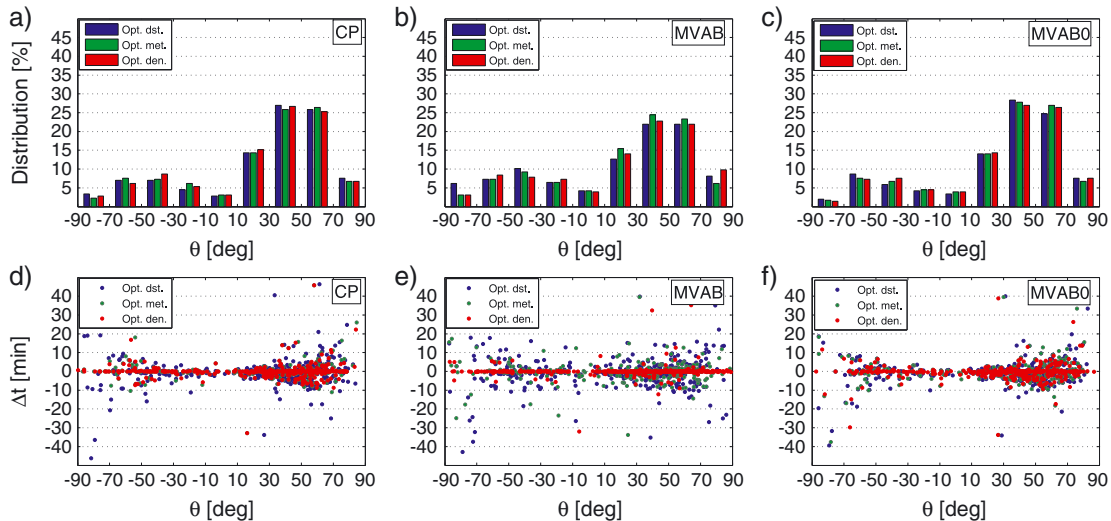


**Figure 9.** Illustration of the influence of wavelet denoising on the orientation angle  $\theta$ . (top) Histograms of  $\theta$  angles for (a) CP, (b) MVAB, and (c) MVAB0. (bottom) Time delay accuracy  $\Delta t$  as a function of  $\theta$  for (d) CP, (e) MVAB, and (f) MVAB0. Blue, green, and red colors have the same meaning as in Figure 8.

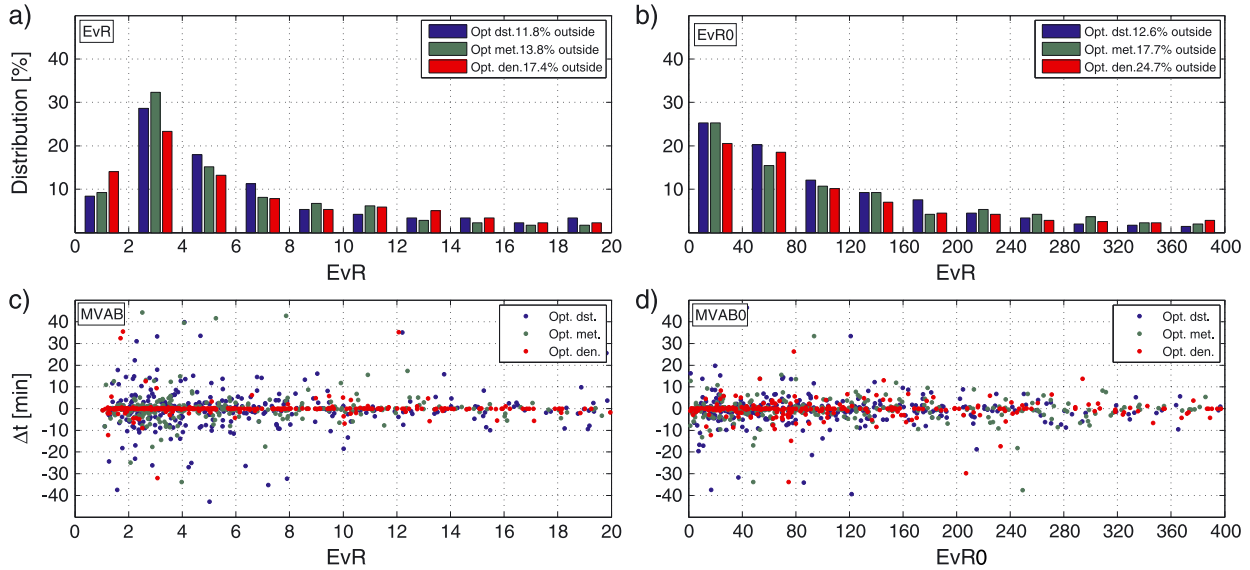


**Figure 10.** Illustration of the influence of wavelet denoising on the eigenvalue ratios EvR and EvR0, computed with MVAB and MVAB0, respectively. (top) Histograms of (left) EvR and (right) EvR0. (bottom) Time delay accuracy  $\Delta t$  as a function of (left) EvR and (right) EvR0. Blue, green, and red colors have the same meaning as in Figure 8.

same time step as described in the previous section (20 s). The parameters that maximize  $f_{2-\min}$  are  $\tau_1^m = 2$  min,  $\tau_2^m = 4$  min,  $\tau_3^m = 5.33$  min, and  $\tau_4^m = 8.33$  min. Using this set of parameters, 45% of discontinuities are estimated within  $\pm 2$  min from the observed times for CP, 35.5% for MVAB and 47.5% for MVAB0. The accuracy of time delay estimation improves when a shorter  $\tau_1$  is used in CP, decreases when increasing  $\tau_3$  in MVAB, and is relatively constant when varying  $\tau_4$  for MVAB0. In each case we obtain only modest fractions of accurate time delay estimations (below 50%) regardless of the set of parameters used. A similar optimization procedure was used by *Weimer and King* [2008] to determine the optimum set of parameters for CP and MVAB0. They found that the best results are obtained if  $\tau_1 = 0$  min,  $\tau_2 = 2.13$  min, and  $\tau_4 = 6.66$  min and that the estimation accuracies are relatively equal for the two methods. *Mailyan et al.* [2008] used the set of parameters:  $\tau_1 = 7$  min,  $\tau_2 = 2.66$  min, and  $\tau_3 = \tau_4 = 7$  min and determined that the best results are obtained with the MVAB0 method.

[28] Figure 7 depicts the  $f_{2-\min}$  computed with  $\tau_1^m$ ,  $\tau_2^m$ ,  $\tau_3^m$ , and  $\tau_4^m$  and different wavelet functions as a function of denoising threshold level  $p$ . The wavelet functions tested are Morlet (blue), Mexican Hat (green), and Paul (red line); the threshold level  $p$  is varied from 0 to 10, with a step size of 0.1. For example, the first point of the green line in Figure 7a represents the  $f_{2-\min}$  computed using  $\tau_1^m$  and  $\tau_2^m$  in the CP method for all discontinuities, the second point is computed by first denoising the time series used as input in CP with the Mexican Hat wavelet and a threshold  $p = 0.1$  and then calculating  $f_{2-\min}$  as above, the third point is computed with a threshold  $p = 0.2$ , and so on. Figure 7 shows that the three methods are quite stable to small values of  $p$ , but a clear decreasing trend is seen as  $p$  increases. For CP and MVAB0 the decreasing trend is reduced compared with the MVAB method, and also the variability of  $f_{2-\min}$  is slightly

lower for CP and MVAB0. A notable result is obtained for MVAB using the Morlet wavelet, where we see that up to  $p \approx 3$ ,  $f_{2-\min}$  is clearly above the values corresponding to the other two wavelet functions; between  $p = 3$  and  $p = 5$  the values of  $f_{2-\min}$  are comparable, and above  $p = 5$  the values obtained with MVAB are lower than the ones for the other two wavelet functions. This effect may be due to the lower temporal resolution of the Morlet wavelets that are able to filter out more efficiently the high-frequency fluctuations, leading thus to the smearing out of the sharp discontinuities. Figure 7 also shows that by using the same set of denoising parameters for all discontinuities, the fraction of accurate time delay estimations shows only a very small increase for small values of the threshold parameter  $p$ , if at all.

[29] In order to calculate the optimum parameters of the boundary normal estimation methods for each event individually, we varied  $\tau_1$ ,  $\tau_2$ ,  $\tau_3$ , and  $\tau_4$  from 2 to 10 min, with a step size of 20 s, and determined those values that minimize the time delay accuracy  $|\Delta t|$  (as in Figure 3). Figure 8 shows the distribution of  $\Delta t$  for each method in the case of optimized method parameters (Opt. met., indicated as green bins). It is clear that the percentages of accurate time delay estimations are significantly improved. As a matter of fact,  $f_{2-\min}$  increased up to 69% for CP, 65% for MVAB, and 59% for MVAB0.

[30] Then we determined the optimum set of denoising parameters for each discontinuity individually. The optimization procedure is similar to the one applied to optimize the method parameters. To optimize the set of denoising parameters, we use the optimum method parameters for each discontinuity and then compute the time delays for different denoising parameters. The optimum set of denoising parameters is the one that maximizes the prediction accuracy. The distributions of  $\Delta t$  in this case are presented in Figure 8 as red bins indicated as “Opt. den.” and clearly show that the  $f_{2-\min}$  increases up to 74% for CP, 88% for MVAB, and

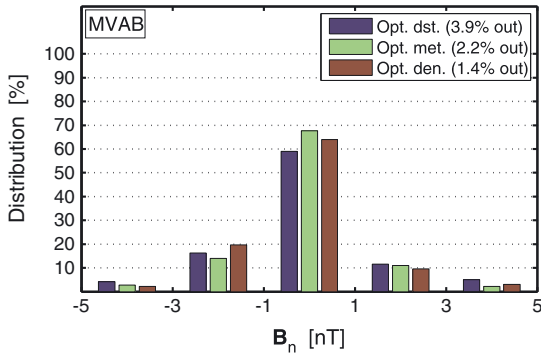


**Figure 11.** Illustration of the influence of wavelet denoising on the mean magnetic field along the boundary normal,  $B_n$ , computed with MVAB. (top right corner) The percentage of discontinuities with  $B_n$  outside the  $\pm 5$  nT interval. Blue, green, and red colors have the same meaning as in Figure 8.

69% for MVAB0. The rather small improvement for CP was expected since a high accuracy was already obtained by individually optimizing the method parameters. In the case of MVAB0 the wavelet denoising increases the 2 min fraction, but a relatively large number of discontinuities still remain outside the  $\pm 2$  min interval. The main result in Figure 8 is the improvement in the case of individually optimized denoising parameters for MVAB, for which almost 99% of discontinuities are now estimated with an accuracy within  $\pm 6$  min. Figure 8 also shows the results obtained with the fixed set of parameters that maximize  $f_{2-\min}$  (indicated as Opt. dst.) inferred from the results of Figure 6 ( $\tau_1^m$ ,  $\tau_2^m$ ,  $\tau_3^m$ , and  $\tau_4^m$ ). We see that  $f_{2-\min}$  for MVAB obtained using individually optimized denoising parameters is more than 50% larger than the corresponding fraction obtained with the fixed set of parameters above.

[31] Figure 8a illustrates the results obtained with the FD method. As expected, the prediction accuracy of FD is rather poor compared with the other three methods, and only 30% of events are predicted with a time delay accuracy  $\Delta t$  within  $\pm 2$  min.

[32] We also studied the influence of wavelet denoising on the statistics of discontinuity orientation for the three methods. The results are presented in Figure 9. We have already seen in Figures 3 and 5 that the orientation angles  $\theta$  are influenced by denoising for individual cases, but we now see that the distribution is not significantly affected. The time delay estimation accuracy for MVAB is improved by denoising without significantly modifying the distribution of  $\theta$  angles. This shows that time delay can be accurately estimated using the MVAB method if a proper preliminary denoising is performed, even if the plane of the discontinuity is almost parallel to the Sun-Earth line ( $\theta$  angles close to  $\pm 90^\circ$ ). In the case of CP and MVAB0 methods, we see a large scatter in timing accuracy for values of  $\theta$  larger than  $\sim 50^\circ$ , even for the optimum denoising case. This means that discontinuities with large  $\theta$  angles are predicted less accurately than the ones with small angles. A similar result was reported in *Mailyan et al.* [2008], which concluded that an acceptable maximum value for  $\theta$ , for an accurate normal estimation, is  $70^\circ$ .

[33] We studied also the influence of wavelet denoising on the statistics of field rotation angles  $\phi$  calculated with the CP method. The denoising procedure has no significant influence on the distribution of  $\phi$  angles, so we decided not to show it.

[34] Figure 10 presents the influence of wavelet denoising on the eigenvalue ratios for MVAB and MVAB0. The EvR distribution is not significantly affected by denoising, and the time delay accuracy is improved irrespective of the EvR value, contrary to the other two cases (Opt. dst. and Opt. met.) where better results are obtained for eigenvalue ratios above  $\sim 8$ . The EvR0 distributions show that the number of discontinuities with EvR0 larger than 400 is doubled after denoising, compared with the results obtained for Opt. dst. We see that the time delay accuracy is improved after denoising irrespective of EvR0.

[35] We also studied the influence of wavelet denoising on the mean magnetic field along the boundary normal computed with MVAB. The results are presented in Figure 11. Using the parameter  $\tau_3^m$ , we find that 59% of discontinuities are estimated to have a  $B_n$  component in the  $\pm 1$  nT interval and 3.9% are outside the  $\pm 5$  nT interval. Using the individually optimized method parameters (Opt. met.), we find that 68% are now in the  $\pm 1$  nT interval and only 2.2% are outside the  $\pm 5$  nT interval. For the individually optimized denoising parameters (Opt. den.), 64% are in the  $\pm 1$  nT interval and only 1.4% are outside the  $\pm 5$  nT interval. These results show that even before denoising the majority of discontinuities in our database had a very small normal component of the magnetic field and denoising only slightly increases this number. The small normal component of the magnetic field indicates that most of the discontinuities in our database resemble tangential discontinuities.

## 7. Summary and Conclusions

[36] We have presented a statistical analysis of the performance of three methods (CP, MVAB, and MVAB0) to compute the propagation delay of solar wind discontinuities and the influence of wavelet denoising on this performance. We analyzed 356 discontinuities observed by both ACE, located at L1, and C3, close to the Earth's bow shock, between 2001 and 2012.

[37] We found that by using the fixed set of parameters  $\tau_1^m = 2$  min,  $\tau_2^m = 4$  min,  $\tau_3^m = 5.33$  min, and  $\tau_4^m = 8.33$  min, the fraction of discontinuities estimated to arrive at C3 within  $\pm 2$  min from the observed time delay ( $f_{2-\min}$ ) is 45% for CP, 35.5% for MVAB, and 47.5% for the MVAB0 method. These results are in good agreement with the study by *Mailyan et al.* [2008], which also found that the best method to obtain accurate propagation delays for solar wind discontinuities is MVAB0. By tuning the method parameters for each discontinuity individually, we can determine the optimum set of method parameters. We found that  $f_{2-\min}$  increases significantly, up to 69% for CP, 65% for MVAB, and 58% for MVAB0.

[38] Wavelet denoising was used to remove small-scale fluctuations from magnetic measurements, which are known to influence the estimation of the orientation of a discontinuity, thus affecting the time delay estimation. We found that by using a fixed set of denoising parameters for the entire database of discontinuities we obtain only very small

increases of  $f_{2-\min}$ , if any. By determining the optimum set of denoising parameters for each discontinuity individually, we found that  $f_{2-\min}$  increases significantly, up to 74% for CP, 88% for MVAB, and 69% for MVAB0. The fact that MVAB is the most precise method demonstrates that it is more sensitive to small-scale fluctuations than CP or MVAB0, and, by denoising the input signal, we can improve significantly the accuracy of time delay estimation.

[39] When the denoising is applied with a fixed set of parameters, it does not have a significant impact on the statistics of the time delays of solar wind discontinuities in our database. Nevertheless, the denoising has a clear positive effect when applied on variable time intervals as demonstrated by the results obtained for the case study presented in section 5 and by the individually optimized denoising results presented in Figure 8. The case study shows that denoising improves the accuracy of discontinuity determination and allows for an increased eigenvalue ratio threshold, resulting in better overall data quality and the inclusion of a large number of events that originally did not meet the quality criteria, thus improving the statistics.

[40] **Acknowledgments.** The research leading to these results has received funding from the ESA PECS Project KEEV (97049) and from the European Community's Seventh Framework Programme (FP7/2007–2013) under grant agreement 313038 (STORM). C.M. acknowledges the financial support by the Romanian Ministry of Science and Research and by the Wallonie-Bruxelles International through a bilateral collaboration project (593) between the Institute of Space Science (Romania) and the Catholic University of Louvain, and by the Academy of Finland through the HISSI research project 128189. We acknowledge the use of the AMDA science analysis system provided by the Centre de Données de la Physique des Plasmas (CESR, Université Paul Sabatier, Toulouse).

[41] Philippa Browning thanks the reviewers for their assistance in evaluating this paper.

## References

- Balogh, A., et al. (2001), The Cluster Magnetic Field Investigation: Overview of in-flight performance and initial results, *Ann. Geophys.*, *19*, 1207–1217, doi:10.5194/angeo-19-1207-2001.
- Burgess, D., E. Mobius, and M. Scholer (2012), Ion acceleration at the Earth's bow shock, *Space Sci. Rev.*, *173*, 5–47, doi:10.1007/s11214-012-9901-5.
- Colburn, D. S., and C. P. Sonett (1966), Discontinuities in the solar wind, *Space Sci. Rev.*, *5*, 439–506, doi:10.1007/BF00240575.
- Daubechies, I. (1992), *Ten Lectures on Wavelets*, 377 p., Cbms-Nsf Regional Conference Series in Applied Mathematics, Society for Industrial and Applied Mathematics, Philadelphia, PA, USA.
- De Moortel, I., S. Munday, and A. Hood (2004), Wavelet analysis: The effect of varying basic wavelet parameters, *Sol. Phys.*, *222*, 203–228, doi:10.1023/B:SOLA.0000043578.01201.2d.
- Donoho, D., and I. M. Johnstone (1995), Adapting to unknown smoothness via wavelet shrinkage, *J. Am. Stat. Assoc.*, *90*, 1200–1224.
- Donoho, D. L. (1995), De-noising by soft-thresholding, *IEEE Trans. Inf. Theor.*, *41*(3), 613–627, doi:10.1109/18.382009.
- Donoho, D. L., I. M. Johnstone, G. Kerkycharian, and D. Picard (1995), Wavelet shrinkage: Asymptopia, *J. Roy. Stat. Soc. B*, *57*, 301–369.
- Gosling, J. T., J. R. Asbridge, S. J. Bame, G. Paschmann, and N. Sckopke (1978), Observations of two distinct populations of bow shock ions in the upstream solar wind, *Geophys. Res. Lett.*, *5*, 957–960, doi:10.1029/GL005i011p00957.
- Haaland, S., and G. Paschmann (2001), Improved boundary normal calculations using minimum variance analysis and wavelet de-noising techniques, in *Proceedings of Les Woolliscroft Memorial Conference*, vol. 492, edited by B. Warmbein, *Eur. Space Agency Spec. Publ.*, pp. 127–132.
- Haaland, S., C. Munteanu, and B. Mailyan (2010), Solar wind propagation delay: Comment on “Minimum variance analysis-based propagation of the solar wind observations: Application to real-time global magnetohydrodynamic simulations” by A. Pulkkinen and L. Raststatter, *Space Weather*, *8*, S06005, doi:10.1029/2009SW000542.
- Horbury, T. S., D. Burgess, M. Fränz, and C. J. Owen (2001), Three spacecraft observations of solar wind discontinuities, *Geophys. Res. Lett.*, *28*, 677–680, doi:10.1029/2000GL000121.
- Jacquey, C., et al. (2010), AMDA, Automated Multi-Dataset Analysis: A web-based service provided by the CDPP, in *The Cluster Active Archive, Studying the Earth's Space Plasma Environment*, edited by H. Laakso et al., 239–247, Springer, Berlin, doi:10.1007/978-90-481-3499-1-16.
- Knetter, T. (2005), A new perspective of the solar wind micro-structure due to multi-point observations of discontinuities, Ph.D. thesis, Universitat zu Koln.
- Mailyan, B., C. Munteanu, and S. Haaland (2008), What is the best method to calculate the solar wind propagation delay? *Ann. Geophys.*, *26*, 2383–2394, doi:10.5194/angeo-26-2383-2008.
- McComas, D. J., S. J. Bame, P. Barker, W. C. Feldman, J. L. Phillips, P. Riley, and J. W. Griffiee (1998), Solar Wind Electron Proton Alpha Monitor (SWEPAM) for the advanced composition explorer, *Space Sci. Rev.*, *86*, 563–612, doi:10.1023/A:1005040232597.
- Paschmann, G., N. Sckopke, I. Papamastorakis, J. R. Asbridge, S. J. Bame, and J. T. Gosling (1981), Characteristics of reflected and diffuse ions upstream from the Earth's bow shock, *J. Geophys. Res.*, *86*, 4355–4364, doi:10.1029/JA086iA06p04355.
- Pulkkinen, A., and L. Rastätter (2009), Minimum variance analysis-based propagation of the solar wind observations: Application to real-time global magnetohydrodynamic simulations, *Space Weather*, *7*, S12001, doi:10.1029/2009SW000468.
- Rème, H., et al. (2001), First multispacecraft ion measurements in and near the Earth's magnetosphere with the identical Cluster Ion Spectrometry (CIS) experiment, *Ann. Geophys.*, *19*, 1303–1354, doi:10.5194/angeo-19-1303-2001.
- Smith, C. W., J. L'Heureux, N. F. Ness, M. H. Acuña, L. F. Burlaga, and J. Scheifele (1998), The ACE magnetic fields experiment, *Space Sci. Rev.*, *86*, 613–632, doi:10.1023/A:1005092216668.
- Sonnerup, B. U. Ö., and M. Scheible (1998), Minimum and maximum variance analysis, in *Analysis Methods for Multi-spacecraft Data*, edited by G. Paschmann and P. W. Daly, chap. 8, pp. 185–220, SR-001 in ISSI Scientific Reports Series, ESA/ISSI, ESA Publ. Div., Noordwijk, Netherlands.
- Torrence, C., and G. P. Compo (1998), A practical guide to wavelet analysis, *Bull. Am. Meteorol. Soc.*, *79*, 61–78, doi:10.1175/1520-0477(1998)079<0061:APGTWA>2.0.CO;2.
- Weimer, D. R., and J. H. King (2008), Improved calculations of interplanetary magnetic field phase front angles and propagation time delays, *J. Geophys. Res.*, *113*, A01105, doi:10.1029/2007JA012452.

# Paper IV



## INERTIAL RANGE TURBULENCE OF FAST AND SLOW SOLAR WIND AT 0.72 AU AND SOLAR MINIMUM

ELIZA TEODORESCU<sup>1</sup>, MARIUS ECHIM<sup>1,2</sup>, COSTEL MUNTEANU<sup>1,6,7</sup>, TIELONG ZHANG<sup>3</sup>, ROBERTO BRUNO<sup>4</sup>, AND PETER KOVACS<sup>5</sup><sup>1</sup>Institute for Space Sciences, Măgurele, Romania; eliteo@spacescience.ro<sup>2</sup>Belgian Institute for Space Aeronomy, Bruxelles, Belgium<sup>3</sup>Space Research Institute, Graz, Austria<sup>4</sup>INAF-IAPS, Istituto di Astrofizica e Planetologia Spaziali, Rome, Italy<sup>5</sup>Geological and Geophysical Institute of Hungary, Budapest, Hungary<sup>6</sup>University of Bucharest, Măgurele, Romania<sup>7</sup>University of Oulu, Oulu, Finland

Received 2015 February 20; accepted 2015 April 22; published 2015 May 11

## ABSTRACT

We investigate *Venus Express* observations of magnetic field fluctuations performed systematically in the solar wind at 0.72 Astronomical Units (AU), between 2007 and 2009, during the deep minimum of solar cycle 24. The power spectral densities (PSDs) of the magnetic field components have been computed for time intervals that satisfy the data integrity criteria and have been grouped according to the type of wind, fast and slow, defined for speeds larger and smaller, respectively, than  $450 \text{ km s}^{-1}$ . The PSDs show higher levels of power for the fast wind than for the slow. The spectral slopes estimated for all PSDs in the frequency range 0.005–0.1 Hz exhibit a normal distribution. The average value of the trace of the spectral matrix is  $-1.60$  for fast solar wind and  $-1.65$  for slow wind. Compared to the corresponding average slopes at 1 AU, the PSDs are shallower at 0.72 AU for slow wind conditions suggesting a steepening of the solar wind spectra between Venus and Earth. No significant time variation trend is observed for the spectral behavior of both the slow and fast wind.

*Key words:* interplanetary medium – magnetic fields – plasmas – solar wind – turbulence

## 1. INTRODUCTION

The spectral properties of the magnetic field and plasma fluctuations in the solar wind have been investigated in situ over several decades for a broad range of frequencies and various radial distances. It has been found that the power spectral density (PSD) of magnetic field fluctuations exhibits three different power-law regimes,  $P(k) = P_0 k^{-\alpha}$ , characterized by different exponents: (i)  $\alpha \approx -1$  for smaller  $k$  (e.g., Matthaeus & Goldstein 1986; Verdini et al. 2012); (ii)  $\alpha \approx -5/3$  for the intermediate  $k$  (e.g., Marsch & Tu 1990), this range of  $k$  is also anisotropic and the fluctuations parallel and perpendicular to the magnetic field may exhibit a different power-law index (see, e.g., Dasso et al. 2005; Horbury et al. 2012); and (iii)  $\alpha \leq -2.5$  with a minimum index close to  $-4.5$  (Leamon et al. 1999; Bruno et al. 2014) for the largest  $k$  (see, also, Coleman 1968; Stawicki et al. 2001, and Bruno & Carbone 2013; Alexandrova et al. 2013, for a review). Frisch (1995) described the three characteristic power-law regimes, separated by spectral breaks, as the magnetohydrodynamic equivalents of the scale ranges of classical hydrodynamic turbulence: (i) the driving (or energy containing) range; (ii) the inertial range, dominated by nonlinear turbulent interactions which transfer the energy over multi-scales; and (iii) the dissipation range. The physical processes contributing to dissipation in turbulent collisionless plasmas are still an open issue and in recent years it has been argued (see, e.g., Alexandrova et al. 2013) that below proton scales, another turbulent cascade may take place which is described by a different power law. This is followed by an exponential law which could be indicative of dissipation.

In practice, the analysis of an in situ time series provides PSD as a function of frequency in the spacecraft reference frame,  $P(f_{\text{sat}})$ , which would correspond to the Doppler-shifted wavevector spectra,  $P(k)$ , under the assumption that the plasma flows over the spacecraft much faster than the characteristic

time evolution of the nonlinearly interacting turbulent spatial structures/eddies (the Taylor hypothesis). In the solar wind, the transition between the driving and inertial ranges is generally observed at frequencies between  $10^{-4}$  and  $10^{-3}$  Hz which would correspond to spatial scales related to the solar wind correlation/integral length ( $\lambda$ ) or the typical size of the “energy containing eddies” (Batchelor 1970; Matthaeus et al. 1994). The high-frequency limit of the inertial range in the solar wind and the transition to the kinetic regime is marked by a break in the spacecraft-frame frequency representation, generally in the vicinity of spatial scales (under the Taylor hypothesis) of the order of the proton inertial length or the proton Larmor radius (e.g., Chen et al. 2014). Recently, the variation of this break with heliocentric distance was discussed by Bruno & Trenchi (2014). High-resolution data seem to suggest that dissipation may effectively start at higher frequencies corresponding to the electron Larmor radius (Alexandrova et al. 2009). The solar wind is a supersonic and super-Alfvénic tenuous stream of collisionless plasma emerging from the dynamic solar corona, and therefore discerning “pure” turbulence features from other structures convected from the Sun is still an issue (see, for instance, Tu & Marsch 1995; Bruno et al. 2007; Borovsky 2008).

Solar wind observations in the inner heliosphere (between 0.3 and 0.9 AU) suggest that the ordering parameter of turbulent properties is the “age” of the turbulence, evaluated as the time it takes for the solar wind to travel from the Sun to the spacecraft, rather than the radial distance. The “aging” of the solar wind turbulence is also characterized by a progressive spectral dominance of the “2D” mode of the turbulence (characterized mainly by perpendicular wavevectors) over the “slab” mode (dominated mainly by parallel wavevectors; Ruiz et al. 2011). Analyses based on a global mean magnetic field estimate concluded that the slow wind generally exhibits features of “2D” turbulence, while the turbulence in the fast

wind is more of the “slab” type (Dasso et al. 2005; Weygand et al. 2011) and the anisotropic state found near the Sun evolves toward a more isotropic state at 1 AU. On the other hand, approaches exploring anisotropy through the scale-dependent local mean magnetic field (e.g., Horbury et al. 2008; Podesta 2009; Wicks et al. 2010; Forman et al. 2011) indicate that the high-speed solar wind power spectrum is dominated by perpendicular “2D” fluctuations. Simulation results (Chen et al. 2011) show the same discrepancy between the global and local mean magnetic field approaches and the authors conclude that global mean magnetic field scaling is not able to properly discriminate between parallel and perpendicular fluctuations. Smith (2003) shows that at high latitudes, roughly equal proportions of slab (1D) and 2D coexist in the same plasma element.

At solar minimum, the solar wind is characterized by an increased recurrence of high-speed streams (up to  $800 \text{ km s}^{-1}$  and more) with lower density and higher temperature, whose origin is the meridional extensions of the polar coronal holes. The properties of fast and slow wind turbulence were investigated for different phases of the solar cycle from data recorded by *Helios* (Bavassano & Bruno 1989, 1991; Ruiz et al. 2011), *ACE* (Borovsky 2012b), *Ulysses* (Yordanova et al. 2009), *Cluster*, *THEMIS* (Weygand et al. 2011), *Messenger*, and *Wind* (Bruno & Trenchi 2014; Bruno et al. 2014). Observations of the solar wind by *Ulysses* at larger radial distances (between 1.5 and 5.4 AU), outside the ecliptic and close to the solar minimum, show that the spectral index of the fast wind inertial range turbulence presents values in the range  $-1.79 < \alpha < -1.55$  for the magnetic field components, and between  $-1.52 < \alpha < -1.25$  for the total field,  $|B|$ . The spectra of the slow wind exhibit similar power-law behavior but with steeper slopes,  $-1.95 < \alpha < -1.45$  for the components of the magnetic field and  $-1.78 < \alpha < -1.55$  for the total field (Yordanova et al. 2009). It is unclear whether or not the inertial range spans roughly the same frequency range for the fast and slow wind.

In situ observations at 1 AU indicate that the *median* of the magnetic spectral index in the inertial range depends on the type of wind: it is shallower for the fast wind ( $V_{\text{wind}} > 450 \text{ km s}^{-1}$ ),  $\bar{\alpha} = -1.54$ , compared to the slow wind,  $\bar{\alpha} = -1.70$ , as shown by Borovsky (2012a) from 10 years of *ACE* data (1998–2008). The spectral index may assume “extreme” values, larger than  $-1.33$  and smaller than  $-1.95$ . Steeper spectral slopes are observed at 1 AU when the solar wind density is larger, the temperature is smaller, the speed takes on lower values, and the number of strong directional discontinuities is reduced (Borovsky 2012a). Close to the high-frequency limit of the inertial range, at proton scales, in the vicinity of the fluid/kinetic spectral break, *Wind* (at 0.99 AU) and *Messenger* (at 0.42 AU) data show that the spectral slope may depend on the power density in the inertial range: steeper slopes are observed for larger power in the inertial subrange (Bruno et al. 2014). This frequency break moves toward smaller frequencies as the radial distance increases (Bruno & Trenchi 2014).

## 2. SPECTRAL PROPERTIES OF FAST AND SLOW SOLAR WIND AT 0.72 AU

We analyze data recorded by *Venus Express* (*VEX*) in the solar wind in the vicinity of Venus, at 0.72 AU, between 2007 January and 2009 December, during the minimum of solar

cycle 24. Since Venus has no intrinsic magnetic field, its induced magnetosphere is confined to shorter distances from the planet, and thus *VEX* spends more than 20 hr each day of the year in the solar wind. Thus, *VEX* is a unique solar wind monitor which investigates the inner heliospheric solar wind on a day to day basis for almost one solar cycle, since 2006. The turbulent fluctuations of the solar wind magnetic field considered in this study are provided by the *VEX* Magnetometer (*VEX-MAG*; Zhang et al. 2006) with a cadence of 1 Hz. The data are obtained through an offline calibration procedure by downsampling the 32 Hz resolution data.

The plasma state (electron and ion spectra and their moments, e.g., density, temperature, velocity) is investigated using the Analyzer of Space Plasma and Energetic Atoms (*ASPERA*, Barabash et al. 2007). *ASPERA* operates in the solar wind for short time intervals of the order of one to two hours, close to the orbit apogee. The ion and electron spectra and their moments are provided with a time resolution of 196 seconds which does not allow for a spectral analysis of the solar wind plasma parameters. Nevertheless, the estimate of the moments of the ion velocity distribution function provides us with the data we need to select high and low speed solar wind. Inspired by previous studies, we select the slow and fast wind intervals based on a threshold speed value equal to  $450 \text{ km s}^{-1}$ . The magnetic field experiment operates continuously, however, we consider time intervals of roughly four hours, which are close to the *VEX* apogee and include those time periods when *ASPERA* is also operating.

Several quality checks impose additional constraints on the magnetic field data analysis. We disregard the time intervals shorter than 1 hr and those with data gaps exceeding 30 consecutive points. In general, the total missing data points amount to less than 3% of the total number of samples for the selected time intervals and they appear to be randomly distributed over time. Thus, the number of data gaps in the selected time intervals is small and their lengths are short. A linear interpolation is applied prior to the spectral analysis. From a total of 1094 orbits between 2007 January and 2009 December, only 204 time intervals fulfill the data quality requirements, 48 of which correspond to fast solar wind observations ( $V_{\text{wind}} > 450 \text{ km s}^{-1}$ ).

The magnetic field components are provided in the Venus Solar Orbital (VSO) rectangular frame, with the  $O_x$  axis aligned in the Sunward direction and the  $O_z$  axis perpendicular to the ecliptic plane in the northward direction. The PSDs are computed with a Welch algorithm (Welch 1967) averaging periodograms applied on  $B_x$ ,  $B_y$ ,  $B_z$ , and the total field,  $|B|$ , for all of the selected time intervals. We also compute the trace of the spectral matrix of the fluctuations. A summary plot of all the power spectra is provided in Figure 1; different colors illustrate different types of wind (fast/slow) and different years. An average spectrum is computed as an ensemble average of all the spectra for the fast and slow solar wind, respectively.

The spectral power of the fast solar wind is systematically larger than for the slow wind, as shown by previous results in other locations of the heliosphere (see the review by Bruno & Carbone 2013 and recent results at 0.38 and 1 AU by Bruno et al. 2014). The PSDs exhibit a power-law regime in the frequency range  $[5 \times 10^{-3}, 10^{-1}]$  Hz. A change in the spectral slope is observed around 0.2–0.3 Hz, close to the local Doppler-shifted proton gyrofrequency, followed by a frequency range showing a steepening of the spectra which could

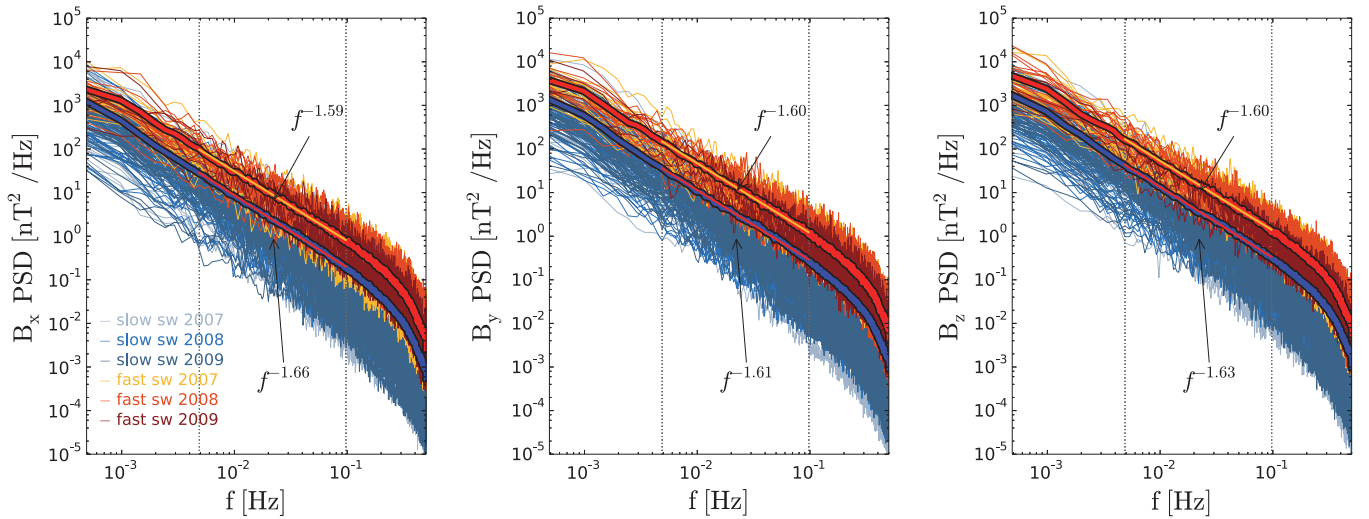


**Figure 1.** Summary plot of the power spectral density spectrum of  $B_x$ ,  $B_y$ , and  $B_z$  from VEX magnetic field data recorded between 2007 and 2009, during the minimum of the 24th solar cycle. Yellow and red lines correspond to fast solar wind, gray and blue lines correspond to slow solar wind. The black dotted lines mark the frequency interval for which the spectral index of each spectrum is computed. An average spectrum is derived as an ensemble average of all the spectra obtained for the fast (the embossed red line) and slow wind (the embossed blue line), respectively. The spectral slope of the average spectra is computed for the frequency range marked by yellow and magenta, respectively.

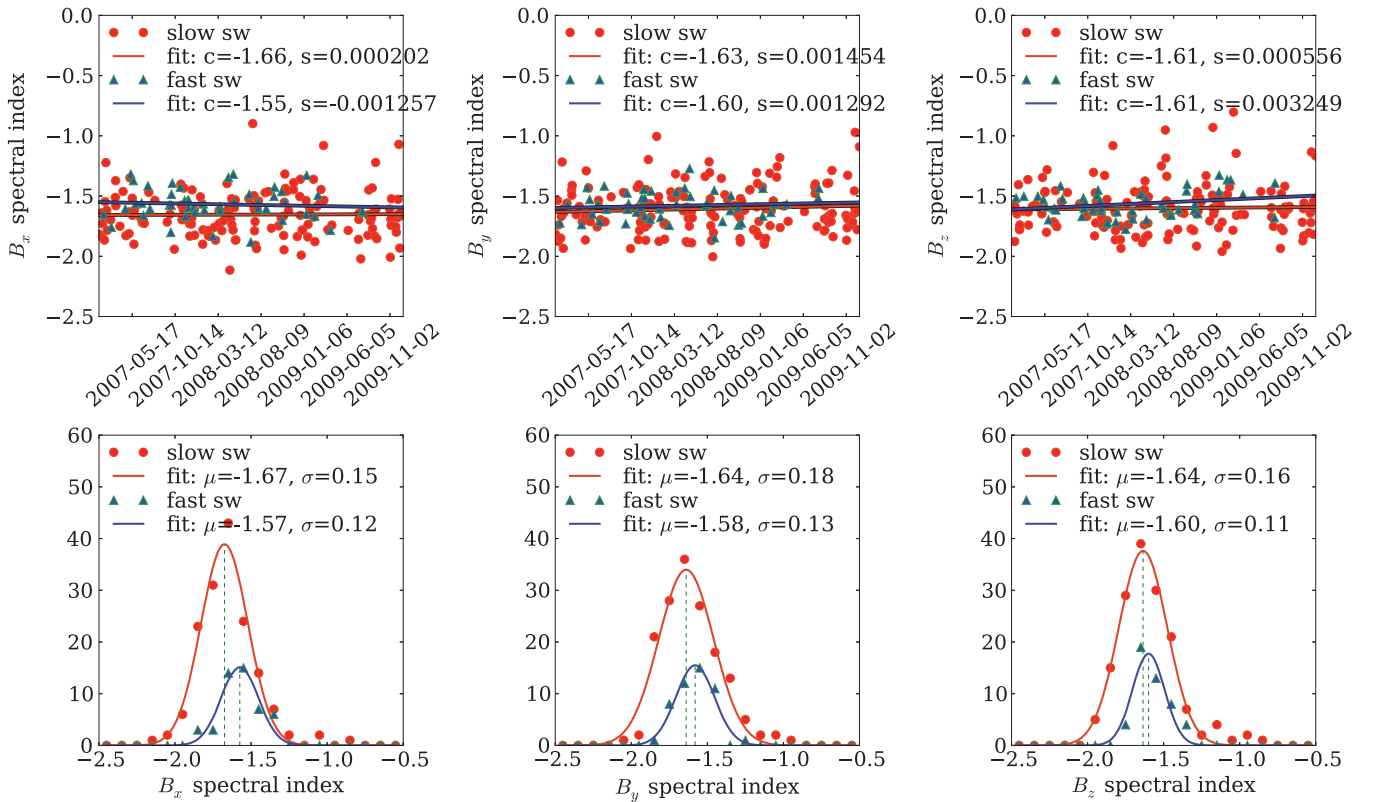


**Figure 2.** Distribution of spectral index for  $B_x$ ,  $B_y$ , and  $B_z$  from data recorded between 2007 and 2009. Upper row: evolution in time of the spectral indices computed in the frequency interval indicated in Figure 1.  $c$  is the constant (intercept) of the first degree polynomial linear fit and  $s$  is the slope of the fit. Lower row: the histogram of the spectral indices approaches a Gaussian distribution with a mean close to  $-5/3$  for the slow wind and  $-1.6$  for the fast wind.

correspond to the lowest frequencies of the non-MHD kinetic turbulent cascade. In order to minimize the effect of inherent uneven sampling of the frequency range by the periodogram technique, the spectral index/slope has been computed from PSDs rebinned and averaged over equal logarithmic bins of frequency. In addition to rebinning the frequency range, we have also searched for power-law behavior by varying the

limits of the fitting frequency range. Thus, for each of the power spectra, the spectral index (or slope) is calculated by a linear least-square fit over the interval  $[5 \times 10^{-3}, 10^{-1}]$  Hz. This range would correspond to the high-frequency part of the inertial subrange at 0.72 AU and solar minimum. The number of data intervals is sufficiently large to allow for a statistical analysis of the distribution of the spectral indices obtained at

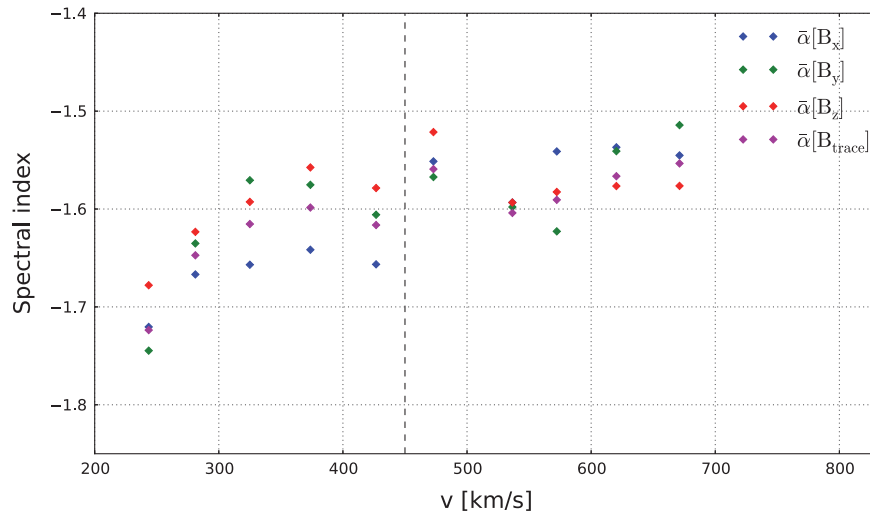


**Figure 3.** Spectral index as a function of solar wind speed; we show averages over velocity bins of  $50 \text{ km s}^{-1}$  width. Different colors illustrate different magnetic field components. Data is collected in the solar wind by VEX between 2007 and 2009. The dotted vertical line represents the threshold we chose to select fast and slow solar wind.

solar minimum, between 2007 and 2009, as illustrated by Figure 2.

The a priori separation of fast from slow solar wind allows for the independent and simultaneous tracking of the evolution of the spectral properties of turbulence for the two types of wind. The least-squares linear fitting of the distributions of the spectral slopes (upper panels of Figure 2) provides experimental evidence that the spectral indices do not exhibit any temporal trends over the years while the solar minimum deepens, both for the slow and fast solar wind. This can be considered as an indication that the processes contributing to the power-law scaling are mainly local, possibly related to nonlinear interactions leading to the turbulent transfer of energy between scales. The histograms of the spectral indices show that the slopes of the magnetic field power spectra in the inertial range fit a Gaussian distribution, as seen in the lower row of plots in Figure 2. The three components of the magnetic field exhibit different average spectral slopes for the fast and slow wind:  $\bar{\alpha}_x^{\text{fast}} = -1.57 \pm 0.02$ ,  $\bar{\alpha}_y^{\text{fast}} = -1.58 \pm 0.02$ , and  $\bar{\alpha}_z^{\text{fast}} = -1.60 \pm 0.02$ , and  $\bar{\alpha}_x^{\text{slow}} = -1.67 \pm 0.01$ ,  $\bar{\alpha}_y^{\text{slow}} = -1.64 \pm 0.01$ ,  $\bar{\alpha}_z^{\text{slow}} = -1.64 \pm 0.01$ , respectively, where  $\bar{\alpha}_i^{\text{fast/slow}}$  indicates the mean spectral index of the component  $i$  and the fast or slow type of wind. The mean spectral index of the trace of the spectral matrix (not shown) varies from  $\bar{\alpha}_B^{\text{fast}} = -1.60 \pm 0.01$  in the fast wind to  $\bar{\alpha}_B^{\text{slow}} = -1.65 \pm 0.01$  in the slow wind.

The variation of the spectral index as a function of the solar wind speed is shown in Figure 3. The average spectral indices of the magnetic field become shallower with increasing plasma velocity, which is in good agreement with previous work (Chen et al. 2013). The continuous trend also seems to indicate that the solar wind velocity may be a controlling parameter for the spectral slope. Nevertheless, recent studies indicate that cross-helicity is equally important in controlling the spectral behavior (Chen et al. 2013).

The VEX results show similarities with the spectral analysis of *Wind* magnetic field data at 1 AU during roughly the same time interval, between 2004 June and 2009 April. Data from *Wind* showed a mean spectral slope from  $-1.6$  (for wind speeds

larger than  $600 \text{ km s}^{-1}$ ) to  $-1.72$  (for speeds smaller than  $400 \text{ km s}^{-1}$ ; Chen et al. 2013). Another analysis of solar wind turbulence at 1 AU, based on *ACE* data recorded between 1998 and 2008, suggests a median spectral slope of the magnetic field equal to  $-1.54$  for speeds larger than  $550 \text{ km s}^{-1}$  and  $-1.70$  for speeds smaller than  $450 \text{ km s}^{-1}$ , respectively (Borovsky 2012a). Nevertheless, the VEX data suggest that, on average, the slopes of the slow wind spectra are shallower at 0.72 AU than at 1 AU, while the fast wind shows, on average, comparable slopes. We note the differences between the mean spectral slopes of the three magnetic field components for the slow wind conditions and roughly the same mean slope for the fast wind. On the other hand, more spectral power is observed for the  $B_y$  and  $B_z$  components in the fast wind. This is in agreement with our expectation of finding more power in the perpendicular components than the parallel components, as fast wind is more Alfvénic and Alfvénic fluctuations are mainly perpendicular to the local mean magnetic field and are not compressive. At 0.72 AU, the Parker spiral (mean field) for the fast ( $700 \text{ km s}^{-1}$ ) solar wind would be around  $24^\circ$ , which is not far from the X direction in the VSO reference system. Thus, more power should be expected for the Y and Z components of the magnetic field (Klein et al. 1993). The anisotropy will be the subject of a future study on the same data set.

### 3. DISCUSSION AND CONCLUSIONS

We have investigated the spectral behavior of the solar wind magnetic field at 0.72 AU for low solar activity between 2007 and 2009 using data provided by VEX. The PSDs of the magnetic field components and the trace of the spectral matrix indicate that the inertial range of turbulence can be identified as power-law behavior in the fast and slow solar wind. More power is contained in the fast wind spectra which also exhibit shallower slopes than the slow wind. The mean value of the slope assumes values around  $-1.6 \pm 0.01$  for the fast wind and  $-1.65 \pm 0.01$  for the slow wind, respectively. Our results fully agree with general predictions found in the literature concerning different spectral slopes of magnetic field fluctuations depending on solar wind conditions.

In particular, Chen et al. (2013) clearly showed how the spectral index of the magnetic field and velocity fluctuations depend on their Alfvénicity, which can be expressed by the normalized cross-helicity  $\sigma_C$ . These authors, analyzing five years of *Wind* data, found that as  $\sigma_C$  decreases, the magnetic energy starts to dominate the kinetic energy, and the magnetic field spectrum becomes steeper than the velocity spectrum, in line with predictions (Müller and Grappin 2005, among others). The tendency for the magnetic spectrum to dominate over the kinetic is a natural outcome for stationary, critically balanced MHD turbulence (Goldreich & Sridhar 1995) generated by nonlinear interacting Alfvén waves (Gogoberidze et al. 2012). Consequently, since we study fast and slow wind, which differ in Alfvénicity (Bruno & Carbone 2013), with the fast wind being more Alfvénic than slow wind, we should expect to find magnetic field spectra in the fast wind less steep than those in slow wind. In addition, a comparison with similar data at 1 AU suggests that, on average, the spectra steepen while the slow solar wind is transported between 0.72 and 1 AU, suggesting that nonlinear interactions are at work. On the other hand, the fast wind exhibits less clear evidence of radial steepening.

The solar wind magnetic field spectral indices between 2007 and 2009 have a normal distribution. We do not find a significant temporal trend in the slopes. The average spectral slopes of the three magnetic components suggest an anisotropic repartition of power. There is evidence for a change in the spectral slope in the vicinity of the proton cyclotron radius, possibly associated with the transition from the inertial to the kinetic subrange.

Our results suggest that at 0.72 AU and solar minimum, the slow wind exhibits, on average, spectral behavior closer to the “ $f^{-5/3}$ ” law with some differences between the mean slopes of the magnetic field components. Thus, there are indications that the turbulence is anisotropic and models based on the isotropy hypothesis, like Kolmogorov (1941) and/or Iroshnikov–Kraichnan, are not applicable. Modern theories of anisotropic strong MHD turbulence (Goldreich & Sridhar 1995) predict that the perpendicular spectrum of turbulence may approach for some conditions the “ $f^{-5/3}$ ” scaling. In the absence of resolute plasma measurements from *VEX*, we can only suggest that the slow wind spectra are perhaps dominated by the perpendicular component. Nevertheless, the younger turbulence carried by the fast wind is described by shallower spectral slopes which show a tendency to approach asymptotically a “ $f^{-3/2}$ ” power law. This could possibly signify that the structure of the turbulence exhibits features consistent with models of anisotropic turbulence as in Boldyrev (2006). In other words, our results may suggest that the slow wind at 0.72 AU and solar minimum is dominated by filament-like structures at the smallest scales (as suggested by Goldreich & Sridhar 1995), while the fast wind turbulence is dominated by sheet-like structures at the smallest scales (as suggested by Boldyrev 2006), possibly related to phenomenological turbulent features of the solar wind at the origin, in the corona.

Research supported by the European Community’s Seventh Framework Programme (FP7/2007-2013) under grant agreement No. 313038/STORM, and a grant of the Romanian Ministry of National Education, CNCSUEFISCDI, project No. PN-II-ID-PCE-2012-4-0418. The data analysis was partially performed with the AMDA science analysis system provided by the Centre de Données de la Physique des Plasmas (IRAP, Université Paul Sabatier, Toulouse) supported by CNRS and CNES.

## REFERENCES

- Alexandrova, O., Saur, J., Lacombe, C., et al. 2009, *PhRvL*, 103, 16  
 Alexandrova, O., Chen, C. H. K., Sorriso-Valvo, L., Horbury, T. S., & Bale, S. D. 2013, *SSRv*, 178, 101  
 Batchelor, G. K. 1970, *The Theory of Homogeneous Turbulence* (Cambridge: Cambridge Univ. Press)  
 Barabash, S., Sauvaud, J.-A., Gunell, H., et al. 2007, *P&SS*, 55, 1772  
 Bavassano, B., & Bruno, R. 1989, *JGR*, 94, 168  
 Bavassano, B., & Bruno, R. 1991, *JGR*, 96, 1737  
 Boldyrev, S. 2006, *PhRvL*, 96, 115002  
 Borovsky, J. E. 2008, *JGR*, 113, A8  
 Borovsky, J. E. 2012a, *JGR*, 117, A5  
 Borovsky, J. E. 2012b, *JGR*, 117, A6  
 Bruno, R., & Carbone, V. 2013, *LRSP*, 10, 2  
 Bruno, R., D’Amicis, R., Bavassano, B., Carbone, V., & Sorriso-Valvo, L. 2007, *AnGeo*, 25, 1913  
 Bruno, R., & Trenchi, L. 2014, *ApJL*, 787, L24  
 Bruno, R., Trenchi, L., & Telloni, D. 2014, *ApJL*, 793, L15  
 Chen, C. H. K., Bale, S. D., Salem, C. S., & Maruca, B. A. 2013, *ApJ*, 770, 125  
 Chen, C. H. K., Leung, L., Boldyrev, S., Maruca, B. A., & Bale, S. D. 2014, *GeoRL*, 41, 8081  
 Chen, C. H. K., Mallet, A., Yousef, T. A., Schekochihin, A. A., & Horbury, T. S. 2011, *MNRAS*, 415, 3219  
 Coleman, P. J., Jr. 1968, *ApJ*, 153, 371  
 Dasso, S., Milano, L. J., Matthaeus, W. H., & Smith, C. W. 2005, *ApJL*, 635, L181  
 Gogoberidze, G., Chapman, S. C., & Hnat, B. 2012, *PoP*, 19, 2310  
 Goldreich, P., & Sridhar, S. 1995, *ApJ*, 438, 763  
 Forman, M. A., Wicks, R. T., & Horbury, T. S. 2011, *ApJ*, 733, 76  
 Frisch, U. 1995, *Turbulence* (Cambridge: Cambridge Univ. Press)  
 Horbury, T. S., Forman, M., & Oughton, S. 2008, *PhRvL*, 101, 175005  
 Horbury, T. S., Wicks, R. T., & Chen, C. H. K. 2012, *SSRv*, 172, 325  
 Kolmogorov, A. 1941, *DoANT*, 30, 301  
 Klein, L., Bruno, R., Bavassano, B., & Rosenbauer, H. 1993, *JGR*, 98, A10  
 Leamon, R. J., Smith, C. W., Ness, N. F., & Wong, H. K. 1999, *JGR*, 104, 22331  
 Marsch, E., & Tu, C.-Y. 1990, *JGR*, 95, 11945  
 Matthaeus, W. H., & Goldstein, M. L. 1986, *PhRvL*, 57, 495  
 Matthaeus, W. H., Oughton, S., Pontius, D. H., Jr, & Zhou, Y. 1994, *JGR*, 99, 19267  
 Müller, W.-C., & Grappin, R. 2005, *PhRvL*, 95, 114502  
 Podesta, J. J. 2009, *ApJ*, 698, 986  
 Ruiz, M. E., Dasso, S., Matthaeus, W. H., Marsch, E., & Weygand, J. M. 2011, *JGR*, 116, A10  
 Smith, C. W. 2003, in *AIP Conf. Proc.* 679, *Astronomy and Astrophysics*, ed. M. Velli, R. Bruno, & F. Malara (New York: AIP), 413  
 Tu, C.-Y., & Marsch, E. 1995, *SSRv*, 73, 1  
 Stawicki, O., Gary, S. P., & Li, H. 2001, *JGR*, 106, 8273  
 Verdini, A., Grappin, R., Pinto, R., & Velli, M. 2012, *ApJL*, 750, L33  
 Weygand, James M., Matthaeus, W. H., Dasso, S., & Kivelson, M. G. 2011, *JGR*, 116, A8  
 Welch, P. D. 1967, *IEEE Trans. Audio Electroacoustics*, AU-15, 70  
 Wicks, R. T., Horbury, T. S., Chen, C. H. K., & Schekochihin, A. A. 2010, *MNRAS*, 407, L31  
 Yordanova, E., Balogh, A., Noullez, A., & von Steiger, R. 2009, *JGR*, 114, A8  
 Zhang, T., Baumjohann, W., Delva, M., et al. 2006, *P&SS*, 54, 1336



# Paper V



# Effect of data gaps: Comparison of different spectral analysis methods

Costel Munteanu<sup>1,2,3</sup>, Catalin Negrea<sup>1,4,5</sup>, Marius Echim<sup>1,6</sup> and Kalevi Mursula<sup>2</sup>

*1. Institute of Space Science, Magurele, Romania*

*2. Department of Physics, University of Oulu, Finland*

*3. Department of Physics, University of Bucharest, Magurele, Romania*

*4. Cooperative Institute for Research in Environmental Sciences, University of Colorado Boulder, USA*

*5. Space Weather Prediction Center, National Oceanic and Atmospheric Administration, Boulder, Colorado, USA*

*6. Belgian Institute of Space Aeronomy, Brussels, Belgium*

## Abstract.

In this paper we investigate quantitatively the effect of data gaps for four methods of estimating the amplitude spectrum of a time series: Fast Fourier Transform (FFT), Discrete Fourier Transform (DFT), Z-Transform (ZTR) and Lomb-Scargle algorithm (LST). We devise two tests: the Single Large Gap test, which can probe the effect of a single data gap of varying size and the Multiple Small Gaps test, used to study the effect of numerous small gaps of variable size distributed within the time series. The tests are applied on two datasets: a synthetic dataset composed of a superposition of four sinusoidal modes and one component of the magnetic field measured by the Venus Express (VEX) spacecraft in orbit around the planet Venus. For single data gaps, FFT and DFT give an amplitude decreasing with gap size. However, the shape of their amplitude spectrum remains unmodified even for a large data gap. On the other hand, ZTR and LST preserve the absolute level of amplitude but lead to greatly increased spectral noise for increasing gap size. Therefore, for single data gaps, FFT is the best method to approximate the spectral slope. For multiple small data gaps, DFT, ZTR and LST can, unlike FFT, find the correct amplitude of sinusoidal modes even for large data gap percentage. However, for in-situ data collected in turbulent plasma environment these three methods overestimate the high frequency part of the amplitude spectrum above a threshold depending on the maximum gap size and the associated spectral noise, while FFT slightly underestimates it.

1  
2  
3  
4  
5  
6  
7  
8  
9  
10  
11  
12  
13  
14  
15  
16  
17  
18  
19  
20  
21  
22  
23  
24  
25  
26  
27  
28  
29  
30  
31  
32

## 1. Introduction

Spectral analysis is a widely used tool in data analysis and processing for most fields of science. The technique became extremely popular when the introduction of the Fast Fourier transform algorithm allowed for an extremely rapid computation of the Fourier Transform. In the absence of modern supercomputers, this was not just useful, but also the only realistic solution for such calculations. This limitation is no longer relevant except for datasets of extremely large size. Still, FFT has remained the most popular tool for spectral analysis, because it is both easy to use and very fast. This makes it an extremely powerful tool and generally it is the first choice from the “toolbox” of spectral analyses. It is readily available in all programming languages of notice and it is accurate under perfect conditions. However, real data is rarely perfect. We address here the very common problem of “data gaps” or non-uniform sampling. Due to the wide usage of FFT, the literature on this subject is spread over a wide array of scientific disciplines (*Horne and Baliunas 1986, Schimmel 2001, Thong et al. 2004, Hocke and Kampfer 2009*). However, despite the vast amount of literature, studies on the effects of non-uniform sampling are few in number. To our knowledge, there is no quantitative study that compares all the methods mentioned below.

We intend to quantify the distortions introduced by data gaps using four popular methods of estimating the frequency spectrum: Fast Fourier Transform, Discrete Fourier Transform, Z-Transform and Lomb-Scargle Transform. The results are compared qualitatively and quantitatively using synthetic and real data sets.

We use a synthetic time series, which consists of several periodic signals and added noise. Different, frequently encountered data gap configurations are applied to it and the amplitude spectra are calculated and compared to the known spectrum of the unaltered signal. Two gap configurations are used to highlight the effects: a) a single large gap, where the original dataset is altered by removing an increasing number of points from the central part, and b) multiple small gaps, where we remove short series of consequent points whose length and precise location are randomly selected. The same methodology is also used to test the effect of data gaps on the amplitude spectra of magnetic field measurements made by the Venus Express spacecraft in orbit around the planet Venus. For these two tests, we determine practical thresholds where the use of the FFT based implementation is no longer feasible.

1 The paper is structured as follows: a description of the general methodology and methods  
 2 is presented in Section 2; Section 3 shows the results for a synthetic dataset comprising of four  
 3 sinusoidal signals, and Section 4 applies the same methodology on a real data set of Venus  
 4 Express magnetic field measurements. Section 5 gives a brief summary and presents the main  
 5 conclusions of our study.

## 6 7 **2. Analysis methods**

8 The Fast Fourier transform is extremely fast to calculate, but requires strictly uniform  
 9 sampling. It is by far the most popular method for computing the frequency spectrum. It is  
 10 sometimes used on non-uniformly sampled data, first using linear interpolation to fill in the  
 11 data gaps. Linear interpolation alters the signals but the FFT is still able to capture an acceptable  
 12 level of spectral details, depending on the size and number of gaps. This is demonstrated  
 13 quantitatively and qualitatively in Sections 3 and 4.

14 The effect of the above-mentioned linear interpolation can be fully described  
 15 analytically. For a given signal  $x(t)$ , the Fourier transform  $y(\omega)$  is defined as:

$$16 \quad y(\omega) = \int_{-\infty}^{+\infty} x(t) * e^{-i\omega t} dt \quad (1)$$

17 If we assume a gap between  $t_a$  and  $t_b$ , we will have:

$$18 \quad y(\omega) = \int_{-\infty}^{t_a} x(t) * e^{-i\omega t} dt + g + \int_{t_b}^{+\infty} x(t) * e^{-i\omega t} dt,$$

19 where

$$20 \quad g = \int_{t_a}^{t_b} x(t) * e^{-i\omega t} dt \cong -g1 + g2,$$

21 with

$$22 \quad g1 = i \left( x(t_a) - \frac{x(t_b) - x(t_a)}{t_b - t_a} t_a \right) \frac{e^{-i\omega t_a} - e^{-i\omega t_b}}{\omega},$$

23 and

$$24 \quad g2 = \frac{x(t_b) - x(t_a)}{t_b - t_a} \frac{e^{-i\omega t_b(1+i\omega t_b)} - e^{-i\omega t_a(1+i\omega t_a)}}{\omega^2}, \quad (2)$$

25 where the data gap is replaced by a straight line. As  $\omega$  increases, both  $g1$  and  $g2$  will decrease  
 26 to zero, resulting in a smaller Fourier amplitude  $y(\omega)$ . This simple analytical example shows  
 27 that FFT, in case of data gaps, will decrease the spectral amplitudes.

28 The Discrete Fourier Transform is a discretization of the Fourier integral of eq. (1),  
 29 which we chose to do using the trapezoidal method:

$$30 \quad y(\omega) = \sum_{j=1}^n x(t_j) e^{-i\omega t_j} \frac{\Delta t_j}{2} \quad (3)$$

31 On the other hand, the Z Transform is a generalization of the Fourier Transform for  
 32 discrete series rather than for continuous functions:

$$y(\omega) = \sum_{j=1}^n x(t_j) e^{-i\omega t_j} \quad (4)$$

The Lomb-Scargle method performs a least squares fit of the data using a superposition of sinusoidal modes (*Lomb* 1976, *Scargle* 1982, 1989, *Hocke and Kampfer* 1998). While it is equivalent to FFT for uniform sampling, it can provide, as we will show later, very different results when analyzing data with non-uniform sampling.

Note that the issues due to data gaps are not limited to any one method, but are a fundamental property of the resulting amplitude spectrum. For a uniformly sampled dataset, there is an orthogonal set of frequencies for which the values of the Fourier coefficients are independent. In the case of non-uniformly sampled data, such an orthogonal set generally does not exist (*Van Dongen* 1999), allowing for spectral leakage to occur. This cannot be avoided regardless of the method used since the problem does not derive from the algorithm. For this reason the problem cannot be entirely resolved. We intend to diagnose the extent by which the data gaps impact the results obtained with different methods and for different gap configurations.

### 3. Synthetic data tests

In order to determine the effect introduced by data gaps on the Fourier transform, we test the four above mentioned spectral analysis methods on a synthetic signal with added gaps. The FFT method is applied on a signal where the gaps are linearly interpolated, while DFT, ZTR and LST are applied on a signal with no data interpolation. We test two configurations of gaps: a) Single Large Gap, based on the alteration of the original dataset by removing an increasing number of points from the central part; the procedure is repeated until the central gap reaches 99.8% of the total length of the signal, and b) Multiple Small Gaps, based on the alteration of the signal by removal of short series of consequent points whose length and precise location are randomly selected; the procedure is applied repeatedly for various distributions of random gaps. The two cases were studied first on a synthetic signal sampled uniformly.

The synthetic dataset is a superposition of 4 sinusoidal modes with unit amplitude and the following frequencies:  $f_1 = 10$  Hz,  $f_2 = 20$  Hz,  $f_3 = 30$  Hz and  $f_4 = 40$  Hz. The signal is sampled at 100 samples per seconds with a total length of  $L = 1000$  points. We also added a white noise with unit amplitude such that the synthetic signal  $y(t)$  can be described by:

$$y(t) = noise + \sum_{i=1}^4 \sin(2\pi \cdot f_i \cdot t), \quad (5)$$

1 and illustrated in Figure 1 together with its amplitude (FFT) spectrum. The latter serves as  
2 reference and will be compared to the spectra obtained by the four methods applied on various  
3 distributions of gaps.

### 5 3.1. Single Large Gap test applied on synthetic data

6 In this case the data gap is created by removing a number of points from the central part  
7 of the synthetic signal. We generate 100 signals from (5) on which we add one gap with size  
8 varying from 1% to 99.8% of the length of the original time series. As an example, we illustrate  
9 in Figure 2 the performance of the four methods on a signal whose gap is 50% of the length  
10 of  $y(t)$ . Figure 2 shows that when then the FFT analysis is applied on the interpolated signal,  
11 it provides a Fourier spectrum whose amplitude is half of the original spectrum at all four eigen-  
12 frequencies of the synthetic signal.

13 The accuracy of the amplitude spectrum computed with DFT is sensitive not only to  
14 the size of the central gap but also to the phase at the two end-points of the gap. If at least one  
15 end point has a value different from the mean value of the signal (which is zero in the case of  
16 our synthetic signals) then the results are distorted. This distortion is also seen in Figure 2,  
17 where the DFT amplitudes depict a very large background level (even above one), and the four  
18 signals barely rise above the background. This distortion is larger for large deviations of the  
19 two end points from the mean.

20 Since we are interested mainly on the effect of the gap size, we apply a Tukey (tapered  
21 cosine) window (*Bloomfield, 2000*) on the two parts of the signal around the gap, which cancels  
22 the offset on either side of the gap (as well as at start and end of the signal). In order to treat all  
23 methods similarly, we apply the same windowing procedure to all the four methods. The results  
24 obtained after the windowing procedure are shown in Fig. 3, in the same format as Fig. 2. For  
25 FFT, the windowing procedure removes the high amplitudes at very low frequencies seen in  
26 Fig. 2b, which were due to the slope of the linear interpolation. DFT results are now similar to  
27 FFT, and show the same 50% decrease in amplitude.

28 Figure 2 shows that the two other spectral analysis methods, ZTR and LST, provide  
29 very accurately the same amplitude level as the original, full dataset, even when the gap is quite  
30 wide. We also see that the spectral background level ( $\sim 3 \cdot 10^{-2}$ ) is larger for these two  
31 methods, compared to the original level of  $\sim 10^{-2}$  depicted in Figure 1b. Figure 3 shows that  
32 the windowing procedure hardly affects the ZTR and LST results. The increase of the spectral

1 background will have important implications for the analysis of real data, as we will see in  
2 Section 4.

3         Figures 4 and 5 show how the amplitudes change when the length of the central gap is  
4 increased. Figure 4 shows the amplitude spectra obtained for the four methods in color coding,  
5 with y-axis giving the TGP of the signal and x-axis representing the frequency. Figure 4  
6 includes 100 spectra of the signal (5) with central gap increasing linearly from 1% to 99.8% of  
7 the signal. Figure 4a shows that the amplitude spectrum calculated by the FFT transform  
8 decreases systematically with increasing size of the central gap. The results of the FFT and the  
9 windowed DFT are very similar until the TGP exceeds about 80%, whence the DFT  
10 background noise level increases dramatically. The spectra corresponding to gap sizes larger  
11 than about 50% exhibit a gradual appearance and broadening of a series of side lobes, leading  
12 to “palm tree” shape in the vicinity of the singular frequencies. The gradual broadening of the  
13 individual spectral lines can be explained by the finite length of the original signal; the  
14 degradation of the signal by removal of an increasingly large central part decreases the number  
15 of sinusoidal peaks and leads to a broadening of the spectral line.

16         The spectra obtained with ZTR and LST are quite different, but bear some similar  
17 features. As the size of the central gap increases, the signal amplitude remains almost constant  
18 for all the four signals. Moreover, Figure 4 shows that the side lobes (the “palm tree”) and the  
19 background noise have considerably larger amplitudes for ZTR and LST than FFT and DFT.

20         In order to illustrate even more quantitatively the response of the four methods to the  
21 increasing size of the central gap we have studied the change for the first frequency,  $f_1=10$  Hz,  
22 of the full signal. Figure 5 shows how the amplitude of the spectrum at  $f_1$  varies with TGP. FFT  
23 and DFT transforms give the same result up to  $TGP < 80\%$ ; the amplitude is monotonically  
24 decreasing with increasing TGP. Beyond TGP of about 80%, the DFT amplitude increases  
25 rather randomly, indicating the increasing background level. On the other hand the amplitude  
26 at  $f_1$  obtained from ZTR and LST remains very closely at 1 up to TGP of about 95%. Beyond  
27 this value, both methods give increasingly disturbed amplitude levels.

28         Figure 6 shows the integral of the amplitude spectrum, i.e. the sum of all amplitudes,  
29 as a function of the TGP. In order to study the effect of spectral noise we calculated the integral  
30 not only for the synthetic signal given by equation (5), but also for a “clean” signal (the sum of  
31 sinusoids without noise) as well as for pure noise. We found that FFT and DFT behave in a  
32 similar way within the limit of small TGP, up to about 60% (see earlier discussion). The integral  
33 corresponding to the clean signal has an almost constant value as we increase the gap size. For  
34 pure noise, the integral decreases with increasing gap size. For the signal contaminated with

1 noise (the original signal given by eq. 5) the result is a combination of these two cases, i.e. the  
2 integral slowly decreases with increasing TGP.

3 For the ZTR and LST methods, the integral increases as we increase the gap size not  
4 only for pure noise and the noisy signal, but also for the clean sum of sinusoids. We already  
5 observed in Figure 3 that, for the 50% TGP, the spectral background was larger than the original  
6 background. We see here that the background level increases systematically as we increase the  
7 gap size, eventually dominating the integral for large TGP and explaining the overall increase  
8 for all three signals depicted in Fig. 6. This result will have an important impact on the analysis  
9 of solar wind data, where dominant harmonics are less frequent and the spectral noise  
10 dominates the integral.

11

### 12 3.2. Multiple Small Gaps test applied on synthetic data

13 The second test performed on the synthetic signal of eq. (5) consists of removing a  
14 number of randomly distributed points from the original signal. This test mimics the situation  
15 often encountered in the experimental investigation of various geophysical or space systems  
16 (e.g., ground based measurement of the geomagnetic field or satellite measurement of the  
17 plasma and field parameters of the solar wind), where randomly distributed data gaps are an  
18 inherent problem.

19 We calculate the size distribution of the gaps using the gamma function  $\Gamma$ , which can  
20 be described by two parameters: the shape parameter  $A_g$  and the scale parameter  $B_g$ . The  
21 Probability Density Function (PDF) for the gamma distribution can be expressed in terms of  
22  $A_g$  and  $B_g$ , as follows:

$$23 \quad PDF_g(x|A_g, B_g) = \frac{x^{A_g-1} \cdot e^{-x/B_g}}{B_g^{A_g} \cdot \Gamma(A_g)} \quad (6)$$

24 We use this PDF to create statistical ensembles of gaps, with gap size probability being  
25 controlled by the mean ( $M_g = A_g \cdot B_g$ ) and variance ( $V_g = A_g \cdot B_g^2$ ) of the gamma distribution. In  
26 practice we choose a set of values for  $M_g$  and  $V_g$  and then compute a vector of gamma  
27 distributed random numbers according to equation (6). The obtained vector comprises of a set  
28 of real numbers from  $\sim$  zero to a positive value  $G_m$  depending on  $M_g$  and  $V_g$ . These numbers  
29 are rounded to the nearest integer value and thus we obtain the distribution of gap sizes, each  
30 integer giving the number of consecutive points to be removed from the uniformly sampled  
31 signal. The increasing degradation of the signal is achieved by increasing both  $M_g$ , which  
32 increases the size of the most probable gap, and  $V_g$ , which increases the probability of obtaining  
33 large gaps.

1 As in the case of SLG, we calculate the Fourier spectra and index them according to  
2 the selection of  $M_g$  and  $V_g$  values. We also define the Total Gap Percent associated with each  
3 spectrum as the total percent of points removed from the signal, computed as the sum of all  
4 gaps.

5 Figure 6 shows an example of a distribution of gaps for  $M_g = 2.1$  and  $V_g = 1.1$ , which  
6 removes 51% of the points of the signal. In this example the gaps with small size (between 1  
7 and 3 consecutive points) have high probability and their cumulative effect is to remove of  
8 more than 40% of the points of the original signal, as indicated by Fig. 7b. The largest gap in  
9 this example has a size of 8 points; there is only one gap of this size.

10 The amplitude spectrum obtained with FFT shows that the amplitude of the sinusoidal  
11 modes decreases systematically with increasing frequency. The other three methods (DFT,  
12 ZTR and LST) are very robust for this configuration of gaps and show no major modification  
13 in the amplitude spectra compared with the original results (see Fig. 1).

14 The methodology outlined above was applied on an ensemble of 100 synthetic signals  
15 obtained by degrading the original signal by increasing the number of missing points according  
16 to the gamma distribution. The mean and variance of the distribution of gaps increase with  
17 signal number, and thereby, the total number of removed points increases, although not strictly  
18 linearly. Figure 8a shows for each of the 100 degraded signals the percentage of total missing  
19 points (the TGP value) and Fig. 8b shows the distribution of gap percentage as a function of  
20 signal index and gap size. We note that this statistical ensemble of signals covers indeed a  
21 broad range of different possible configurations, relevant to investigate the response of the four  
22 spectral analysis methods.

23 Figure 9 depicts the amplitude spectra of the 100 signals described above and in Fig. 8  
24 as a function of TGP and frequency, similar to the SLG test of Fig. 4. One can see that the FFT  
25 amplitude decreases with frequency and with increasing TGP. The results for DFT, ZTR and  
26 LST show little decrease in amplitude and no frequency dependence when TGP increases.

27 Figure 10 shows the FFT amplitudes as a function of TGP separately for the four  
28 frequencies  $f_1$ - $f_4$ . FFT amplitudes decrease rather systematically with TGP. However, there is  
29 some variation in amplitudes, especially for large TGP, which is due to the different effect of  
30 each individual gap sample. So, TGP is not the only factor affecting the amplitude, but also the  
31 distribution of gaps matters.

32 Figure 11 shows the analogue of Fig. 6 for MSG test., i.e. the amplitude integral as a  
33 function of TGP. As in Fig. 6, the amplitude integral for the original signal is removed in each  
34 case. There are interesting differences between Fig. 11 and Fig. 6 that are related to the different

1 gap structure between the two cases, even for the same total TGP. In particular there is a  
2 much larger integral amplitude in FFT, even for clean sinusoids, which is due to increased  
3 background power. Figure 9 shows that FFT amplitude increases at low frequencies with TGP.  
4 However, there is increased background level even at lower TGP of about 40% (see Fig. 9),  
5 where the integral amplitude attains its maximum, as seen in Fig. 11.

## 7 **4. Satellite data tests**

8 We now apply the above methods to the magnetic field data from Venus Express (VEX)  
9 spacecraft (Zhang et al. 2006) in orbit around the planet Venus. The signal represents a sample  
10 of the x component of the solar wind magnetic field, measured by VEX on 17.01.2007. It  
11 includes 1000 data points sampled at 1 s time resolution, forming a time series of 16 minutes  
12 and 40 seconds without gaps. Figure 12 shows the signal and its FFT amplitude spectrum.

### 14 **4.1. Single Large Gap test applied on VEX data**

15 This testing method is identical to the one described above in Section 3.1. A case study  
16 obtained by removing 50% of the central part of the original signal (TGP = 50%) is shown in  
17 Fig. 13. Since the signal does not have significant peaks in the original spectrum (see Fig. 12),  
18 we study the performance of the four methods by comparing amplitude spectra, which have  
19 been averaged by a 100-point moving mean filter. Like in the corresponding synthetic test, we  
20 see that FFT and DFT perform roughly in a similar way. The amplitude spectra of the signal  
21 with TGP = 50% are at a clearly lower level than the original spectrum over the whole  
22 frequency interval. For ZTR and LST the overall average level of the spectrum is fairly similar  
23 to the original one.

24 The results for the ensemble of 100 signals with the TGP increasing linearly from 1%  
25 to 99.8% (the procedure described in Section 3.1) are shown in Figures 14 and 15 (analogues  
26 of Figures 4 and 5). These figures illustrate the difference between the spectrum of the signal  
27 with and the original spectrum. FFT and DFT show in Figure 14 an overall decrease in  
28 amplitude with increasing gap size. However, due the more complicated spectral content of the  
29 real signal, the results are not as clear as for the synthetic signal (Figure 4). Also, due to edge  
30 effects, the DFT amplitude shows a large increase especially at high frequencies. ZTR and LST  
31 show an increase in amplitude with increasing gap size. Figure 14 shows the integral of the  
32 amplitude spectra as a function of TGP. We see here a pattern very similar to the one obtained

1 for pure noise analysis (see Fig. 6b): a decrease in FFT and DFT (until about 60% TGP) and  
2 an increase in ZTR and LST as we increase the gap size.

#### 4 4.2. Multiple Small Gaps test applied on VEX data

5 A case study for the VEX signal from which we have removed 50.6% of the points by  
6 introducing small gaps according to the gamma distribution is shown in Figure 16. We see that  
7 this gap configuration produces excessive power over most of the frequency range for DFT,  
8 ZTR and LST. Only FFT produces an amplitude spectrum that is close to the original one. One  
9 can notice a threshold frequency at about  $f_t=2 \cdot 10^{-2}$  Hz which is common for the three methods,  
10 above which the spectral slope departs strongly from the original one. This threshold value is  
11 related to the critical signal to noise ratio (SNR); when SNR is small, the three methods produce  
12 very noisy spectra that are not reliable when studying the distribution of power at different  
13 frequencies, which is a key information for many types of studies.

14 Figures 17 and 18 show the results of the test for the ensemble of 100 signals with  
15 variable gap size distribution generated by the gamma function. Figure 17 shows the difference  
16 between the actual amplitude spectrum and the original spectrum. It gives us a synoptic view  
17 of the behavior of the four methods when degradation is increasing. Figure 17 shows that the  
18 FFT amplitude spectrum underestimates the original spectrum for frequencies higher than  
19 about 0.1 Hz.

20 On the other hand, DFT, ZTR and LST overestimate the spectrum over most of the  
21 frequency range. A significant increase is detected for frequencies larger than 0.15 Hz, in  
22 agreement with the case study depicted in Figure 16. Interestingly the increase seen in these  
23 three methods is frequency dependent, and the affected range of frequencies seems to depend  
24 on the actual distribution of the gaps and the power of the signal. These results indicate that, at  
25 least when the data includes gaps, FFT is the best method to approximate reliably the spectral  
26 slope of a signal recorded in a turbulent environment. Figure 18 illustrates the integral spectral  
27 amplitude (as difference to the original) as a function of the TGP. The integral gives a global  
28 measure of the spectrally differentiated behavior seen in Figure 17. Figure 18 shows  
29 quantitatively the better agreement of the FFT amplitude with the original spectrum, than the  
30 three other methods, even for large TGP.

1  
2  
3  
4  
5  
6  
7  
8  
9  
10  
11  
12  
13  
14  
15  
16  
17  
18  
19  
20  
21  
22  
23  
24  
25  
26  
27  
28  
29  
30  
31  
32  
33

## 5. Discussion and conclusions

We have analyzed the effect of data gaps on four commonly used spectral analysis methods: the Fast Fourier Transform, the Discrete Fourier Transform, the Z Transform and the Lomb-Scargle algorithm. FFT is extremely fast and readily available in all programming languages, and it is by far the most popular method of estimating the amplitude spectrum. It is often applied also to signals containing data gaps, using interpolation to compensate for the lack of data. The simple discretization of the Fourier integral using the trapezoidal method (DFT), can be used without interpolation even in the presence of data gaps. The Z transform, a generalization of the Fourier transform for discrete series and the Lomb-Scargle algorithm, a least squares fit of the data using a superposition of sinusoidal modes, are straight-forwardly applicable for time series with non-uniform sampling and/or data gaps.

In order to study the effect of data gaps and to mimic frequently encountered gap configurations, we devised two tests: the Single Large Gap test, which removes a number of consecutive points from the signal, and the Multiple Small Gaps test, which removes a number of randomly distributed gaps whose size was given by the gamma distribution. Both tests include an ensemble of 100 signals with gap percentage increasing from 1% (4.3%) to 99.8% (83.6%) in the case of the SLG test (MSG test, respectively). The tests are applied on two data sets: a simple superposition of four sinusoidal modes and magnetic field measurements made by the Venus Express spacecraft in orbit around planet Venus. Since the DFT method gives reasonable results in the SLG test only after windowing, the signal was windowed for all four methods, although the effect of windowing was minimal for the other methods.

For FFT and DFT, the SLG test shows monotonically decreasing amplitudes of the sinusoidal modes, with increasing Total Gap Percent. For DFT this decrease continues only to the limit of TGP of about 80%, where after the background level increases considerably because the windowing procedure becomes less effective (due to the small number of data points and related numerical noise). For VEX data, used here as an example of a realistic dataset with a more complex spectrum, the results are influenced by the non-stationarity of the time series but, overall, we see a similar decrease in FFT and DFT amplitude when increasing the TGP, as for the synthetic data. For the synthetic dataset, ZTR and LST show neither decrease in the amplitude of the sinusoidal modes nor frequency dependence, when TGP is increased in the SLG test. However, for very large gaps, the spectral background becomes increasingly

1 noisy, leading to an overall increase of the average level of the spectrum. For VEX data, since  
2 we do not have clear spectral peaks, we only see the increase of the average level of the  
3 spectrum as TGP increases.

4 The MSG test probes the effect of small, randomly distributed, gaps within the time  
5 series. For the synthetic dataset, FFT is the only method which is severely affected by such  
6 small gaps, showing decreased amplitude and systematic frequency dependence in amplitude  
7 reduction, with high frequencies being most affected. On the other hand, DFT, ZTR and LST  
8 are able to recover the amplitudes of the sinusoidal modes, but the spectral background  
9 becomes increasingly noisy when increasing TGP. For VEX data, FFT shows a similar  
10 decrease in amplitude and frequency dependence as for the synthetic case. On the other hand,  
11 DFT, ZTR and LST seriously overestimate the high frequency part of the amplitude spectrum  
12 above a certain frequency threshold. Moreover, we found that this threshold is dependent on  
13 the distribution of the small data gaps, and is moving to a lower frequency as the maximum  
14 gap increases. Beyond this threshold the spectral amplitude is roughly constant since the data  
15 gaps cover a large range of gap sizes corresponding to the frequency range above the threshold.

16 Concluding, the FFT method can be used even for relatively large single data gaps,  
17 although the absolute value of the amplitude spectrum is systematically reduced with gap size.  
18 On the other hand, the ZTR and LST methods preserve the absolute level of the amplitude  
19 spectrum, but are more vulnerable to increasing spectral background arising from increasing  
20 data gap percentage. They are recommended for the analysis of signals with strong sinusoidal  
21 modes, giving robust results for the amplitude of sinusoidal modes. For more turbulent spectra,  
22 the appearance of side lobes and spectral noise makes the effect of data gaps more pronounced  
23 for these methods than for FFT. Thus, our results indicate that, at least when the data includes  
24 gaps, FFT is the best method to approximate reliably the spectral slope of a signal recorded in  
25 a turbulent environment.

## 27 **Acknowledgements**

28 The research leading to these results has received funding from the European  
29 Community's Seventh Framework Programme (FP7/2007–2013) under grant agreement  
30 313038 (STORM), and a grant of the Romanian Ministry of National Education,  
31 CNCSUEFISCDI, project No. PN-II-ID-PCE-2012-4-0418. We also acknowledge the  
32 financial support by the Academy of Finland to the ReSoLVE Center of Excellence (project  
33 272157) and to project 264994.

1  
2  
3  
4  
5  
6  
7  
8  
9  
10  
11  
12  
13  
14  
15  
16  
17  
18  
19  
20  
21  
22  
23  
24  
25  
26

## References

P. Bloomfield - *Fourier Analysis of Time Series: An Introduction*, New York: Wiley-Interscience, 2000.

H.P.A. van Dongen et al. – *A procedure of multiple period searching in unequally spaced time series with the Lomb Scargle method*, Biological Rhythm Research, 30:2, 1999.

J. H. Horne and S. L. Baliunas: *A prescription for period analysis of unevenly sampled time series*, The Astrophysical Journal, 302, 1986.

K. Hocke and N. Kampfer– *Gap filling and noise reduction of unevenly sampled data by means of the Lomb-Scargle periodogram*, Atmos. Chem. Phys., 9, 2009.

K. Hocke – *Phase estimation with the Lomb-Scargle periodogram method*, Ann. Geophysicae, 16, 356–358, 1998.

N. R. Lomb – *Least-squares frequency analysis of unequally spaced data*, Astrophysics and Space Science, 1976.

M. Schimmel: *Emphasizing difficulties in the detection of rhythms with Lomb-Scargle periodograms*, Biol. Rhythm Res., 32:3, 2001.

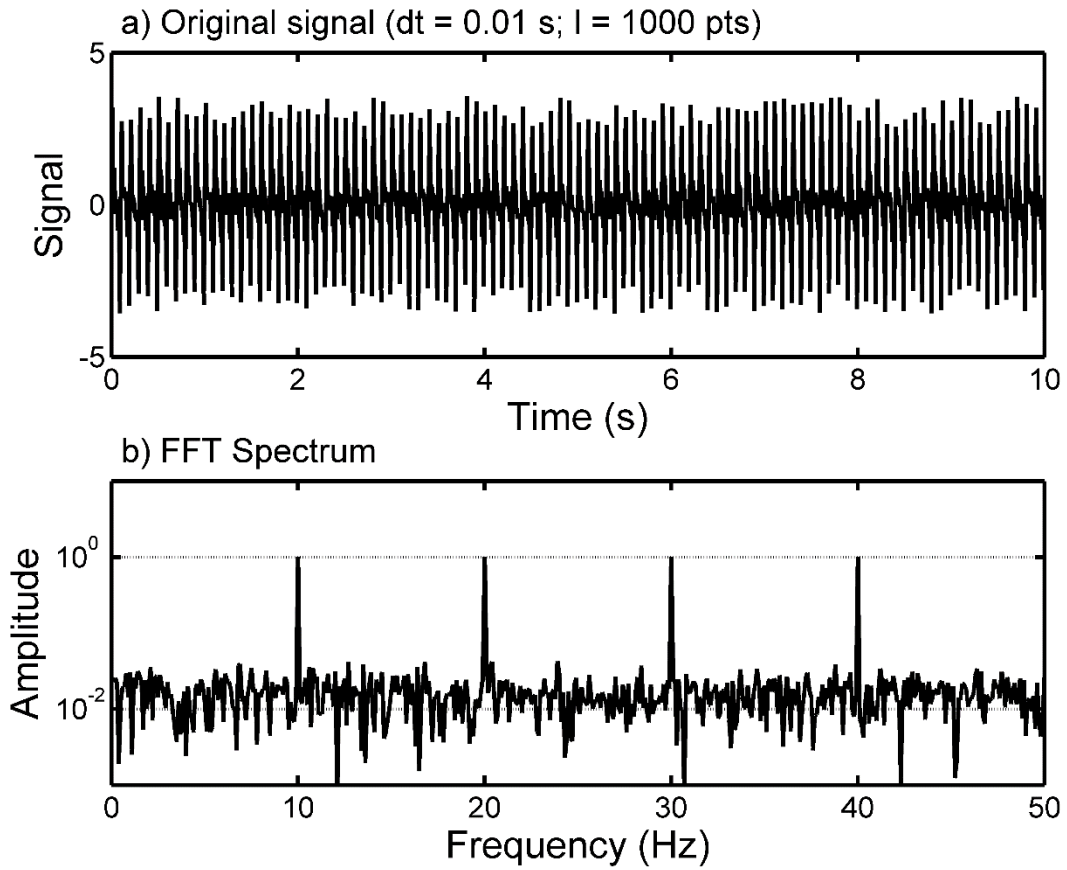
J. D. Scargle – *Studies in astronomical time series analysis. II. Statistical aspects of spectral analysis of unevenly spaced data*, The Astrophysical Journal, 263, 1982.

J. D. Scargle – *Studies in astronomical time series analysis. III. Fourier transforms autocorrelation functions and cross-correlation functions of unevenly spaced data*, The Astrophysical Journal, 343, 1989.

T. Thong – *Averaged Lomb Periodograms for Non-uniform Sampling*, Conf. Proc. IEEE Eng. Med Biol. Soc., 2004.

T. L. Zhang et al. – *Magnetic field investigation of the Venus plasma environment: Expected new results from Venus Express*, Planetary and Space Science, 54, 1336–1343, 2006

1



2

3 **Figure 1.** a) Synthetic signal and b) its associated FFT amplitude spectrum. The signal consists  
4 of 4 sinusoidal modes.

5

6

7

8

9

10

11

12

13

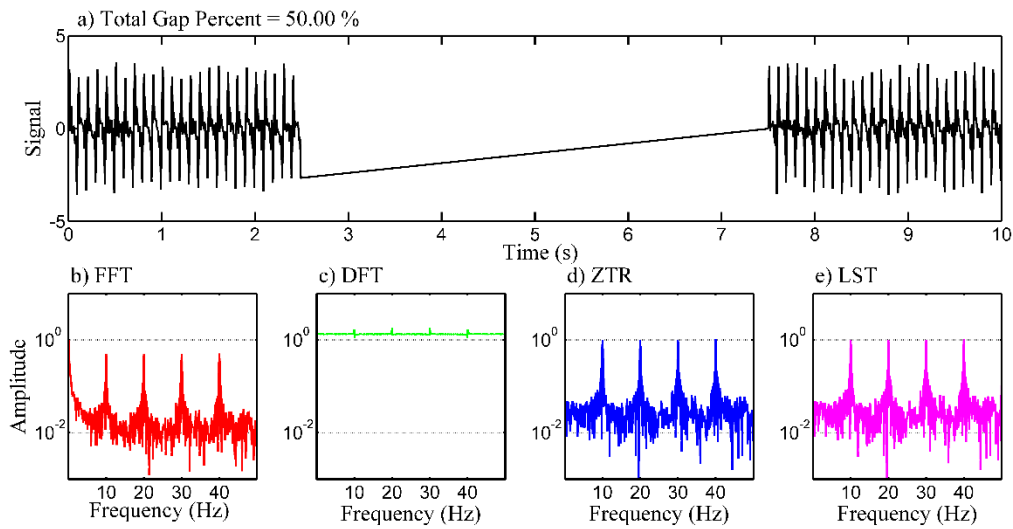
14

15

16

17

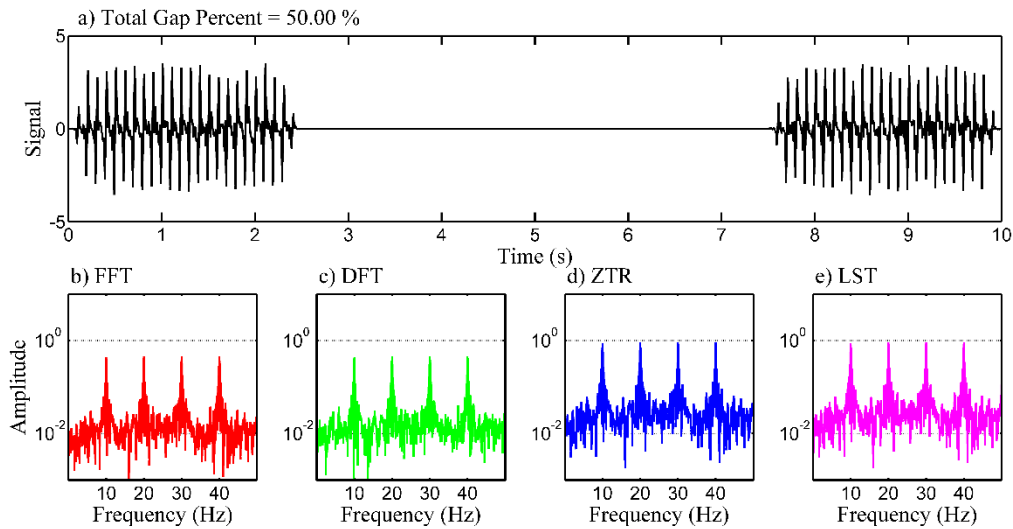
1



2

3 **Figure 2.** Single Large Gap test applied on synthetic data. Panel a) shows the non-windowed  
 4 signal with TGP of 50% and panels b), c), d) and e) show the corresponding amplitude spectra  
 5 computed with Fast Fourier Transform (FFT), Discrete Fourier Transform (DFT), Z-  
 6 Transform (ZTR) and Lomb-Scargle Transform (LST). TGP (Total Gap Percent) represents  
 7 the total number of points removed from the time series as a percent of the original length  $L$ .

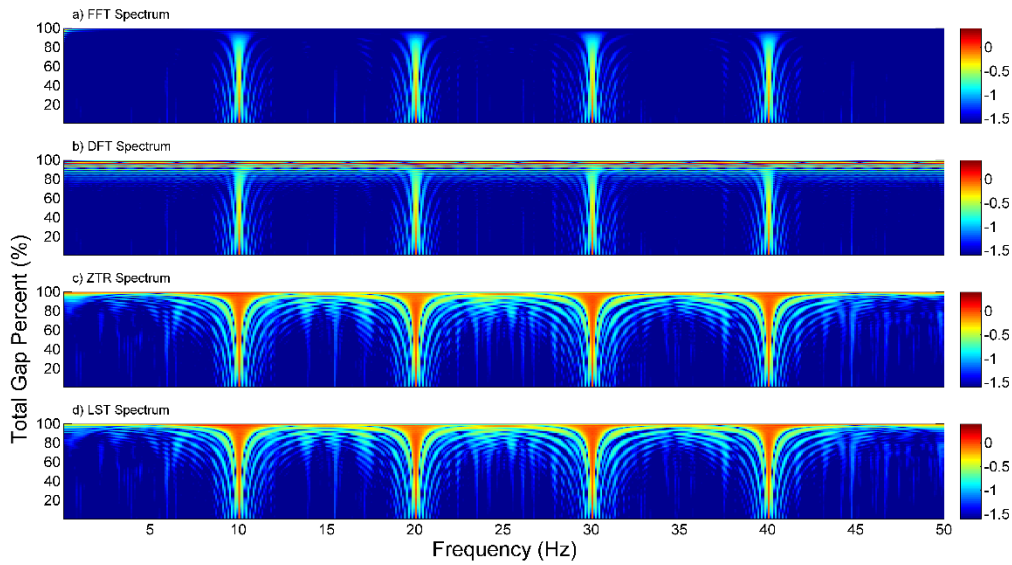
8



9

10 **Figure 3.** Single Large Gap test applied on synthetic data. Panel a) shows the windowed signal  
 11 with TGP of 50% and the other panels are the same as in Fig. 2.

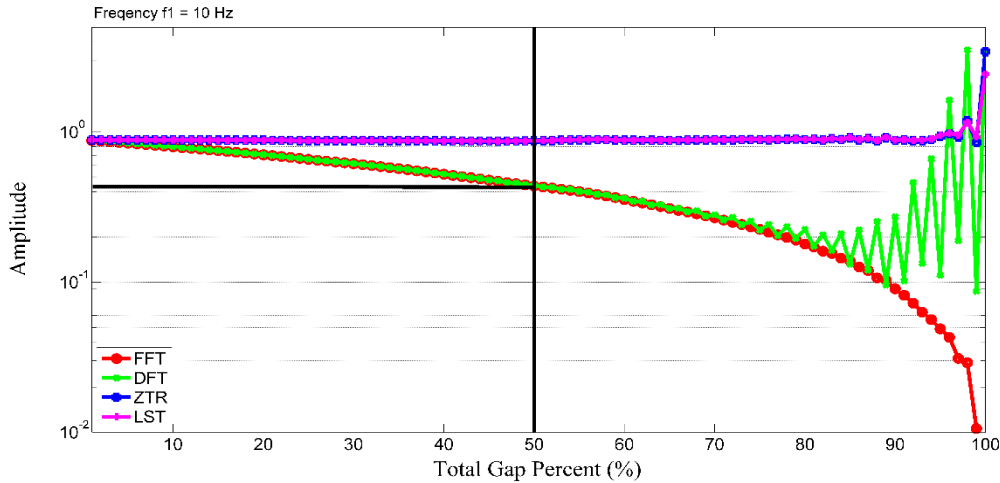
1



2

3 **Figure 4.** Single Large Gap test applied on synthetic data: amplitude in color code as a  
 4 function of TGP and frequency. Panels a) b) c) and d) show the results for FFT, DFT, ZTR and  
 5 LST. Color scale is logarithmic and the color bars denote the  $10\log$  of amplitude.

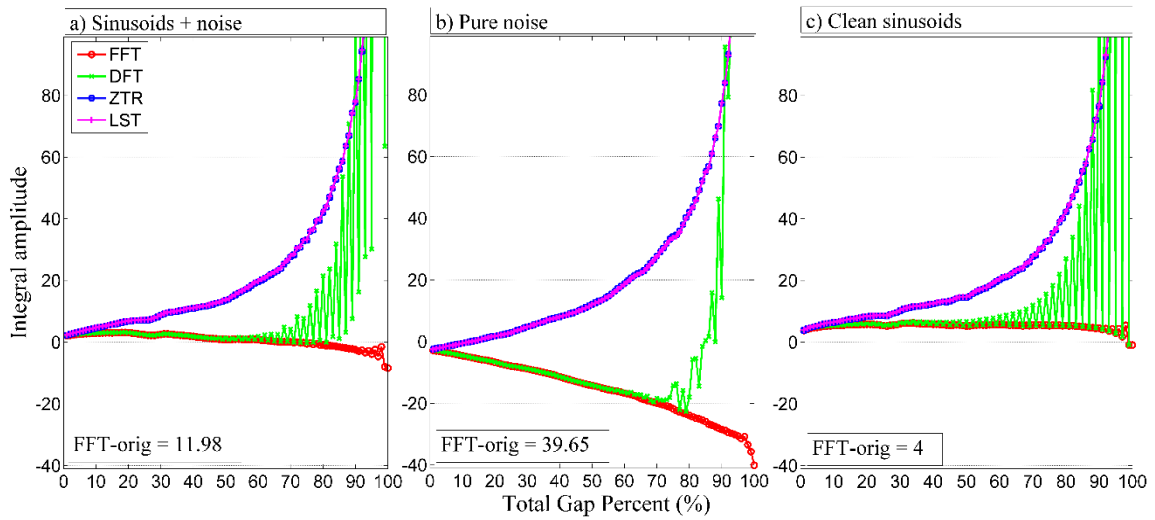
6



7

8 **Figure 5.** Single Large Gap test applied on synthetic data: amplitude of the 10 Hz sinusoidal  
 9 mode ( $f_1$ ) as a function of TGP for: FFT (red line marked with circles), DFT (green with x),  
 10 ZTR (blue and square) and LST (magenta and +). The case study for TGP of 50% (see Fig. 2)  
 11 is noted as a vertical black line and the horizontal black line gives the FFT amplitude for this  
 12 case.

1



2 **Figure 6.** Integral amplitudes for the Single Large Gap test applied on synthetic data as a  
3 function of TGP for the signal with noise (panel a), for pure noise (panel b) and for clean signal  
4 (panel c). Color denotes the four methods.

5

6

7

8

9

10

11

12

13

14

15

16

17

18

19

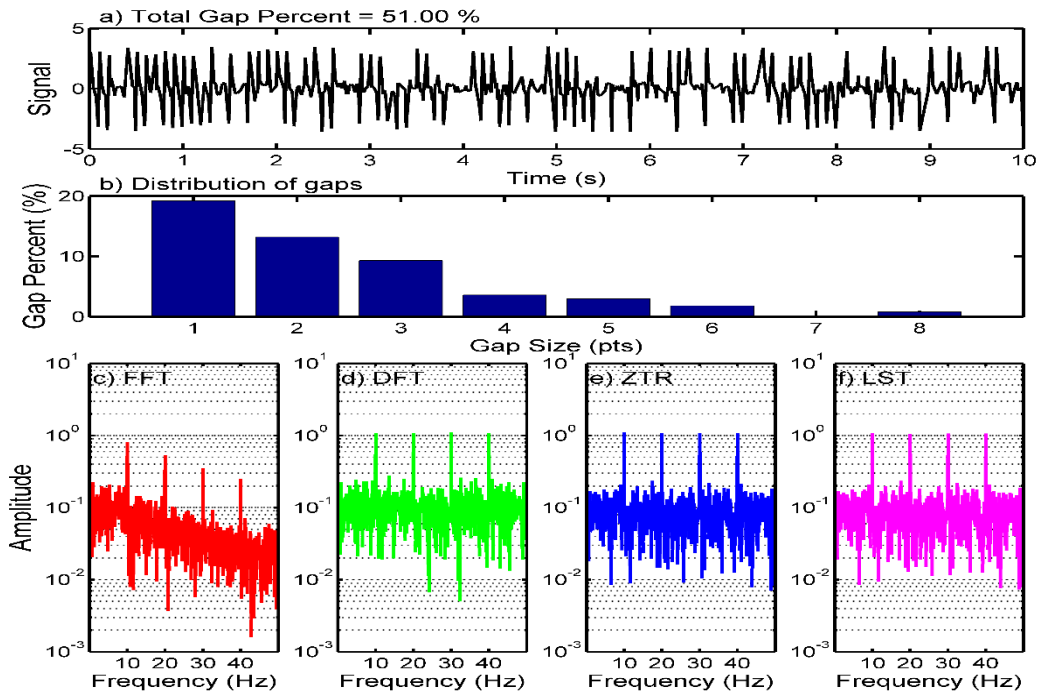
20

21

22

23

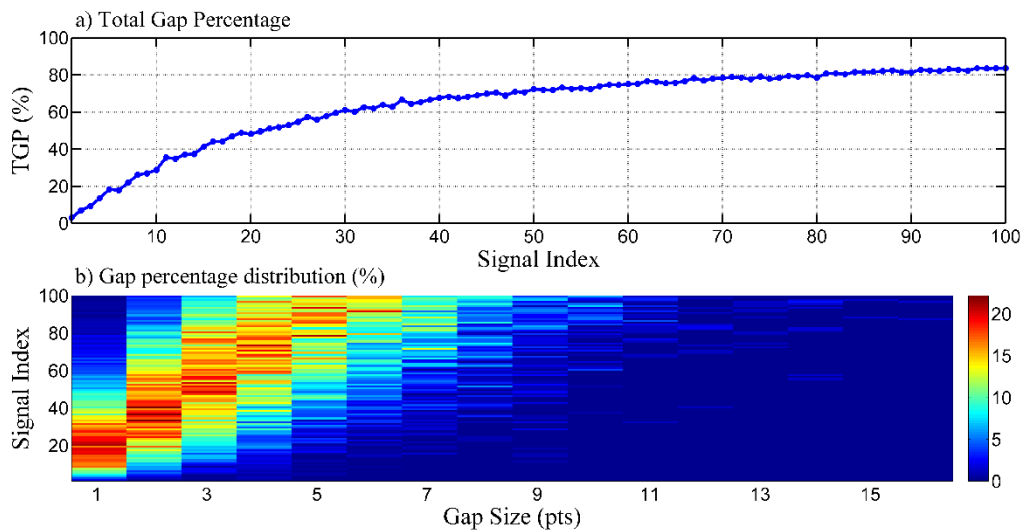
1



2

3 **Figure 7.** Case study for the Multiple Small Gaps test applied on synthetic data. The format is  
 4 similar to Fig. 2, except for panel b), which shows the individual gap percent as a function of  
 5 gap size corresponding to this case study. The correct amplitude of the sinusoidal modes (10,  
 6 20, 30, 40 Hz) is equal to 1, value retrieved by DFT, ZTR and LST.

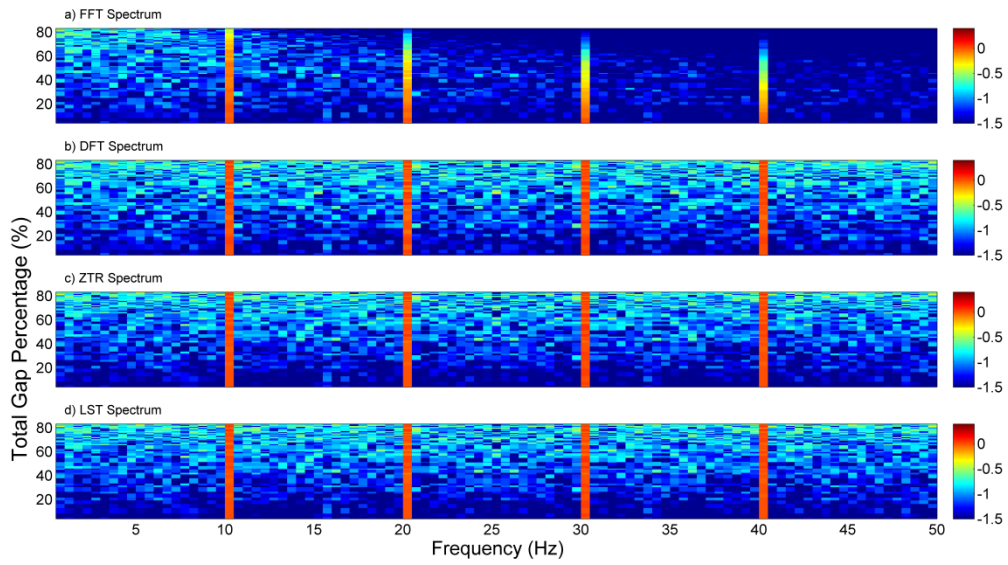
7



8

9 **Figure 8.** a) Total Gap Percent as a function of signal index; b) distribution of gap percentage  
 10 (color coded) as a function of signal index and gap size for the Multiple Small Gaps test.

1

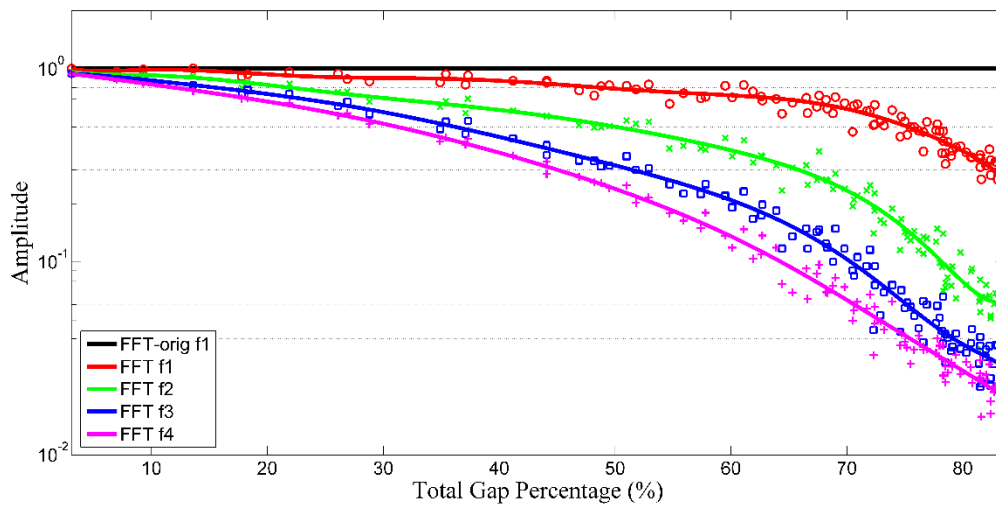


2

3 **Figure 9.** Multiple Small Gaps test applied on synthetic data: amplitude spectra in color code  
 4 as a function of TGP and frequency for: FFT (panel a) DFT (panel b), ZTR (panel c) and LST  
 5 (panel d). Color as in Fig. 3.

6

7

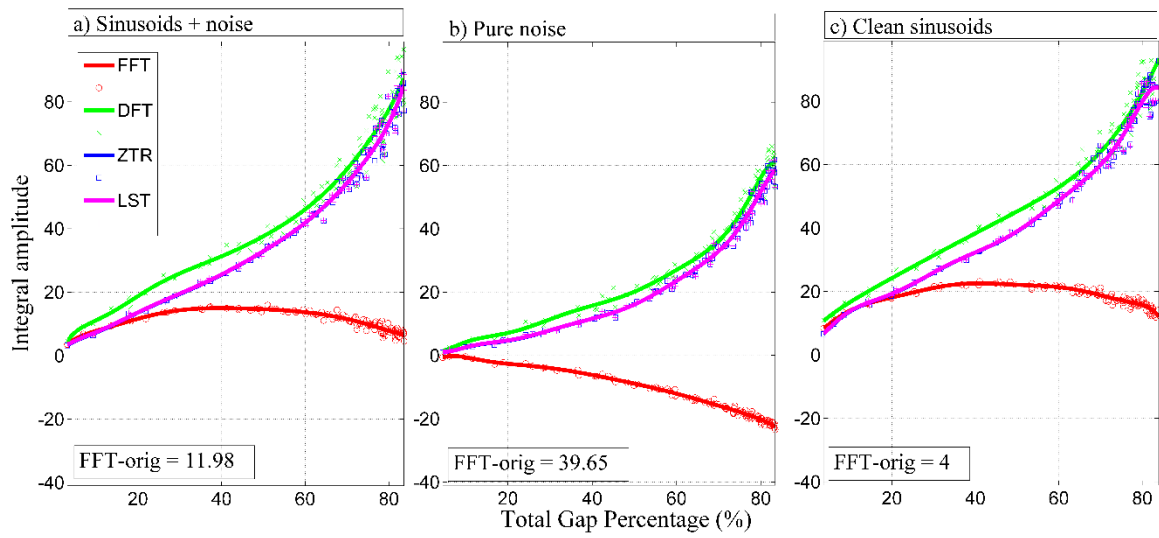


8

9 **Figure 10.** Multiple Small Gaps test applied on synthetic data: FFT amplitude as a function of  
 10 TGP for the four frequencies of the synthetic signal:  $f_1 = 10$  Hz (red),  $f_2 = 20$  Hz (green),  $f_3 =$   
 11  $30$  Hz (blue),  $f_4 = 40$  Hz (magenta). Lines are 9<sup>th</sup> order polynomials fit to the individual  
 12 amplitudes. The original signal amplitude is shown in black.

13

1



2

3 **Figure 11.** Integral amplitudes for the Multiple Small Gaps test applied on synthetic data. The  
4 format is identical to Fig. 5.

5

6

7

8

9

10

11

12

13

14

15

16

17

18

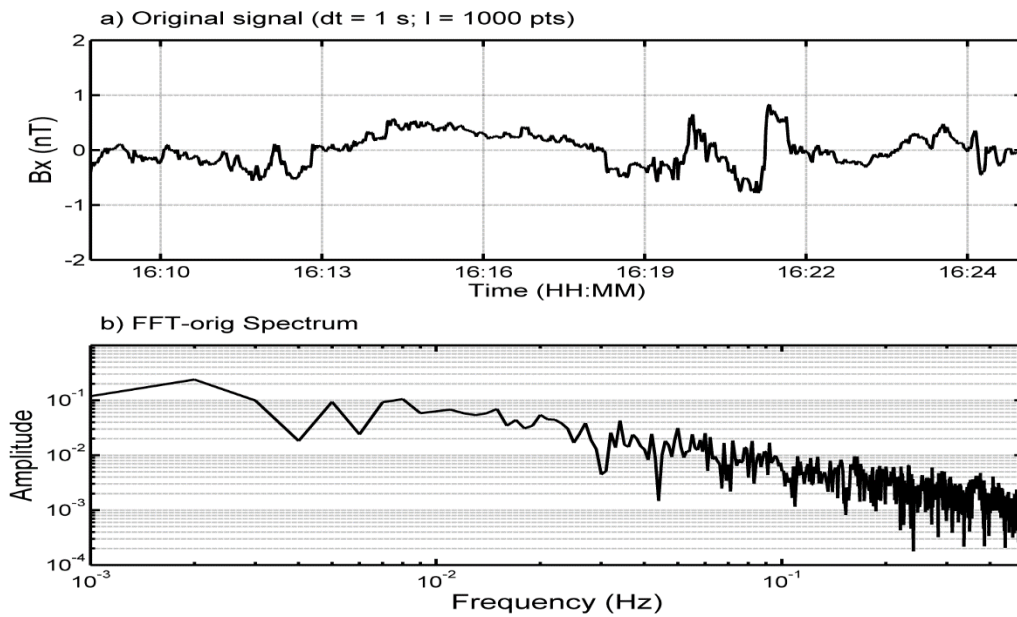
19

20

21

22

1



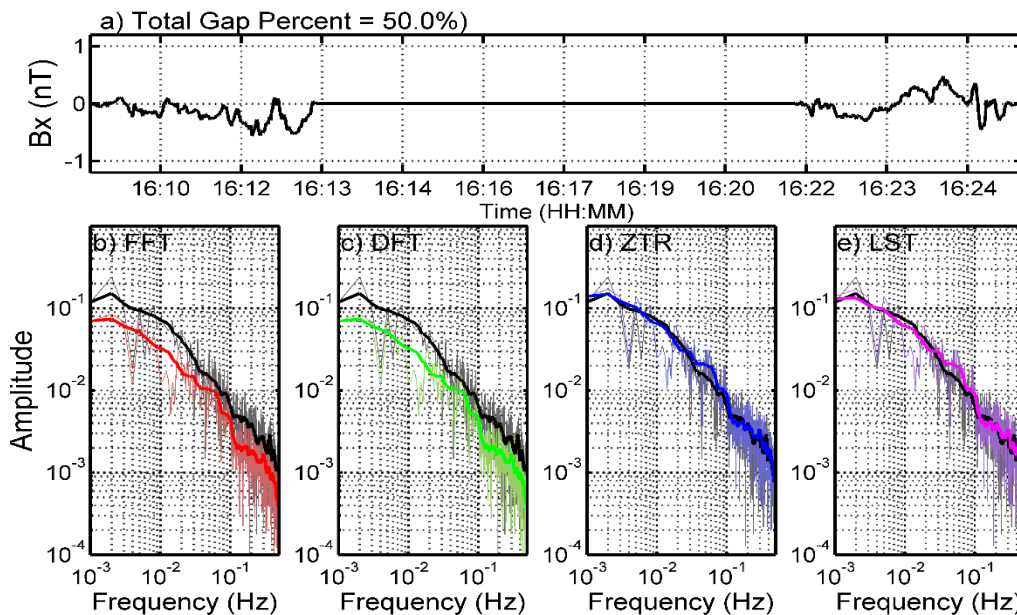
2

3

4 **Figure 12.** A Venus Express magnetic field signal. Panel a) shows the  $B_x$  component of the  
 5 magnetic field as a function of time and panel b) shows its FFT amplitude spectrum

6

7

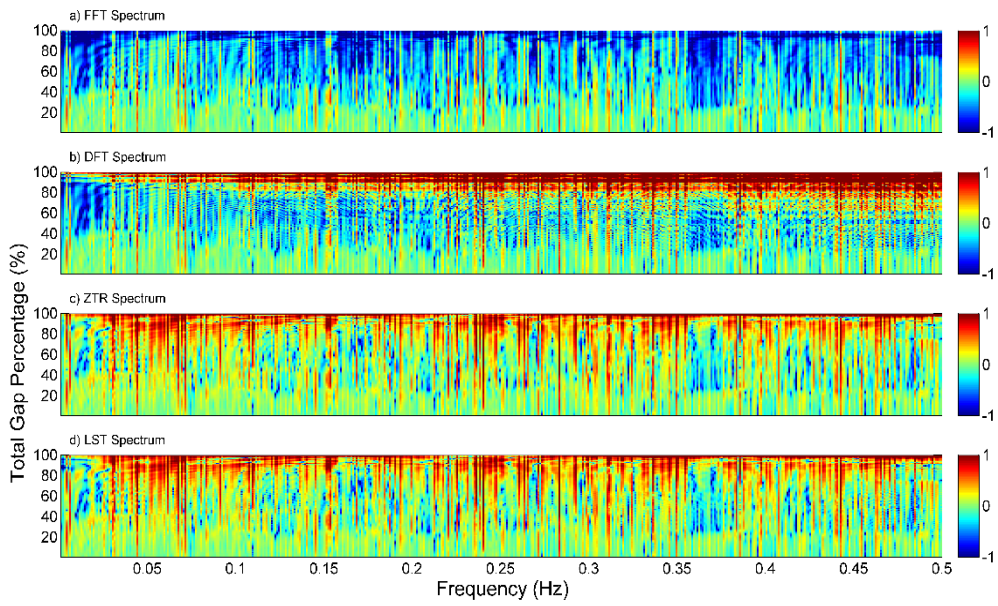


8

9 **Figure 13.** Case study for the Single Large Gap test applied on VEX data. The format is similar  
 10 to Fig. 2. In addition, panels b) - e) also show the original spectrum (black) and the average  
 11 level of the spectra for each method (thick lines).

12

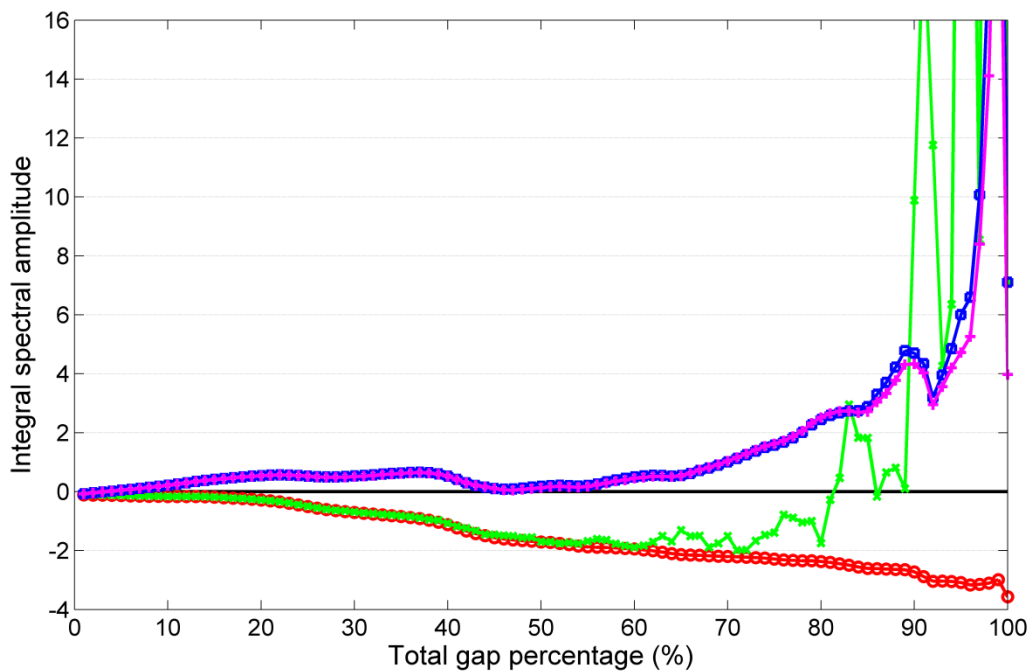
1



2

3 **Figure 14.** Results of the Single Large Gap test applied on VEX data. Represented are the  
4 difference of amplitude spectra (method – original) as a function of TGP and frequency: a)  
5 FFT, b) DFT, c) ZTR and d) LST.

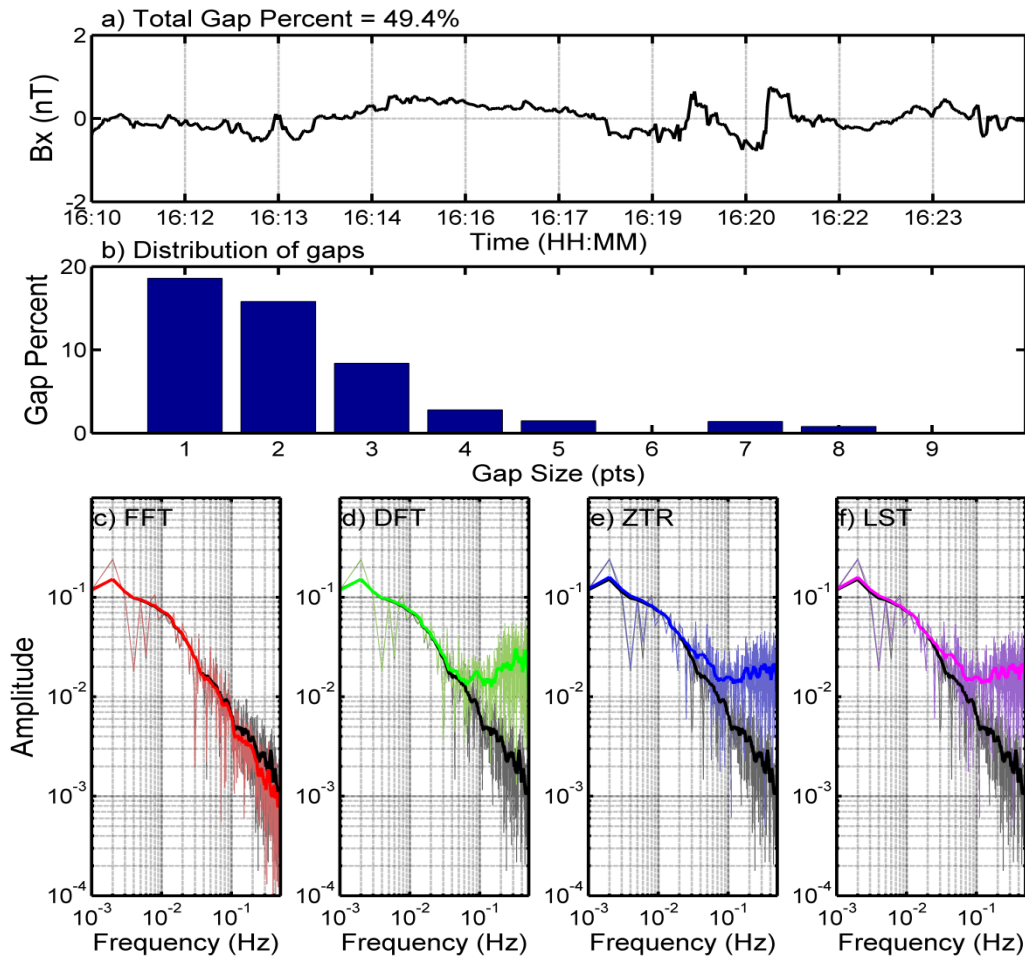
6



7

8 **Figure 15.** Integral spectral amplitude for the Single Large Gap test applied on VEX data.  
9 Shown are the results for: FFT (red), DFT (green), ZTR (blue) and LST (magenta).

1



2

3 **Figure 16.** Case study for the Multiple Small Gaps test applied on VEX data. The format is  
4 similar to Fig. 7. Panels c, d, e and f show the original average FFT spectrum (black) and the  
5 average spectra for each method.

6

7

8

9

10

11

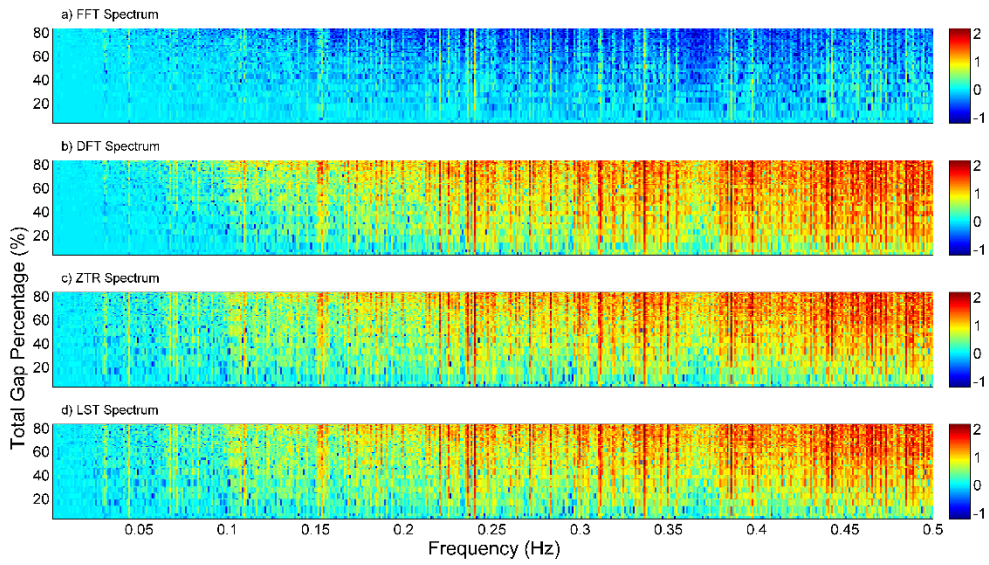
12

13

14

15

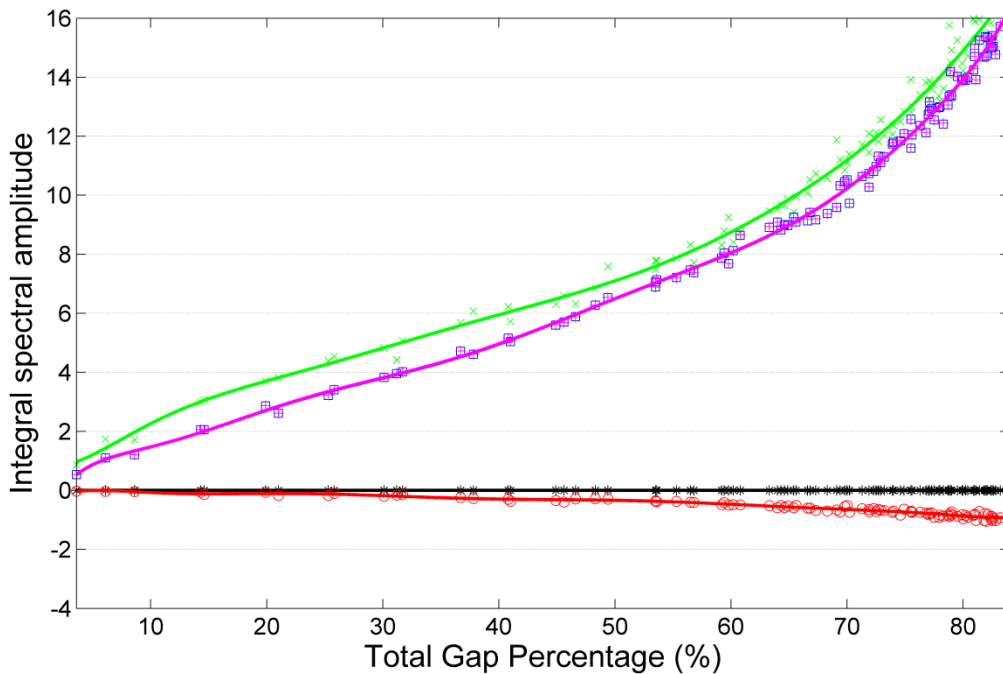
1



2

3 **Figure 17.** Results of the Multiple Small Gaps test applied on VEX data. The format is similar  
4 to Fig. 14.

5



6

7 **Figure 18.** Integral spectral amplitude for the Multiple Small Gaps test applied on VEX data.  
8 The format is similar to Fig. 15.

9



